THE SPECTRAL CHARACTERISTICS AND THE PROPAGATION IN THE MAGNETOSPHERE OF HYDROMAGNETIC EMISSIONS (PEARLS)

by

William R. Sill

B.S., Michigan State University
(1960)
S.M., Massachusetts Institute of Technology
(1963)

SUBMITTED IN PARTIAL FULFILLMENT
OF THE REQUIREMENTS FOR THE
DEGREE OF DOCTOR OF
PHILOSOPHY

at the

MASSACHUSETTS INSTITUTE OF TECHNOLOGY

September, 1967

Signature of Author.....
Dept. of Geology and Geophysics
September, 1967

Certified by.....
Thesis Supervisor

Accepted by.....
Chairman, Departmental Committee
on Graduate Students

3ND PPSO 13152

DOCUMENT CONTROL DATA - R&D

(Security classification of title, body of abstract and indexing annotation must be entered when the overall report is classified)

1 ORIGINATING ACTIVITY (Corporate author)	2a REPORT SECURITY CLASSIFICATION
MASSACHUSETTS INSTITUTE OF TECHNOLOGY CAMBRIDGE, MASSACHUSETTS	Unclassified
	2b GROUP

3. REPORT TITLE

THE SPECTRAL CHARACTERISTICS AND THE PROPAGATION IN THE MAGNETOSPHERE OF HYDROMAGNETIC EMISSIONS (PEARLS)

4. DESCRIPTIVE NOTES *(Type of report and inclusive dates)*

5. AUTHOR(S) *(Last name, first name, initial)*

Sill, William R.

6. REPORT DATE	7a. TOTAL NO. OF PAGES	7b. NO. OF REFS
December, 1967	187	37

8a. CONTRACT OR GRANT NO.	9a. ORIGINATOR'S REPORT NUMBER(S)
NR-371-401 b. PROJECT NO.	
c.	9b. OTHER REPORT NO(S) *(Any other numbers that may be assigned this report)*
d.	

10. AVAILABILITY/LIMITATION NOTICES

11. SUPPLEMENTARY NOTES	12. SPONSORING MILITARY ACTIVITY
	Office of Naval Research

13. ABSTRACT

Many of the observed characteristics of hydromagnetic emissions or pearls have been successfully explained by the propagation of the guided Alfven wave along geomagnetic lines of force. This thesis extends some of the previous work, which has concentrated on the dispersion properties of these signals, by examining the fine structure in the spectral character of these signals. These emissions all show a very dramatic spectral feature of a series of high Q peaks. This frequency structure is present in the individual dispersed wave trains, and should not be confused with the fine structure obtained in a Fourier analysis of a series of repetitive signals. It is shown that the spectral peaks that are observed are consistent with the high order field line resonances that would be expected from models which satisfy the observed dispersion. The mode numbers are so high, being of the order 20 to 50, that one cannot expect to predict the actual frequencies observed. The observed separations between the peaks are in good agreement with those predicted from the model studies. An interpretation is proposed that the emissions are produced by the cyclotron resonance amplification of a background wave spectrum of resonant field line oscillations.

(continued)

DD FORM 1 JAN 64 1473 IIA 0101 807 6800

14. KEY WORDS	LINK A		LINK B		LINK C	
	ROLE	WT	ROLE	WT	ROLE	WT
Hydromagnetic emissions						
Particle-wave interactions						
Guided Alfven wave resonances						
Magnetosphere Plasma densities						

INSTRUCTIONS

1. ORIGINATING ACTIVITY: Enter the name and address of the contractor, subcontractor, grantee, Department of Defense activity or other organization *(corporate author)* issuing the report.

2*a*. REPORT SECURITY CLASSIFICATION: Enter the overall security classification of the report. Indicate whether "Restricted Data" is included. Marking is to be in accordance with appropriate security regulations.

2*b*. GROUP: Automatic downgrading is specified in DoD Directive 5200.10 and Armed Forces Industrial Manual. Enter the group number. Also, when applicable, show that optional markings have been used for Group 3 and Group 4 as authorized.

3. REPORT TITLE: Enter the complete report title in all capital letters. Titles in all cases should be unclassified. If a meaningful title cannot be selected without classification, show title classification in all capitals in parenthesis immediately following the title.

4. DESCRIPTIVE NOTES: If appropriate, enter the type of report, e.g., interim, progress, summary, annual, or final. Give the inclusive dates when a specific reporting period is covered.

5. AUTHOR(S): Enter the name(s) of author(s) as shown on or in the report. Enter last name, first name, middle initial. If military, show rank and branch of service. The name of the principal author is an absolute minimum requirement.

6. REPORT DATE: Enter the date of the report as day, month, year; or month, year. If more than one date appears on the report, use date of publication.

7*a*. TOTAL NUMBER OF PAGES: The total page count should follow normal pagination procedures, i.e., enter the number of pages containing information.

7*b*. NUMBER OF REFERENCES: Enter the total number of references cited in the report.

8*a*. CONTRACT OR GRANT NUMBER: If appropriate, enter the applicable number of the contract or grant under which the report was written.

8*b*, 8*c*, & 8*d*. PROJECT NUMBER: Enter the appropriate military department identification, such as project number, subproject number, system numbers, task number, etc.

9*a*. ORIGINATOR'S REPORT NUMBER(S): Enter the official report number by which the document will be identified and controlled by the originating activity. This number must be unique to this report.

9*b*. OTHER REPORT NUMBER(S): If the report has been assigned any other report numbers *(either by the originator or by the sponsor)*, also enter this number(s).

10. AVAILABILITY/LIMITATION NOTICES: Enter any limitations on further dissemination of the report, other than those imposed by security classification, using standard statements such as:

(1) "Qualified requesters may obtain copies of this report from DDC."

(2) "Foreign announcement and dissemination of this report by DDC is not authorized."

(3) "U. S. Government agencies may obtain copies of this report directly from DDC. Other qualified DDC users shall request through _____."

(4) "U. S. military agencies may obtain copies of this report directly from DDC. Other qualified users shall request through _____."

(5) "All distribution of this report is controlled. Qualified DDC users shall request through _____."

If the report has been furnished to the Office of Technical Services, Department of Commerce, for sale to the public, indicate this fact and enter the price, if known.

11. SUPPLEMENTARY NOTES: Use for additional explanatory notes.

12. SPONSORING MILITARY ACTIVITY: Enter the name of the departmental project office or laboratory sponsoring *(paying for)* the research and development. Include address.

13. ABSTRACT: Enter an abstract giving a brief and factual summary of the document indicative of the report, even though it may also appear elsewhere in the body of the technical report. If additional space is required, a continuation sheet shall be attached.

It is highly desirable that the abstract of classified reports be unclassified. Each paragraph of the abstract shall end with an indication of the military security classification of the information in the paragraph, represented as *(TS), (S), (C), or (U)*.

There is no limitation on the length of the abstract. However, the suggested length is from 150 to 225 words.

14. KEY WORDS: Key words are technically meaningful terms or short phrases that characterize a report and may be used as index entries for cataloging the report. Key words must be selected so that no security classification is required. Identifiers, such as equipment model designation, trade name, military project code name, geographic location, may be used as key words but will be followed by an indication of technical context. The assignment of links, roles, and weights is optional.

THE SPECTRAL CHARACTERISTICS AND THE PROPAGATION IN THE MAGNETOSPHERE OF HYDROMAGNETIC EMISSIONS (PEARLS)

by

William R. Sill

Submitted to the Department of Geology and Geophysics on

September 15, 1967

in partial fulfillment of the requirements for the degree of

Doctor of Philosophy

Abstract

Many of the observed characteristics of hydromagnetic emissions or pearls have been successfully explained by the propagation of the guided Alfven wave along geomagnetic lines of force. This thesis extends some of the previous work, which has concentrated on the dispersion properties of these signals, by examining the fine structure in the spectral character of these signals. These emissions all show a very dramatic spectral feature of a series of high Q peaks. This frequency structure is present in the individual dispersed wave trains, and should not be confused with the fine structure obtained in a Fourier analysis of a series of repetitive signals. It is shown that the spectral peaks that are observed are consistent with the high order field line resonances that would be expected from models which satisfy the observed dispersion. The mode numbers are so high, being of the order of 20 to 50, that one cannot expect to

predict the actual frequencies observed. The observed separations between the peaks are in good agreement with those predicted from the model studies. An interpretation is proposed that the emissions are produced by the cyclotron resonance amplification of a background wave spectrum of resonant field line oscillations.

The interpretation of the emissions that were observed from a station in New Hampshire results in relatively low equatorial particle density estimates. This indicates that the waves are amplified and propagate in the rarefied plasma beyond the plasmapause. The previously reported correlation between pearl activity and modestly disturbed geomagnetic activity is also observed. Some examples are shown where pearl activity is also closely correlated with decreases in the energy of the neighboring frequency band, PC2,3. No fast rule could be set on this behavior however.

Improvements were made in the analysis of the travel time and dispersion data by incorporating the effects of the dipole field distortions produced by the magnetosphere solar wind interaction.

Thesis supervisor: Theodore R. Madden

Title: Professor of Geophysics

ACKNOWLEDGEMENTS

I am most indebted to Professor T. R. Madden for his guidance and encouragement throughout the course of this thesis work. I would also like to thank Professor A. Gangi, Dr. R. Greenfield and Professor J. Claerbout for many helpful discussions and Dr. K. Vozoff who supplied some of the data.

Thanks must also go to my wife, Mary, for her patience and understanding.

The American Chemical Society provided support for the author during his graduate years and the research was funded by the Office of Naval Research (Project Nr-371-401). Support during the authors stay in California (University of California, San Diego) was provided by a research grant from the Chevron Research Corp.

Funds for the analogue to digital converter were supplied by the Socony-Mobil Company.

The computations were performed at the MIT Computation Center on the IBM 7094.

My thanks also to Miss J. Mulligan who typed the manuscript.

TABLE OF CONTENTS

Table of Contents Continued -

LIST OF FIGURES

FIGURE

FIGURE

LIST OF TABLES

TABLE

Chapter 1

INTRODUCTION AND THE DISPERSION CHARACTERISTICS OF THE ANISOTROPIC ALFVEN WAVE

1.1 Introduction

The plasma that exists in the magnetosphere is of intense interest to scientists in a number of fields since nature has provided a medium with parameters (density, temperature, etc.) that are difficult, if not impossible, to duplicate in the laboratory. In a way we might consider this vast space as a laboratory in which nature carries out experiments for us (the natural phenomena) and in which we can conduct experiments of our own design.

Hydromagnetic emissions is one such natural phenomenon which in recent years has attracted considerable attention. These natural oscillations of the earth's magnetic field have also been referred to as pearls and hydromagnetic whistlers. As the last of these names implies, hydromagnetic emissions are in some ways similar to ordinary audio whistlers in that they are dispersive plasma waves that propagate along field lines in the magnetosphere. However the frequencies of pearls (.1-5cps) are lower by three or four orders of magnitude than those of whistlers. As with whistlers, the dispersion characteristics of pearls can be used to determine the density of charged particles in the magnetosphere. Pearls commonly propagate to distances in the magnetosphere that are greater than those reached by whistlers and therefore are important in providing data on the density which would not otherwise be available.

The first observations of pearls were made by Sucksdorf (1936) and Harung (1936). The time-amplitude recordings of these micropulsations appear as bursts of sinusoidal oscillations and Sucksdorf described a series of these bursts as

resembling "a pearl necklace of oval pearls of different sizes". (figure 1.1.1,b). During the next twenty years nothing more appears in the literature concerning pearls, probably because the attention of most workers in geomagnetism was centered on the lower frequency oscillations such as the giant micropulsations and the magnetic storm variations.

Interest in the higher frequency micropulsations was revived during the IGY (1957-1958) and observations of pearls were reported by Troitskaya (1957,1961) and Benioff (1960).

A significant improvement in the analysis of micropulsation data was achieved by the use of audio spectrum analyzers (Duffus, 1958; Tepley 1961). The low frequency oscillations are recorded on magnetic tape which is later played back at a high speed so that the frequencies are shifted up into the audio band. The typical output of these audio analyzers is a sonogram (dynamic spectrum) which indicates the frequency content of a signal as a function of time.

On this type of display (frequency vs. time) a hydromagnetic emission appears as a repetitive series of rising and overlapping wave trains. (figure 1.1.1,a) Before the use of sonogram techniques the repetitive nature of hydromagnetic emissions was not readily apparent. This is due to the fact that on an amplitude vs. time recording the overlapping wave trains interfere, resulting in an irregular modulation or beating appearance. It is only when the frequency band is so narrow that the wave trains do not overlap that the repetitive nature of these signals is obvious on the amplitude vs. time display.

The first suggestion of the source of hydromagnetic emissions appeared in a paper by Tepley in 1961. In particular, he noted that the ratio of the frequencies of VLF to

FIGURE 1.1.1

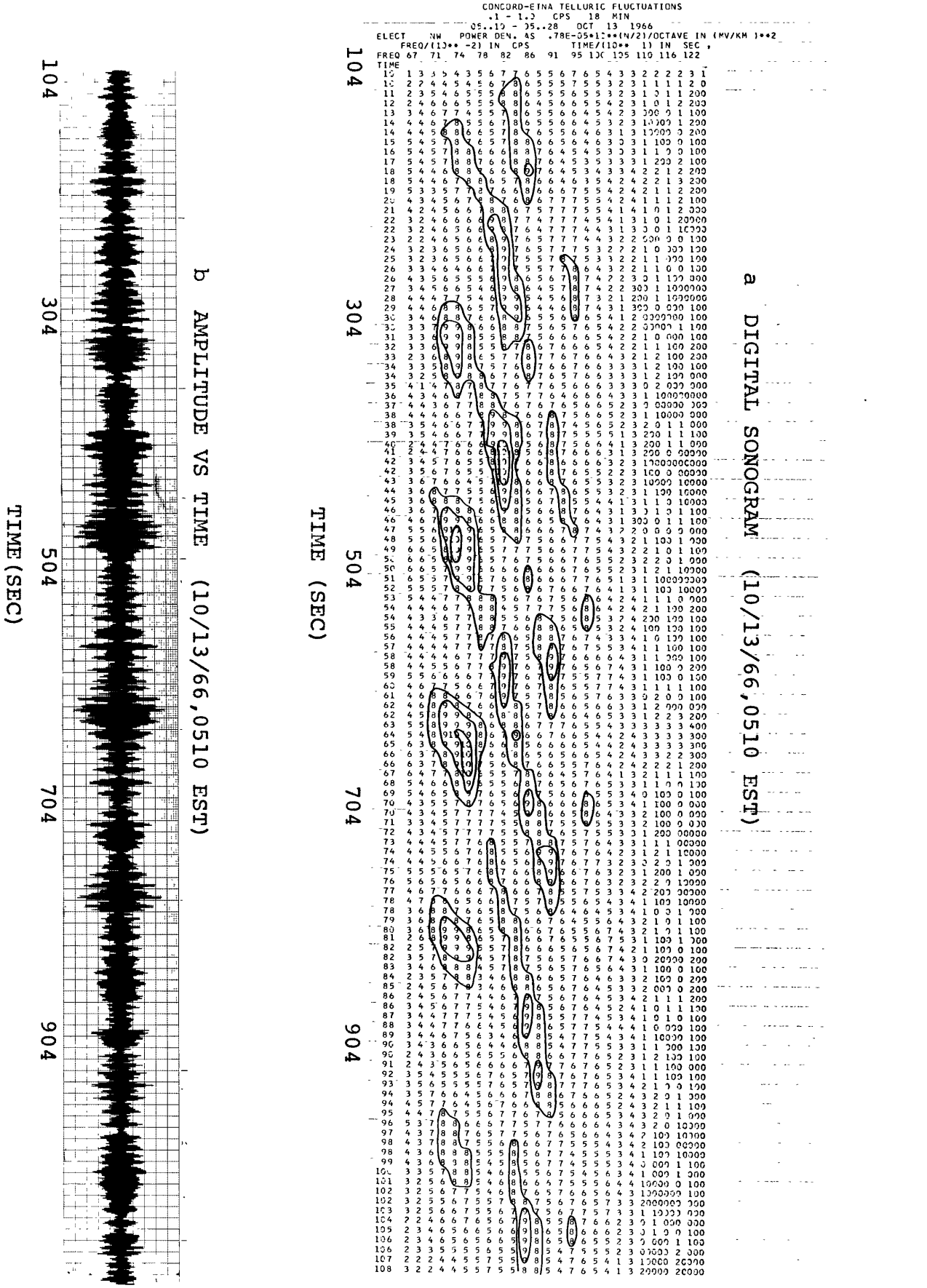
CONCORD-ETNA TELLURIC FLUCTUATIONS
.1 - 1.0 CPS 18 MIN
05..10 - 05..28 OCT 13 1966
ELECT NW POWER DEN. AS .78E-05*10**(N/2)/OCTAVE IN (MV/KM)**2
FREQ/(10** -2) IN CPS TIME/(10** 1) IN SEC ,
FREQ 67 71 74 78 82 86 91 95 100 105 110 116 122
TIME
104
304
504
704
904
TIME (SEC)
a DIGITAL SONOGRAM (10/13/66, 0510 EST)
b AMPLITUDE VS TIME (10/13/66, 0510 EST)

hydromagnetic emissions was of the same order as the ratio of the proton mass to the electron mass. Since Gallet (1959) had proposed that VLF emissions were the result of a traveling wave amplification by electrons, it was natural to suppose that a similar mechanism with protons as the charged particles might be operative in the case of hydromagnetic emissions. Though this view was later shown to be substantially correct it was dropped in favor of one proposing that hydromagnetic emissions were the result of perturbations of the magnetic field caused by the mirroring of fast particle bunches. (Tepley and Wentworth, 1962; Wentworth and Tepley, 1962; Gendrin, 1963). According to Gendrin (1963) a proton bunch mirroring at the pearl period (approximately 1 sec.) caused a pearl bead as it drifted over a station; the next pearl bead would be formed when the bunch had drifted around the earth and was once more over the station. The repetition period was then due to the westward drift period of the proton bunch. As a result of this theory, one would expect the the pearl beads to be observed simultaneously at conjugate points since these fast particles mirror in less than a few seconds. However, conjugate studies by Yanagihara (1963), Loken, Shand and Wright (1963) and Tepley (1964) have shown that the signal groups are received alternately in opposite hemispheres.

If the agent causing hydromagnetic emissions travels along field lines, the time delay between signals received at conjugate points indicates a velocity of the order of 10^3 km/sec. Yanigihara (1963) proposed two possible agents, either slow particle bunches or hydromagnetic (Alfven) waves. The present theories consider the waves and particles as a coupled system, which under certain conditions can become unstable with respect to the growth of the waves. These

theories are concerned with the cyclotron resonance instability in which protons passing through the wave field see a Doppler shifted frequency equal to their gyrofrequency. Under this condition the protons experience a resonance with the electric field of the wave and are scattered in velocity space. Since the total energy in the wave-particle system is constant, the waves will grow if the particles are scattered so as to loose energy. Papers investigating the source of hydromagnetic emissions as a cyclotron resonance interaction between waves and particles have been published by Jocobs and Watanabe (1965), Cornwall (1965), Tepley, wentworth and Admunsen (1964), Huruska (1966) and Liemohn (1967).

Once the waves have been generated or amplified in the source region near the equatorial plane, they propagate along the field lines to the surface where part of the energy is reflected and returned to the source region. Calculations of the dispersion, travel times and guiding of the anisotropic Alfven wave (Jacobs and Watanabe, 1964; Obayashi, 1965; Pope, 1965; and Sill, 1965) indicated that these waves could explain many of the observed characteristics of hydromagnetic emissions. On the assumption that the earth's field could be represented by a dipole field, Watanabe (1965) and Wentworth (1966) developed techniques which would allow one to determine the density in the magnetosphere from the observed dispersion.

Hydromagnetic emissions are observed at the surface of the earth from the auroral regions to the equator. Since the dispersion of these waves indicates that they have propagated on high latitude field lines (L=4 to 10), there must be some mechanism permitting the energy to propagate to low latitudes. The suggestion has been made (Tepley and Landshaff, 1966;

Manchester, 1966) that the energy may propagate in a leaky wave guide in the ionosphere. The wave guide is the result of a minimum in the phase velocity at an altitude of 400 km. The velocity in this region is of the order of 10^3 km/sec which could explain the 2 to 3 second shifts in arrival times observed between stations separated by a few thousand km.

Digital sonograms have shown that the energy in a wave-train is not evenly distributed in frequency but that there is a series of approximately equally spaced peaks in the spectra. This gives the rising tones a certain bead-like appearance (figure 1.1.1a). These peaks are a very pronounced feature of hydromagnetic emissions, often being 10 to 20 db above the background and having Q's of the order of 10 to 50. This important feature often is not apparent on the output of the usual analogue spectrum analyzer because of the limited dynamic range of the heat sensitive paper used.

One purpose of this thesis is to show that this frequency structure is a result of the source mechanism (the plasma instability) amplifying the background waves which have a spectrum determined by the resonant modes of oscillation of the field lines. We have in this case a system (the magnetic field and the plasma) which is capable of sustaining resonant oscillations. The background waves due to random excitations have a spectrum characteristic of this resonant mode structure, so that those waves with frequencies of the resonant modes can be expected to have the largest amplitudes. When the conditions are favorable, the plasma instability is capable of amplifying these waves to levels where they are observable at the surface.

Since the dispersion characterisitcs of these waves provide useful information on the density distribution in the magnetosphere another purpose of this thesis is to investigate the effects of various magnetospheric field line and density

models on the wave propagation. This will be done by comparing the results derived for propagation along field lines in a pure dipole field, the only case treated heretofore in the literature, with propagation along field lines in a distorted dipole field such as that which exists in the magnetosphere. The effects on the dispersion as a result of the waves not being perfectly guided by the field will also be discussed.

Outline of Thesis

In the remainder of Chapter 1 we will discuss the propagation of the anisotropic Alfven wave in the magnetosphere; investigating the results of several models for the density distribution and the field line configuration.

Chapter 2 will cover the data collection and analysis; including a brief description of the digital sonogram program. The results of the observations in terms of the spectra, sonograms and the calculated proton densities will also be shown.

Chapter 3 begins with a general discussion of the vibration of non-uniform strings. A one dimensional layered model for the determination of the resonant modes is presented and the results of the calculations are discussed and compared with the observations.

Chapter 4 presents a brief summary and discussion of the results and makes some suggestions for further work.

1.2 Group Travel Times

The anisotropic or slow Alfven wave is guided by the magnetic field and in Appendix A it is shown that the group velocity vector is confined to within 10^{o} of the field line direction for all angles of phase propagation from 0^{o} to 90^{o}. For phase propagation parallel to the magnetic field this wave has left-circular polarization and the group velocity is (equation A.5)

$$U_g = V_A (1-F_+)^{3/2}/(1-.5F_+) \qquad 1.2.1$$

where $$V_A = B/[4\pi n m_+]^{1/2}$$

$F_+ = \omega/\Omega_+ =$ ratio of angular frequency to the ion gyrofrequency

In this section we will consider only propagation parallel to the field since for angles up to 30^{o} the magnitude of the group velocity is not a strong function of the direction. The group travel time as a function of frequency is found by evaluating the following integral

$$T(F) = \int_S \frac{ds}{U_g(f)} \qquad 1.2.2$$

The path of integration S is to be taken along the ray trajectory, however in the following sections the ray path will be assumed to be along the field lines of either a dipole or a distorted dipole.

The results of Appendix B show that for frequencies of the order of the ion gyrofrequency the ray paths deviate from the dipole field lines. The consequences of the assumption that the ray path is along the field line will be discussed in Section 1.5.

Under the assumption that the ray trajectory is along the field line, the path of integration (S) can be readily determined. The magnitude of the field (B) which is needed to calculate the classical Alfven velocity (Va) and the gyrofrequency (Ω_+) must also be calculated. We are left then with the problem of determining the density (n) along the field lines before the integral in equation 1.2.1 can be evaluated.

1.3 Density Models

Whistler data (Carpenter, 1966; Angerami and Carpenter, 1966) indicates that the density of electrons in the equatorial plane falls off something like the inverse third or fourth power of the radius. Carpenter (1966) has shown that during periods of little geomagnetic activity ($0 < K_p < 1$) the density profile shows a relatively flat slope near 3 earth radii (3 Re) which gradually steepens beyond this distance so that the density falls off as r^{-3} near 3.5 Re; beyond 4 Re and density decreases as r^{-4}.

When the magnetic activity is moderate ($2 < K_p < 4$) a discontinuity or knee exists in the equatorial density profiles at a mean distance of 4 Re. At the knee an abrupt drop in the density by a factor of .03 to .01 is present; however, the density on either side of the knee falls off as r^{-4}. Satellite data on the proton density (Taylor, Brinton and Smith, 1965) and the work of Carpenter (1966) indicate that the discontinuity is a field aligned feature. When the knee exists we have two regions in the magnetosphere. The first is a relatively dense doughnut shaped region interior to the field line which crosses the equator at 4 Re (L = 4) and the second is a low density region between the L=4 field line and the magnetopause. The L parameter will be used throughout this work to indicate the field line by its equatorial crossing point in units of earth radii.

Since hydromagnetic emissions are guided by the field lines, we can expect that if a wave originates on a line exterior to the knee it will continue to propagate in the low density region outside the knee. Observations of hydromagnetic emissions in New Hampshire have shown that these waves have propagated on field lines with L parameters

greater than 4 and hence beyond the mean position of the knee. Furthermore the densities calculated are quite low indicating that the knee exists somewhere on an L shell less than that on which the waves were propagating.

With these facts in mind we will propose two models for the density of the ions in which the density is inversely proportional to the third and fourth power of the radius. Other models have been used where the density was made proportional to some power of the magnetic field (Watanabe, 1965). A model of this type allows the density to be a function of the latitude as well as the radial distance. Calculations made including a latitude dependence differ by a few percent from those with a radial dependence only. The models to be used here will allow only a dependence on radial distance. The density model is given in 1.3.1.

$$n = n_0 (R_e / r)^P \qquad 1.3.1$$

where

P = 3 or 4

n_0 = ion density extrapolated to surface

$n_e = n_0 / L^P$ = ion density in the equatorial plane at r =LRe

R_e = radius of the earth

λ = magnetic latitude (figure 1.4.1)

This type of model will represent the density along a field line in the outer portion of the magnetosphere (r > 1.5 Re) quite well but it will be badly in error in the ionosphere. The calculations of the travel times will not be seriously affected however, since the propagation time from an altitude of 3,000 km to the surface (1 sec) will be only a small

fraction of the travel time from the equator to this altitude (16-32 sec). The most critical region for the travel time calculation is the outer portion of the field line in the equatorial region where the velocities are low over large distances and where the waves are most dispersive due to the low gyrofrequency. It is this region where we expect our model to be most accurate.

The density extrapolated to the surface (n_o) does not correspond to any real density but is convenient for specifying a model. Hereafter, when discussing physically meaningful densities we will refer to the equatorial density (n_e).

It will be assumed in this chapter that the positive ions are hydrogen. Satellite measurements have shown that the ratio of hydrogen to helium ions at large distances is usually of the order of 100 to 1. (Taylor, Brinton and Smith, 1965). In order to take into account the presence of other positive ions one must consider propagation in a multicomponent plasma (Smith and Brice, 1964). One of the main results of this type of treatment is the introduction of a new set of resonances (v_p=o) at each of the ion gyrofrequencies. For Helium this would introduce a resonance at a frequency one-fourth of the proton gyrofrequency.

1.4 Propagation in a Dipole Field

As a first approximation, the field in the magnetosphere can be considered as that of a dipole. This approximation is good for field lines which cross the equator at distances less than 4 Re (L=4) when the distance to the magnetopause in the noon meridian is 10 Re. At distances greater than 4 Re, the field lines are compressed and distorted. For the above-mentioned case, the dipole field line with L=7 has its equatorial crossing point moved to 6 Re in the noon meridian and to 6.5 Re in the midnight meridian.

Assuming for the present propagation along dipole field lines we have the geometry in figure 1.4.1

Figure 1.4.1

Geometry of Wave Propagation in a Dipole Field

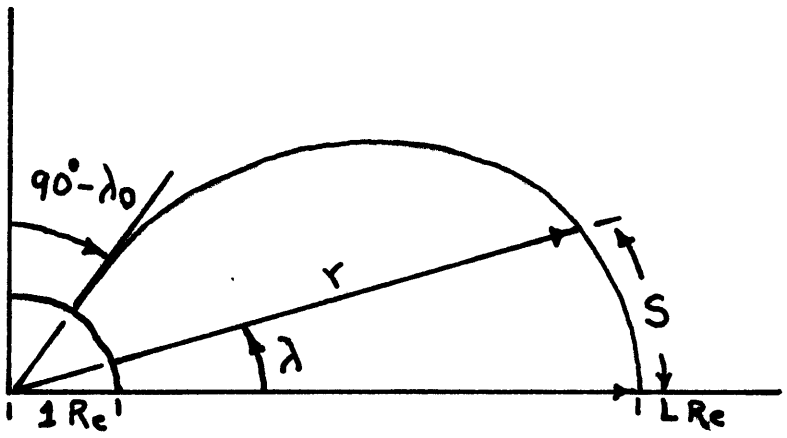

For a dipole field we have

$$r = R_e L \cos^2\lambda \qquad \text{equation of field line}$$

Re = radius of Earth

LRe = distance to field line at equator

λ_o = latitude of field line at surface

$L = 1/\cos^2\lambda_o$ 1.4.1

S = arc distance along field line

$$dS = LRe\left[\cos\lambda\right]\left[4-3\cos^2\lambda\right]^{1/2} d\lambda$$

The two hop travel time in terms of the latitude of a point on the field is from equation 1.2.2

$$T = 4LR_e \int_0^{\lambda_o} \frac{d\lambda}{U_g} (\cos\lambda)\left[4-3\cos^2\lambda\right]^{1/2} \qquad 1.4.2$$

The group velocity (U_g) along the path S depends on the magnetic field strength, the local ion gyrofrequency and the density of positive ions (equation 1.2.1). The first and the second of these quantities are easily determined for a dipole field and for the last we will utilize the two models proposed in the previous section.

Along a field line the magnitude of the field varies as

$$B = \frac{B_o}{L^3} \frac{[4 - 3\cos^2\lambda]^{1/2}}{\cos^6\lambda} \qquad 1.4.3$$

where

Bo = .314 Gauss.

The gyrofrequency of the ions is proportional to B and the dependance of the ratio of the wave frequency to the gyrofrequency is given by 1.4.4.

$$F_+ = \omega/\Omega_+ = F\cos^6\lambda / [4 - 3\cos^2\lambda]^{1/2} \qquad 1.4.4$$

where

$F = \omega / \Omega_+^e$; Ω_+^e = equatorial gyrofrequency

Combining equations 1.2.1, 1.3.1, 1.4.3, and 1.4.4 the expression for the group velocity along a field line becomes

$$u_g = V_o L^{P/2-3} (\cos^{P-6}\lambda) \frac{[4 - 3\cos^2\lambda]^{1/2}[1 - aF]^{3/2}}{[1 - .5aF]} \qquad 1.4.5$$

where $a(\lambda) = \cos^6\lambda / [4 - 3\cos^2\lambda]^{1/2}$

$V_o = B_o / [4\pi n_o m_+]^{1/2}$

Substituting 1.4.5 in 1.4.2 we have for the two density models P=3 and P=4.

$$T_3(F) = \frac{4R_e L^{5/2}}{V_o} \int_0^{\lambda_o} d\lambda \frac{[\cos^4\lambda][1 - .5a(\lambda)F]}{[1 - a(\lambda)F]^{3/2}} \qquad 1.4.6$$

$$T_4(F) = \frac{4R_e L^2}{V_o} \int_0^{\lambda_o} d\lambda \frac{[\cos^3\lambda][1 - .5a(\lambda)F]}{[1 - a(\lambda)F]^{3/2}} \qquad 1.4.7$$

Equations 1.4.6 and 1.4.7 were numerically integrated and the results for the P=4, no=3.8 10^3 model are shown in figure 1.4.2. In this figure are plotted the round trip travel times as a function of frequency and L parameter. The horizontal asymptotes for each of these dispersion curves is the equatorial ion gyrofrequency (Ω_+^e). From this figure it is seen that the form of the curves as a function of L (or equivalently Ω_+^e) are essentially the same. Changing the value of n_o results in the shifting at the curves parallel to the horizontal axis while the variation of L translates the curves both vertically and horizontally.

The insensitivity of the form of the curves to the L parameter suggests that a normalization of the travel time and the frequency will result in a simpler representation. One such normalization, the dimensionless frequency ($F=\omega/\Omega_+^e$) has already been utilized; the second will make use of the dimensionless time $T(F)/T_o$, which is the ratio of the travel time at the frequency F to the travel time of a low frequency wave which is nondispersive ($F \rightarrow 0$). The normalized curves in terms of these demensionless parameters are shown in figure 1.4.3.

We see from these normalized dispersion curves that the travel times are quite insensitive to the density model used. In the process of normalizing these curves we have removed the dependence of the travel time on the density parameter. To complete our knowledge of the dispersion we must determine the dependence of T_o on the density parameter n_o (or n_e) and of the equatorial gyro-

FIGURE 1.4.2
GROUP TRAVEL TIMES , DIPOLE FIELD

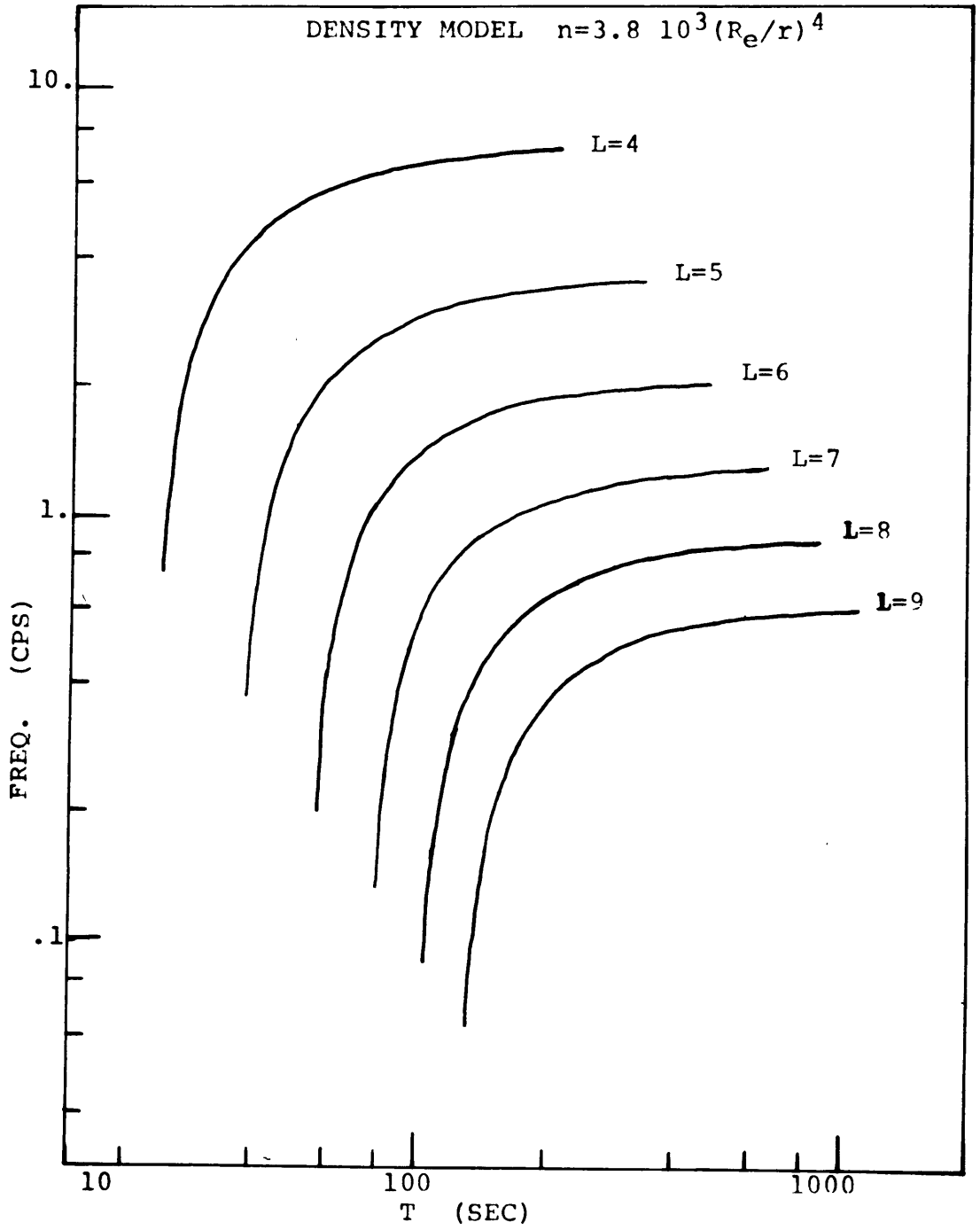

FIGURE 1.4.3
NORMALIZED DISPERSION CURVES
DIPOLE FIELD

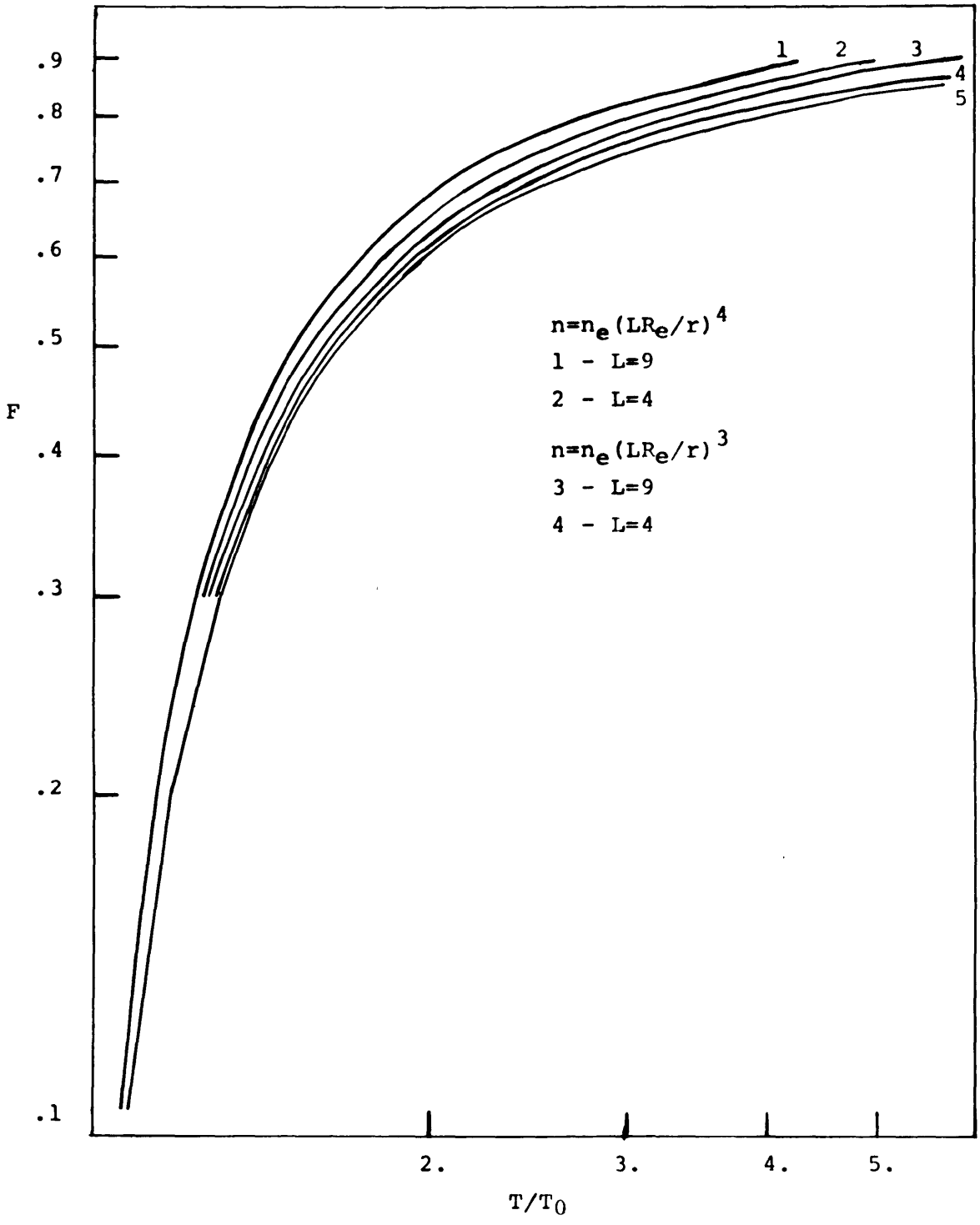

frequency on L. This information is obtained from equations 1.4.6, 1.4.7 and 1.4.4 and is shown in figure 1.4.4. The use of these curves to determine the L shell on which the waves have propagated and the equatorial density will be illustrated by the following example.

On April 13, 1966, a hydromagnetic emission occurred, part of which exhibited a series of rising wave trains that were successively dispersed. The average repetition period as measured over ten wave trains was 174 sec at .416 cps and 208 sec at .616 cps. In order to fit this dispersion to our normalized curves, we form the ratios $f_L/f_H = .675$ and $T_H/T_L = 1.2$. These numbers are then plotted on the vertical (F) and horizontal $(T(F)/T_o)$ axies of figure 1.4.3 and joined by a straight line. We then translate this short line segment until its end points fall on one of the curves. The ordinates and abscissas of the end points give the ratios $f_L/f_{\mp}^e$, T_L/T_o, $f_H/f_{\mp}^e$ and T_H/T_o. From either set of these we can determine the equatorial gyrofrequency $(f_{\mp}^e)$ and T_o. These two parameters and figure 1.4.4 permits us to determine the equatorial density and L value.

Following this procedure for the above event we obtain the results in table 1.4.1

FIGURE 1.4.4
EQUATORIAL GYROFREQUENCY AND $T_0/\sqrt{n_e}$
AS A FUNCTION OF L

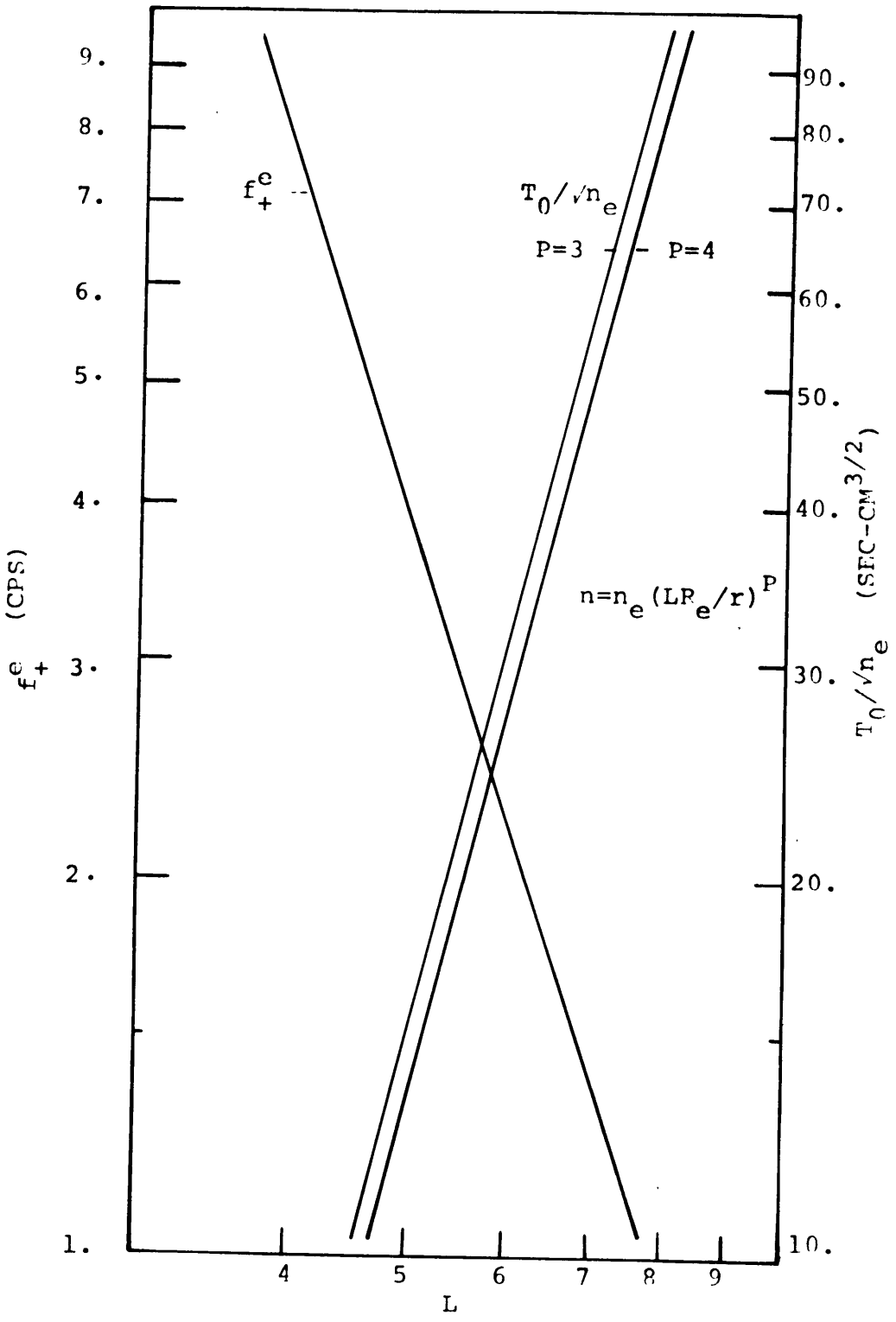

Table 1.4.1

Dipole interpretation of the emission of 4/13/66 0330/EST

Two density models

	P = 3	P = 4
f (cps)	1.21	1.18
L	7.3	7.4
T_o (sec)	132	134
n_e ($1/cm^3$)	4.6	3.6

The difference in L value from the two models is one percent and the density for the P=3 model is 27 percent greater than that for the P=4 model. The results for the P=4 model should be closer to the real situation since the density at large distances actually falls off as r-4 (section 1.3 and section 2.5).

Repeated tests fitting the same dispersion data to the curves indicates that an accuracy of about 5 to 10 percent in the estimate of n_e can be obtained. Larger errors can arise from the process of measuring the repetition period from the sonograms. Typically the width of the rising wave trains is 40 to 60 seconds and their total length, one to several minutes. The width of the traces allows a certain leeway in the sloping line that can be drawn through the rising wave train. Obviously this problem is more serious when the bandwidth of the event is narrow. The errors in measuring the repetition periods at two frequencies can be reduced by averaging the repetition periods over a number of wave trains; this is satisfactory as long as the repetition periods (and hence the density) are not changing with time.

A 3 percent increase in T_H of the previous example (4/13/66) would lead to a 6 percent decrease in the estimated equatorial density. The same increase when applied to an event having half the bandwidth of the event of 4/13/66 would give rise to a 13 percent decrease in the equatorial density.

The digital sonograms used by the author typically have a sampled output every 8 to 20 seconds for events with repetition periods of the order of 100 to 200 seconds. A 3 percent criteria in measuring the repetition period implies that over 5 wave trains the arrival of energy can be picked within 1 or 2 lines (15-30 sec.) of sampled output. Considering the width of the traces (2-6 samples) this is about the best accuracy that can be hoped for.

Since the slopes of the curves in figure 1.4.4 are steep it is helpful in practice to either expand the scale or to eliminate the dependence on L between f_H^e and T_o and to plot $T_o/\sqrt{n_e}$ as a function of f_H^e. Data for replotting the curves in this and the following sections will be found in Appendix C.

1.5 Dispersion Characteristics for Propagation Along Ray Paths in a Dipole Field.

In appendix B it is shown that for frequencies of the order of the ion gyrofrequency the ray paths deviate from dipole field lines. For zero initial angle (θ_o) the ray paths are exterior to the field lines and as F increases the deviation from the dipole line increases. Since the magnetic field strength is smaller along each of these ray paths the dispersion will increase as F increases. Equation 1.4.7 was numerically integrated along the ray paths and the results for are shown in figure 1.5.1. The L parameter as used in this section indicates the equatorial crossing point of the ray path. For comparison figure 1.5.1 also contains the normalized dispersion for propagation along a dipole field line. The normalized dispersion, as in the previous section, is not strongly dependent on the L value and the ratio $T_o / \sqrt{n_e}$ is the same as calculated in section 1.4 since at low frequencies the ray paths are along the field lines. Figure 1.5.2 illustrates the change in the dispersion as the initial angle (θ_o) is varied. When θ_o is positive the ray paths are outside of the field line and the dispersion increases as θ_o increases from 0 to 20 degrees. When θ_o exceeds 30 to 40 degrees the guiding becomes better (Appendix A) and the dispersion begins to decrease. For θ_o negative, part of the ray path can be inside the field line and part outside. (Appendix B). The net effect for $\theta_o = -10^o$ is for the dispersion along the ray path to exceed the dispersion along the field line. When $\theta_o = -20^o$ and F less than .6 the dispersion along the ray path and the field line are very nearly the same and when F is greater than .6 the

FIGURE 1.5.1

NORMALIZED DISPERSION - DIPOLE FIELD

ALONG FIELD LINE AND RAY PATH

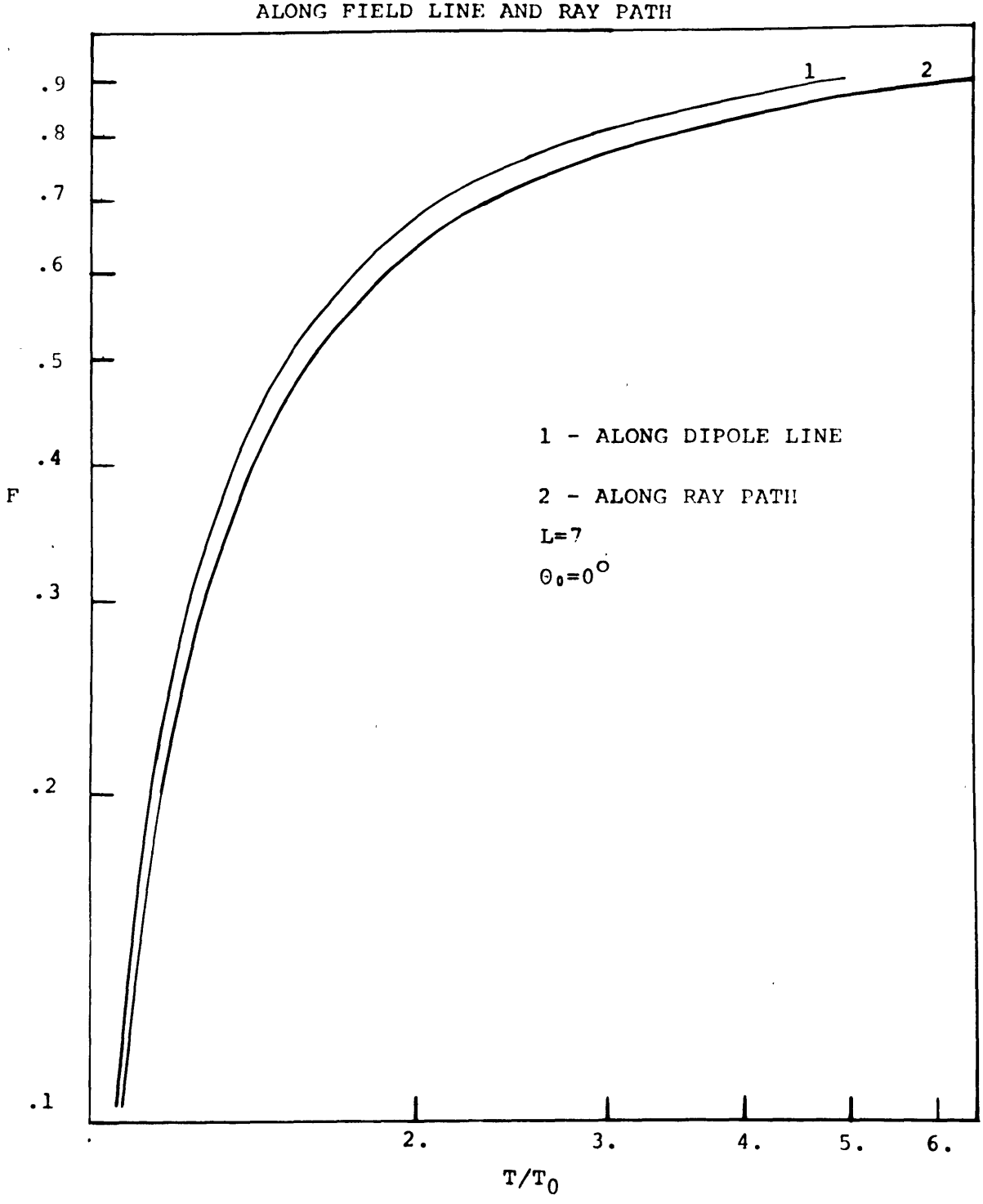

FIGURE 1.5.2
NORMALIZED DISPERSION
ALONG RAY PATHS AS A FUNCTION OF θ_0

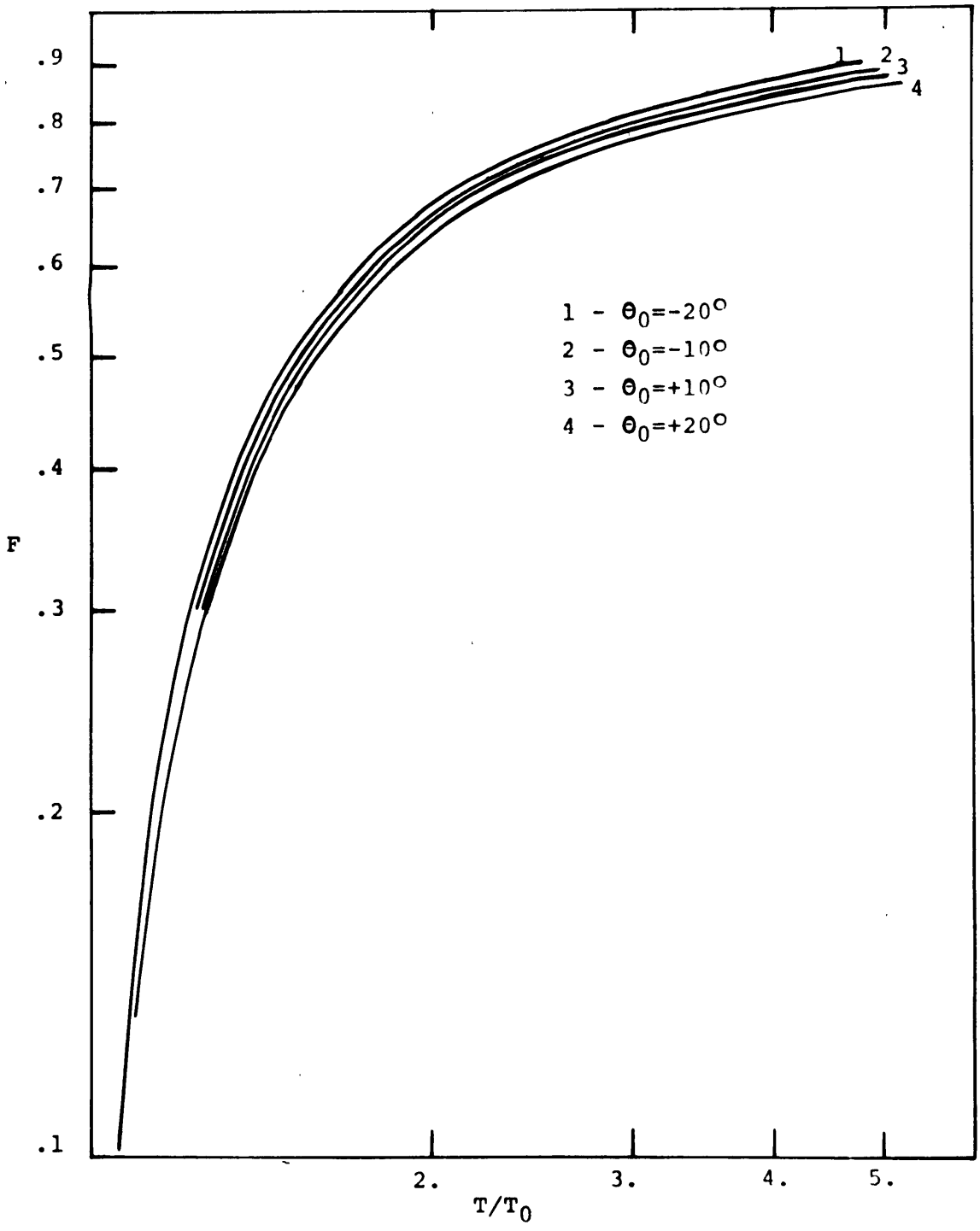

dispersion along the ray is less than that along the field line.

As an example, the emission of 4/13/66 0330/EST (section 1.4) has been interpreted with these curves and the results are presented in table 1.5.1.

Table 1.5.1

Interpretation of the events of 4/13/66, 0330/EST along several ray paths determined by the initial angle.

	-20^o	-10^o	10^o	20^o	dipole
f	1.14	1.21	1.26	1.30	1.18
L	7.5	7.3	7.25	7.2	7.4
T_o	132	132	131	131	134
n_e	3.2	3.7	4.1	4.5	3.6
$n_e 7.4$	3.3	3.5	3.7	3.9	3.6

Compared with the dipole field line model, the equatorial crossing points differ by up to 4 percent and the densities by as much as 8 percent. The errors introduced by assuming propagation along the field lines rather than the ray paths is probably not significant compared to errors arising from the measurement of the dispersion and from the curve fitting.

1.6 Propagation in the Magnetosphere

The interaction of the solar wind with the earths magnetic field results in a distortion of the dipole lines. On the daylight side the field is compressed and confined within a roughly hemispherical cavity. The high latitude field lines, those leaving the surface within 10 to 15 degrees of the poles, are swept back behind the earth to form the magnetospheric tail resulting in a compression of the field on the night side as well. As was mentioned in section 1.4, the distortion is not severe for field lines crossing the equator at distances less than 4 Re.

In this section the effects on the travel times due to the compression and distortion of the field will be investigated. Relative to a pure dipole, the compression results in an increase in the magnitude of the field at any distance and the distortion results in an increase in the arc length. The waves will still be considered as propagating along field lines.

The spherical harmonic expansion of the field which will be used here is taken from the work of Mead (1964). The components of the field are:

$$\frac{B_r}{B_o} = -\frac{2\sin\lambda}{R^3} + B_1^0 \sin\lambda - 2\sqrt{3}\, B_2^1 R \sin\lambda \cos\phi \qquad 1.6.1$$

$$\frac{B_\lambda}{B_o} = \frac{\cos\lambda}{R^3} + B_1^0 \cos\lambda + \sqrt{3} B_2^1 R (2\sin^2\lambda - 1)\cos\phi \qquad 1.6.2$$

$$\frac{B_\phi}{B_o} = +\sqrt{3} B_2^1 R \sin\lambda \sin\phi \qquad 1.6.3$$

where

$R = r/Re$

$B_1^0 = .2515/.314\ R$

$B_2^1 = .1215/.314\ R$

R_b = distance (in Re) to magnetopause at the subsolar point

ϕ = magnetic longitude ($\phi = 0$ at midnight)

The first terms in 1.6.1 and 1.6.2 give a dipole field and the second terms in these two equations give a constant field directed parallel to the dipole. The last terms and the term in 1.6.3 give a field which has a linear dependence on R. The field lines within the cavity can be obtained by numerically integrating the following set of equations.

$$\frac{dR}{ds} = \frac{B_r}{B} \qquad 1.6.4$$

$$\frac{d\lambda}{ds} = \frac{B_\lambda}{rB} \qquad 1.6.5$$

$$\frac{d\phi}{ds} = \frac{B_\phi}{r\cos\lambda\, B} \qquad 1.6.6$$

The travel time integral in 1.2.2 was evaluated for the P=4 density model making use of equations 1.6.1 through 1.6.6 and the results are shown in figures 1.6.1 through 1.6.4.

Figure 1.6.1 illustrates the changes in the dispersion between the midnight and noon meridians as a function of the equatorial crossing point of the lines (L parameter). As in the case of a pure dipole field, the dispersion in the

FIGURE 1.6.1
NORMALIZED DISPERSION - DISTORTED DIPOLE
MIDNIGHT AND NOON MERIDIANS

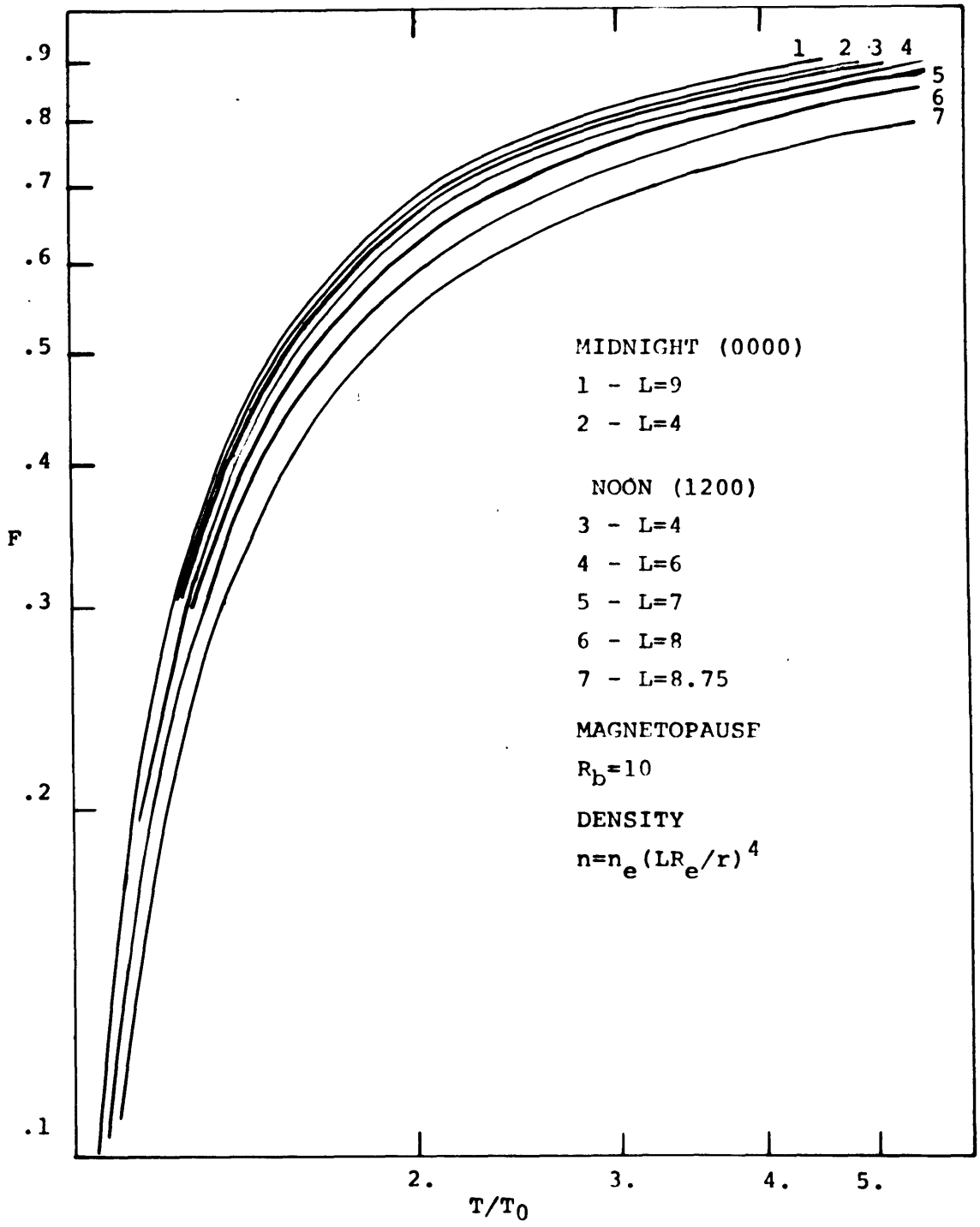

midnight meridian decreases slightly as the equatorial crossing increases. The distortion of the field lines in the midnight meridian is small and the dispersion for the distorted dipole in the worst case (9 Re) is within a few percent of that calculated for the pure dipole.

In the noon meridian the distortion of the field is more pronounced at distances greater than 4 Re and the dispersion is strongly affected. The variation in the curves for 4 Re between the midnight and noon meridians is less than 3 percent. The increase in the dispersion as the crossing point approaches the magnetopause is due to the distortion which results in an increase in the arc length and the variation of B along the lines which increases more slowly than in the pure dipole case (see Mead, 1964 Figures 4 and 7).

The calculations for the above curves have been carried out for a magnetopause radius of 10 Re. However the curves of relative dispersion (T/To vs F) are perfectly general and can be used by any magnetopause radius (Rb) provided the equatorial crossing points of the field lines are expressed in terms of the fractional distance to the boundary. In the above example (Rb = 10 R_e) the curve for 7 Re has an equatorial crossing point at .7 the radius of the boundary; for Rb=8 this curve would be appropriate for a field line crossing the equator at 5.6 Re.

In figure 1.6.2 the effects of local time are shown in more detail for the field line with an equatorial crossing of 7 Re. As would be expected the dispersion increases steadily in going from the midnight to the noon meridian.

Figure 1.6.3 is a plot of the ion gyrofrequency and the factor To $/\sqrt{n_e}$ as a function of the equatorial distance and the local time for the case Rb = 10. The gyrofrequency at

FIGURE 1.6.2
NORMALIZED DISPERSION ± DISTORTED DIPOLE
L=7 AS A FUNCTION OF LOCAL TIME

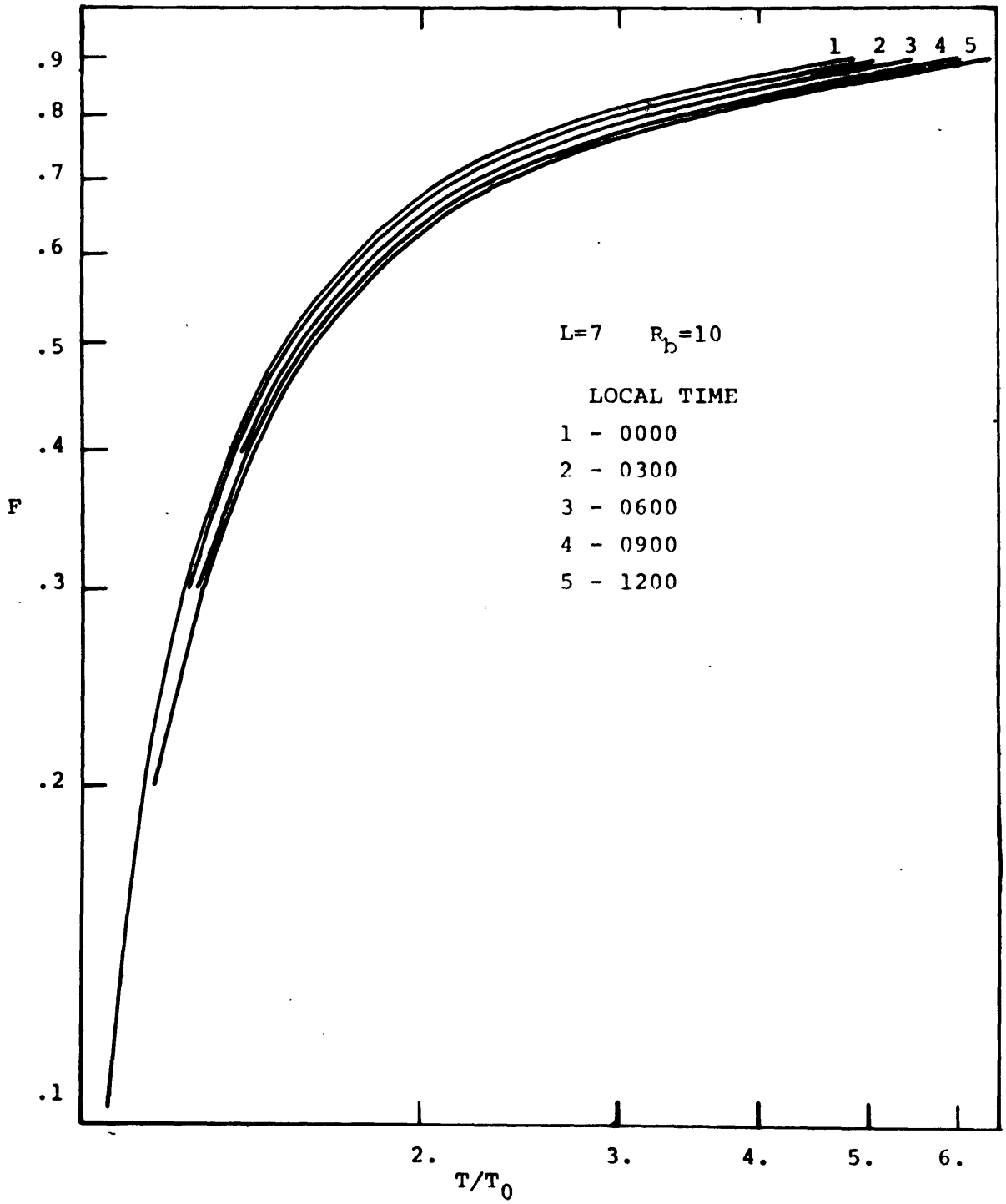

FIGURE 1.6.3

EQUATORIAL GYROFREQUENCY AND $T_0/\sqrt{n_e}$

AS A FUNCTION OF L AND LOCAL TIME

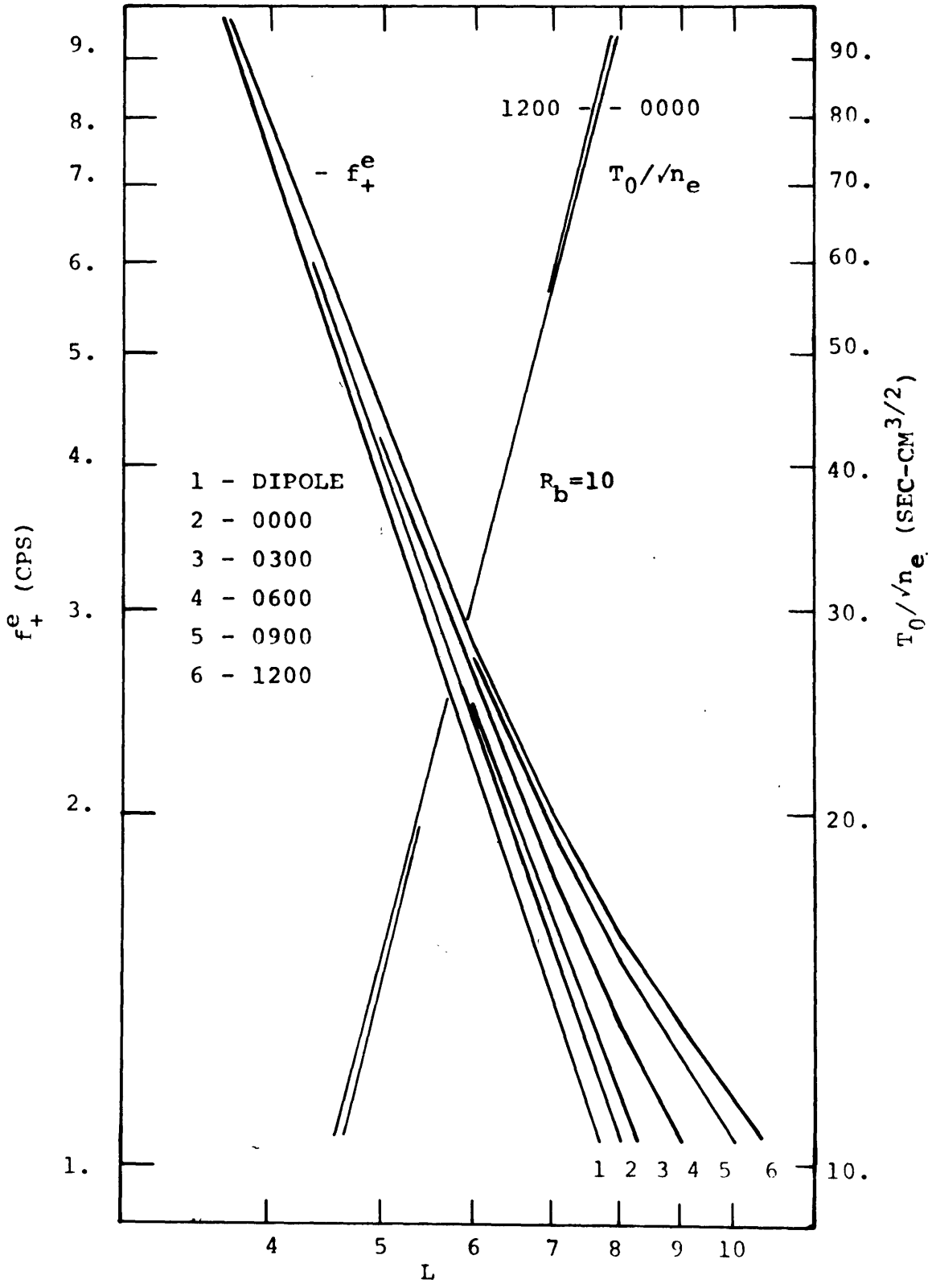

any distance increases with local time due to the compression of the field. To $/\sqrt{n_e}$ is practically independent of the local time and is only slightly less than that for a pure dipole. The insensitivity of To $/\sqrt{n_e}$ to the local time is the result of two effects which tend to cancel each other. These are an increase in arc length and an increase in velocity with local time. The field line crossing at 8 Re in the noon meridian has an arc about 10% greater and a field strength 50% greater than the 8 Re line in the midnight meridian. (Rb=10). In this case the increase in arc length is compensated by the increase in velocity to within about 2%.

In figure 1.6.4 are shown the gyrofrequency and To $/\sqrt{n_e}$ as a function of local time for Rb=8. The dependence of To$/\sqrt{n_e}$ on local time is more pronounced in this case than in the previous one but the difference at 7 Re is still less than 10 percent. The gyrofrequency is also shifted proportionately more for this example.

For most work moderate accuracy can be obtained by using the curves of To$/\sqrt{n_e}$ vs L for either the pure dipole or midnight meridian calculations. Since the one set of curves of T/To vs F can be scaled to any Rb, one then needs only to compute curves of f_+^e vs L (equation 1.5.2). In fact these curves can be determined from the calculation for any Rb, since the increase in gyrofrequency depends only on the fractional distance to the boundary. One graphical technique is the following. On a log-log overlay trace the pure dipole curve of f_+^e vs L from figure 1.6.2. Next shift the overlay keeping the pure dipole curves coincident until the vertical line for the new Rb falls on the underlying line for L=10. Tracing the remaining curves of f_+^e will produce the desired curves for the new Rb.

FIGURE 1.6.4

EQUATORIAL GYROFREQUENCY AND $T_0/\sqrt{n_e}$

AS A FUNCTION OF L AND LOCAL TIME R_b=8

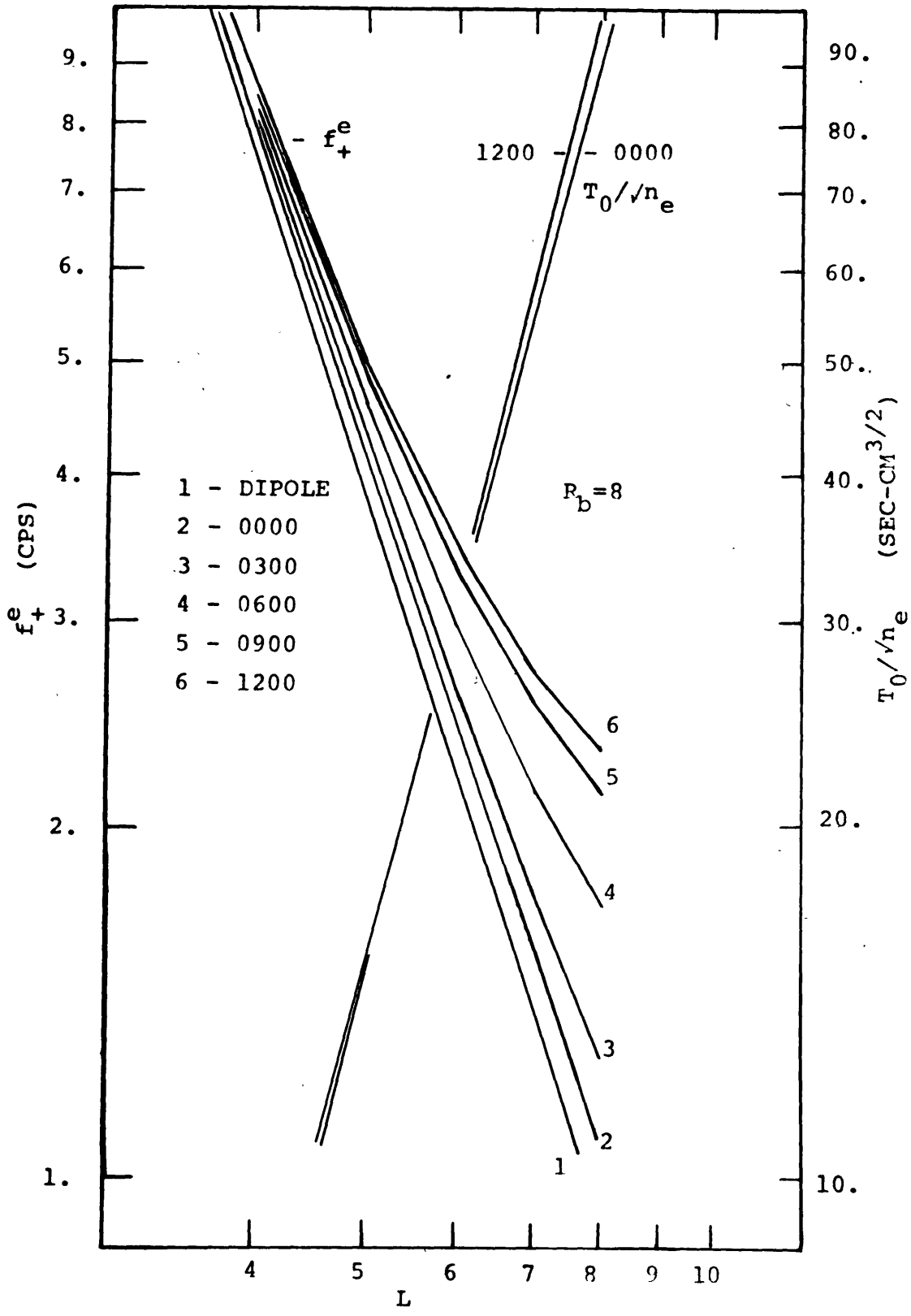

As an example of the differences that arise from the use of the various curves, let us consider the hydromagnetic emission of 4/13/66, 0330 EST which has been used as an example in section 1.4 and 1.5. The results are presented for various times in Table 1.6.1 where the magnetopause boundary was taken at 10 Re.

Table 1.6.1

Comparison of dipole and distorted dipole interpretations as a function of local time. R_b=10

		Local Time			
	Dipole	0000	0300	0600	1200
f	1.18	1.18	1.21	1.26	1.46
L	7.4	7.7	7.8	8.2	8.4
T_o	134	135	134	133	131
n_e	3.6	2.7	2.4	1.7	1.3
$n^{7.4}$	3.6	3.2	3.0	2.6	2.2

The increasing compression of the field lines from 0000 to 1200 results in an increasing equatorial gyrofrequency and L value while the calculated equatorial density decreases. The last line in Table 1.6.1 gives the calculated density extrapolated to a common datum of 7.4 Re. From this we see that the difference in density between the dipole interpretation and the distorted dipole increases from 15 percent at 0000 to 70 percent at 1200.

Using the pure dipole curves rather than the appropriate distorted dipole curves will result in L values which are too small and densities which are too large. Extrapolating the dipole density out to the appropriate L value still results in densities that are too large, (Table 1.6.1). Considering the errors involved in measuring the dispersion data and fitting it to the curves, one cannot hope for accuracy in determining n_e much better than 25 percent. Therefore, for local times within 3 or 4 hours or midnight or for events propagating within 5 or 6 Re, one would be justified in using the pure dipole curves.

Chapter 2

OBSERVATIONAL DATA

2.1 Data Collection

The micropulsation activity is measured by a telluric current recording system that monitors the voltage developed between lead electrodes situated in Concord, N.H. and 75 km to the NW in Etna, N.H. The geographic coordinates of the center of the telluric line are 43.5^{o}N, 72^{o}W corresponding to a geomagnetic latitude of 55.2^{o}N and an L parameter of 3.1. Electrical contacts are made between Etna, Concord and Cambridge by telephone lines. A high impedance preamplifier at Concord measures the voltage between the ground electrode at Concord and the electrode at Etna; this voltage is transmitted via telephone line to the MIT Geophysics Laboratory in Cambridge, Mass. Signals in the PC-1 band (0.1-2.0 cps) are amplified, rectified and averaged and the average amplitude as a function of time is continuously recorded on paper charts. During periods of increased activity in this band an alarm activates a FM tape recording system which then records the unrectified signals in a band from .01 to 3.0 cps. Events thus recorded are played back at a later time into an analogue to digital converter and are subsequently transferred to punched cards.

2.2 Data Analysis

In addition to the usual Fourier spectrum techniques the digitized data has been analyzed with a sonogram program developed by T. Madden. The sonogram or dynamic spectrum is a representation of the energy in a signal as a function of frequency and time. The three dimensional display of these quantities is achieved by plotting the energy (a number) as a function of frequency (vertical axis) and time (horizontal axis). The numbers representing energy level can then be contoured. The digital sonogram program duplicates with discrete data the same processes used by analogue devices to derive a dynamic spectrum; i.e. the signal is passed through a bank of narrow bandpass filters and the energy output of the filters is displayed as a function of time. In the case of the digital sonogram the discrete data is passed through 26 filters of constant Q with neighboring filters overlapping at the half power points. These 5 term digital filters approximate the 2 pole Chebyshev characteristics and are used in a recursive filtering technique similar to those discussed by Shanks (1967). The steps in the digital sonogram program are illustrated schematically in figure 2.2.1. The Q's of the filters, the sampling interval and the averaging time can be specified to obtain any desired display. Typical parameters for the sonograms used to analyze hydromagnetic emissions are; Q's from 25 to 100, sample time from 8 to 20 seconds, averaging time=1.5 sample time.

The printed output (figure 1.1.1,a) displays the frequency on the vertical axis and the time on the horizontal axis. The power/octave in this plane is expressed as a number in the following way, (Power/octave) K $10\frac{N}{2}$. The constant K is printed along with the labeling information and the scale

factors for the time and frequency axes at the beginning of the sonogram. With the power represented in this way an increment in N of unity represents 5 db and the dynamic range of the sonogram ($0 \leq N \leq 10$) is 50 db or 5 orders of magnitude.

FIGURE 2.2.1
SCHEMATIC DIAGRAM OF
DIGITAL SONOGRAM PROGRAM

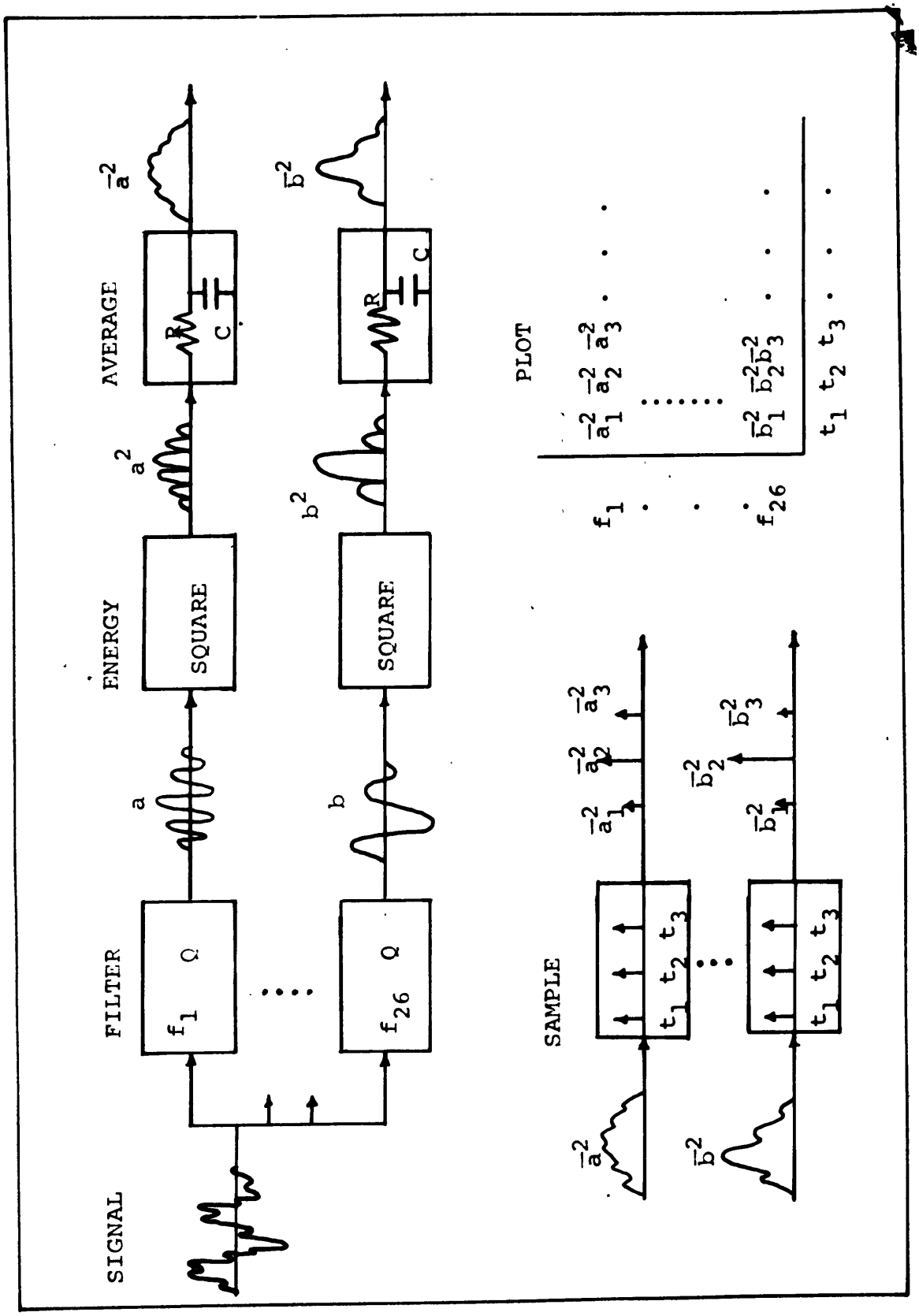

2.3 Some General Characteristics of Hydromagnetic Emissions.

Thirty-four hydromagnetic emissions have been recorded, digitized and analyzed for the interval of April, 1966 to July, 1967. Of these approximately half are of such a complicated nature that individual rising wave trains cannot be observed in the sonograms. Several of these complicated events are of large amplitude and long duration. The complicated nature of these events may be due to the addition in the ionospheric waveguide of signals from hydromagnetic emissions generated on a number of different field lines.

A few events are of such a narrow bandwidth that the dispersion between the high and low frequencies is not measurable. Thirteen events show a measurable amount of dispersion and these will be discussed in more detail in sections 2.4 and 2.5.

In general most of the events occurred during periods of moderate geomagnetic activity as can be seen from figure 2.3.1.

Figure 2.3.1

The number of Hydromagnetic Emissions as a function of Kp

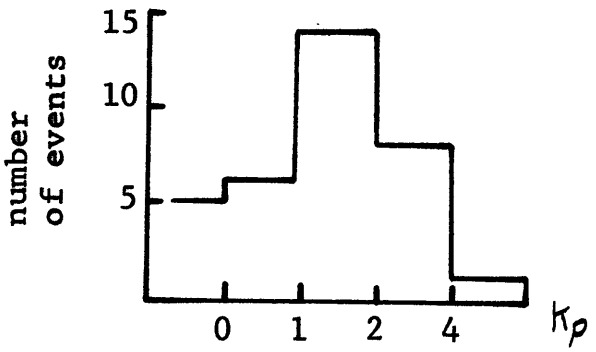

About 75 percent of the events fall in the range of Kp from 0 to 2. and 95 percent for Kp less than 4..

Continuous recordings of the telluric signals in the range from DC to 1 cps are made at the M.I.T. Geophysics Laboratory and a two day segment of this data is shown in figure 2.3.2. Four bands of signals are shown. The top two records for each day are the direct A.C. signals for the bands DC - .002 cps (Pc5), and .001 - .03 cps (Pc4). The lower two records are the rectified and averaged amplitudes in the bands .02 - .2 cps (Pc2-3) and .2 - .8cps (Pc1).

On 9/10/66 at 0115EST a hydromagnetic emission occurs during a period of moderate activity (Kp=2); note the very rapid increase in amplitude and the simultaneous increase in the amplitude of the Pc 2-3 band (.02 - .2 cps). Later on this same day at 19:35 an event of 4 hours duration begins. This emission occurs in an interval between two large low frequency disturbances (Kp=3) at 1900 on 9/10/66 and 0030 on 9/11/66 there is little correspondence between the amplitudes in Pc1 band and the lower frequencies except for the event at 2300 which is accompanied by pulsations in the Pc4 band (.001 - .03 cps).

Figures 2.3.3 through 2.3.12 contain six hour segments of the four frequency bands of telluric data. Note in figure 2.3.3 (10/13/66) that during the hydromagnetic emission (0500) the amplitude in the Pc2-3 band decreases. Another event showing this characteristic is presented in figure 2.3.4. There is an abrupt decrease in the Pc2-3 activity at the point (1507) where the hydromagnetic emission begins. In addition this event ends shortly after an increase in the Pc4 band around 1700.

Two events exhibiting a concurrent increase in the Pc2-3 band are shown in figures 2.3.5 and 2.3.6. The first example

is unusual in that it begins before and lasts through the period of a negative bay.

Figures 2.3.7 through 2.3.9 show 3 events during which very little Pc2-3 activity was present. The event on 4/29/66 occurs during a very quiet period (Kp=0) with no noticeable changes in the Pc2-3 and Pc4 activity. Figure 2.3.8 shows an event which occurred during a period of moderate activity (Kp=2). The hydromagnetic emission in figure 2.3.9 spans a period of moderate to quiet conditions (Kp from 3 to 1) and it is accompanied during its first part by large oscillations in the Pc4 range. There is also a short period of simultaneous activity in the Pc-1 and Pc4 bands at 2300.

The records for several emissions during periods of moderate to strong activity are presented in figures 2.3.10 through 2.3.12. The event of 4/13/66 (figure 2.3.10) is accompanied by several short bursts of activity in the Pc2-3 and Pc4 bands. On 9/9/66 (figure 2.3.11) at 1800 the emission begins during a period of low amplitude in the Pc2-3 band and decreases as the activity in this band builds up. After the large negative pulse in the Pc5 band the emission amplitude increases while the Pc2-3 activity slowly decreases. The events during the night of 7/10/67 (figure 2.3.12) took place during a period of moderate activity (Kp=3). The first and last events in this figure show some concurrent Pc2-3 activity.

We see then that there are no hard and fast relationships between hydromagnetic emissions and the activity in the other Pc bands. The two most dramatic cases (9/10/66 at 0115 and 10/13/66) show opposite relationships. The event of 9/10/66 indicates a definite increase in the Pc2-3 band during the

emission and the event of 10/13/66 shows a definite decrease in the Pc2-3 activity for the duration of the emission. This type of association might be the result of damping of the Pc2-3 waves by the particles responsible for the emission. It might also be that the Pc2-3 waves are capable of supressing hydromagnetic emissions through wave-particle interactions that disturb the particle distribution function (i.e. decrease the pitch angle anisotropy). In this case a sudden decrease in the Pc2-3 wave energy could lead to conditions favorable for the generation of hydromagnetic emissions.

Since so few events were recorded during the daylight hours no meaningful diurnal variation of the emission frequencies can be determined. There is, however, a noticeable tendency, within events of long duration, for the band of the emission to shift to higher frequencies with time when the events occur before midnight. For those events occuring after midnight the tendency is for a shift to lower frequencies. See for example the sonograms in the next section for 4/29/66 (figure 2.4.1) and 5/20/66 (figure 2.4.2). This shift in frequency is in agreement with results presented in the literature which indicate that both the lower limit and the overall band of emissions are at a maximum frequency near midnight and shift to lower frequencies during the daylight hours. (Manchester, 1966; Kenney and Knaflich, 1966).

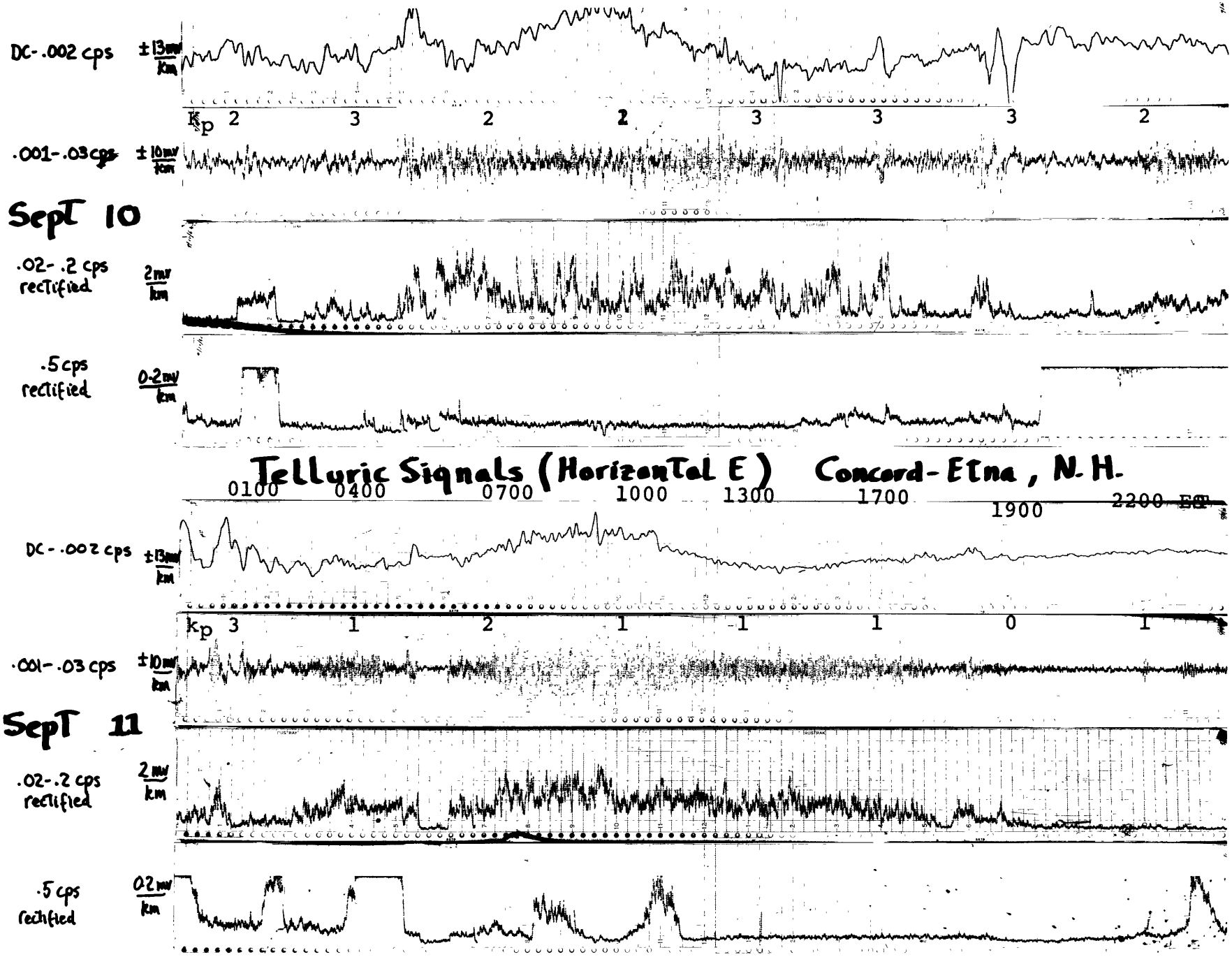

FIGURE 2.3.2
TELLURIC RECORDS 9/10-11/66

FIGURE 2.3.3

TELLURIC AMPLITUDE VS TIME RECORDS

10/13/66

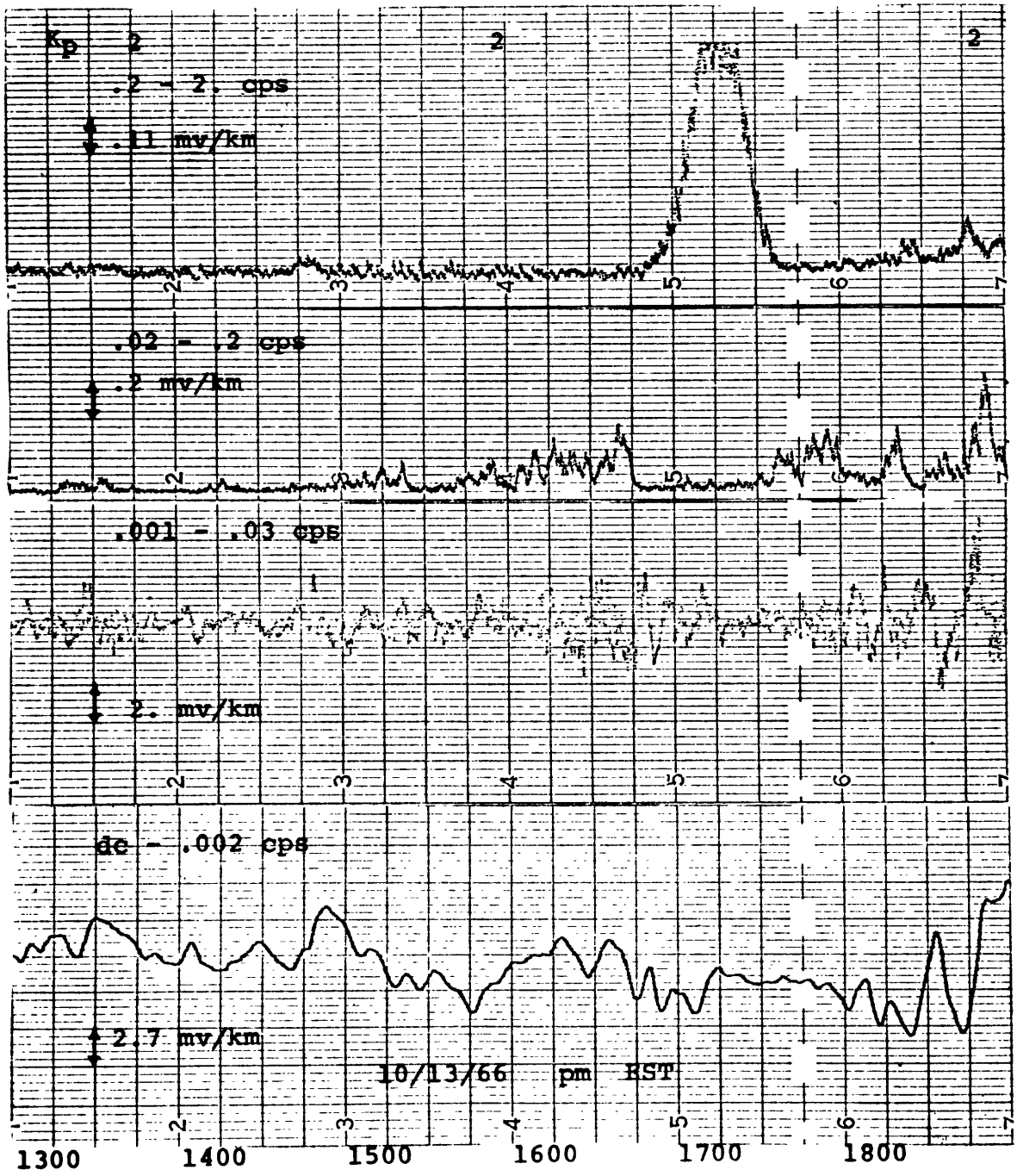

FIGURE 2.3.4

TELLURIC AMPLITUDE VS TIME RECORDS

11/2/66

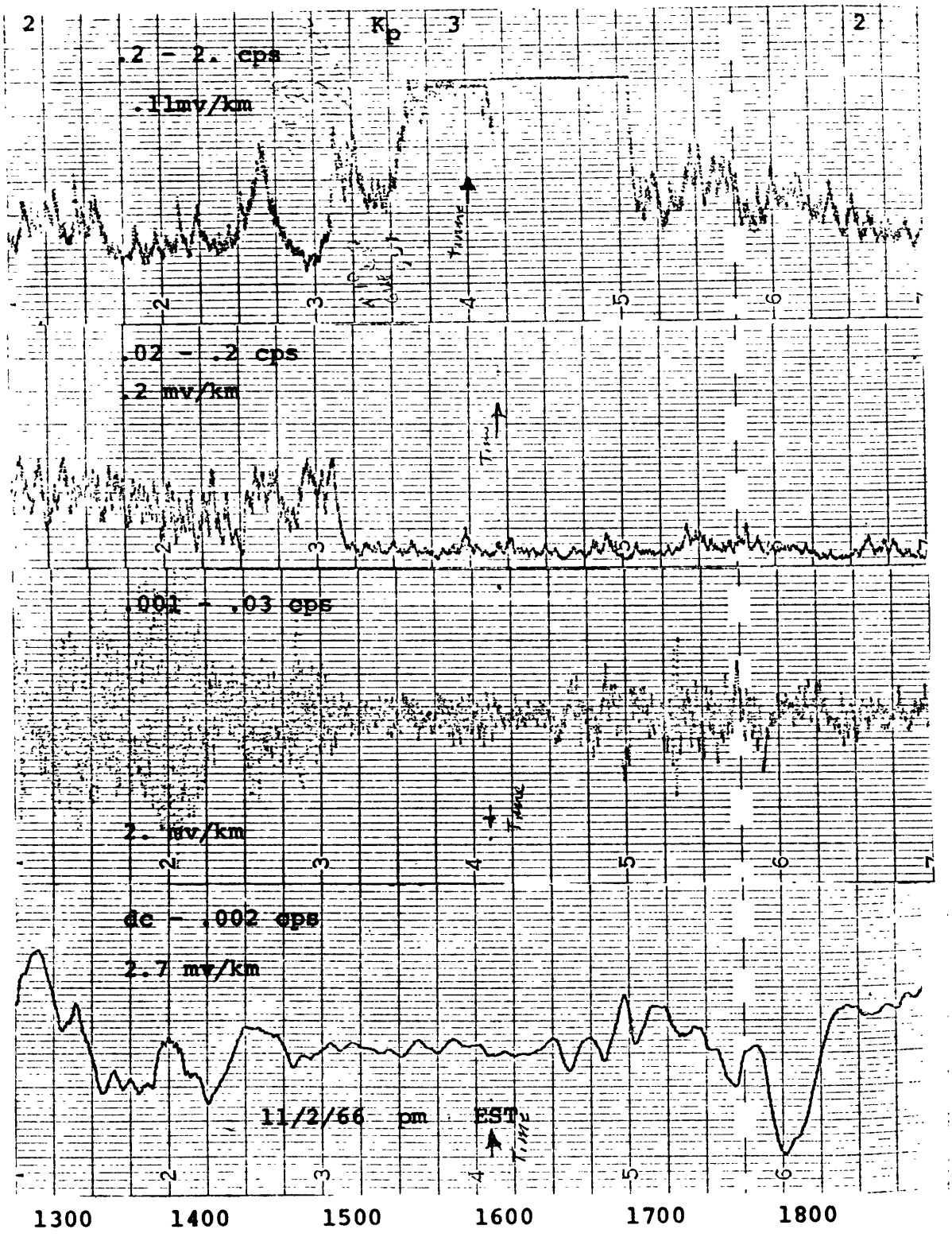

FIGURE 2.3.5
TELLURIC AMPLITUDE VS TIME RECORDS
1/28/67

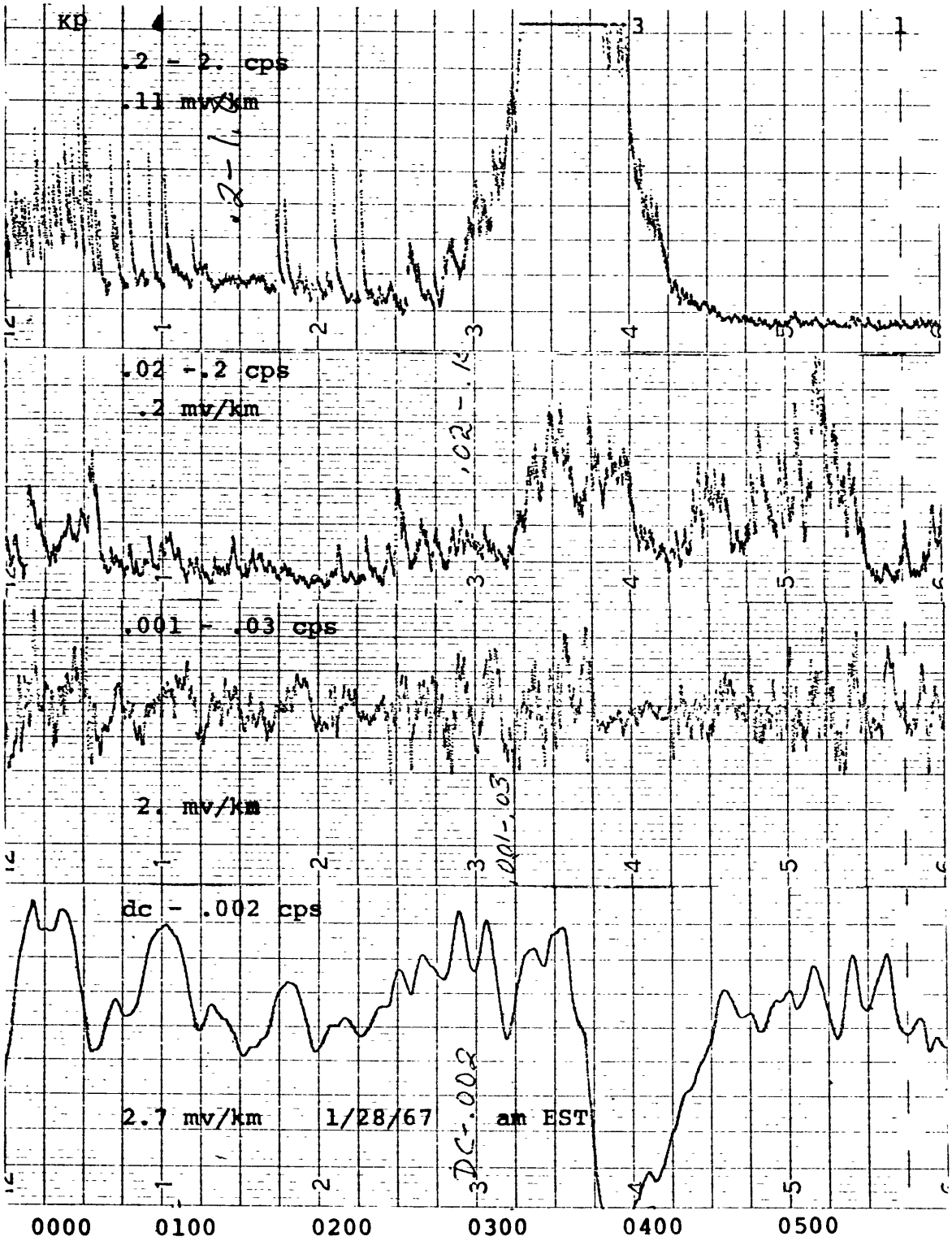

FIGURE 2.3.6
TELLURIC AMPLITUDE VS TIME RECORDS
7/8/67

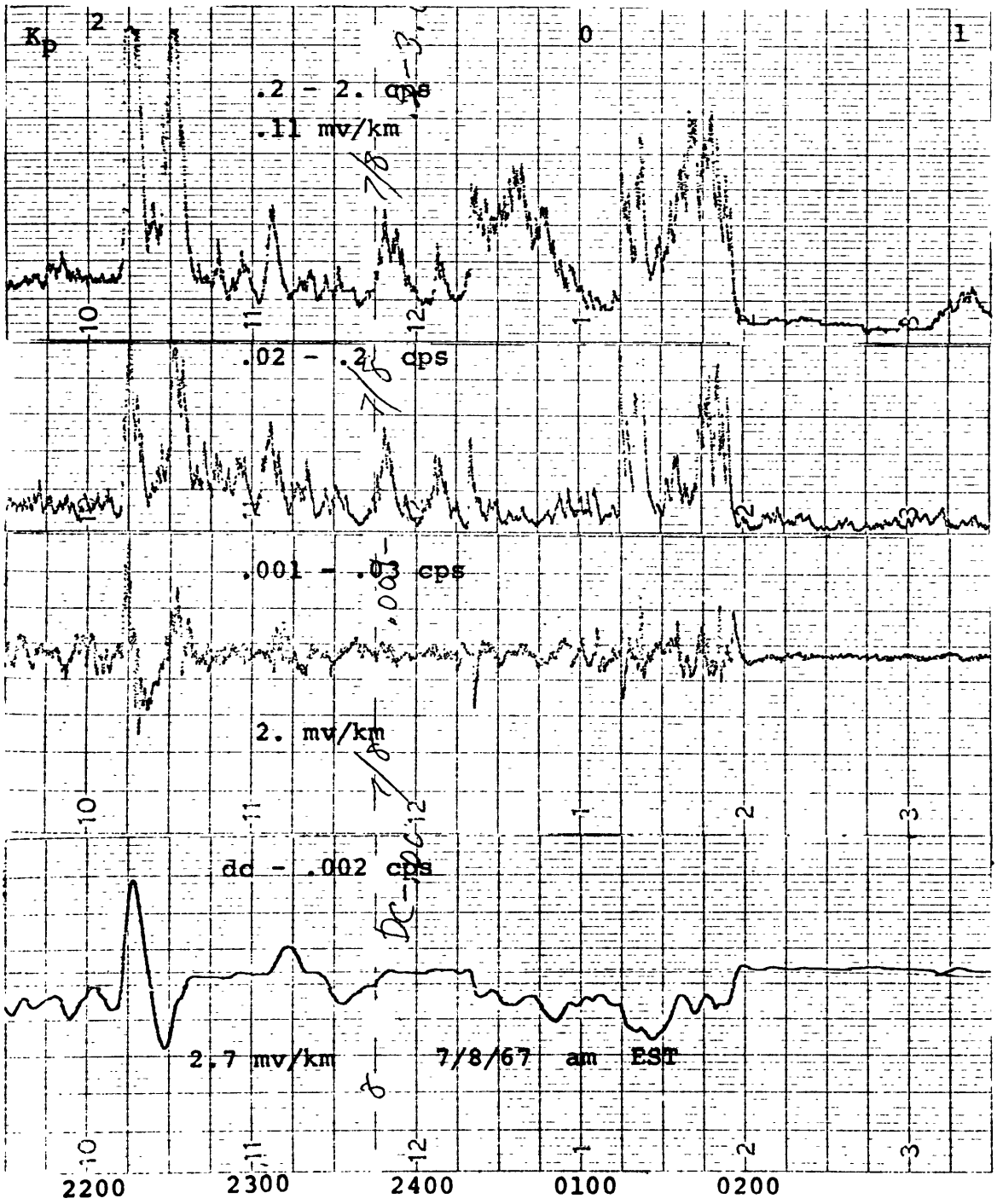

FIGURE 2.3.7
TELLURIC AMPLITUDE VS TIME RECORDS
4/29/66

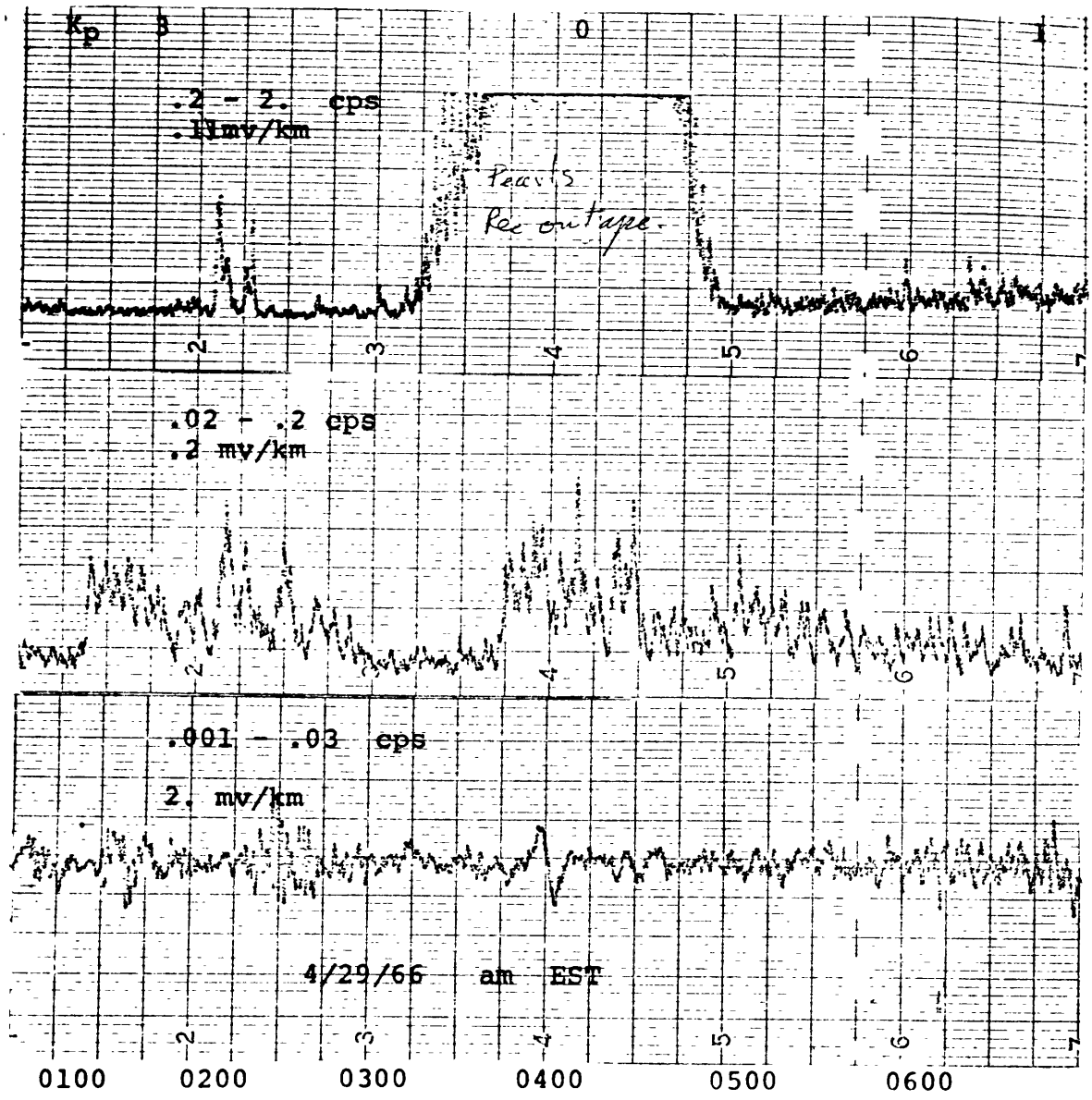

FIGURE 2.3.8

TELLURIC AMPLITUDE VS TIME RECORDS

5/17/66

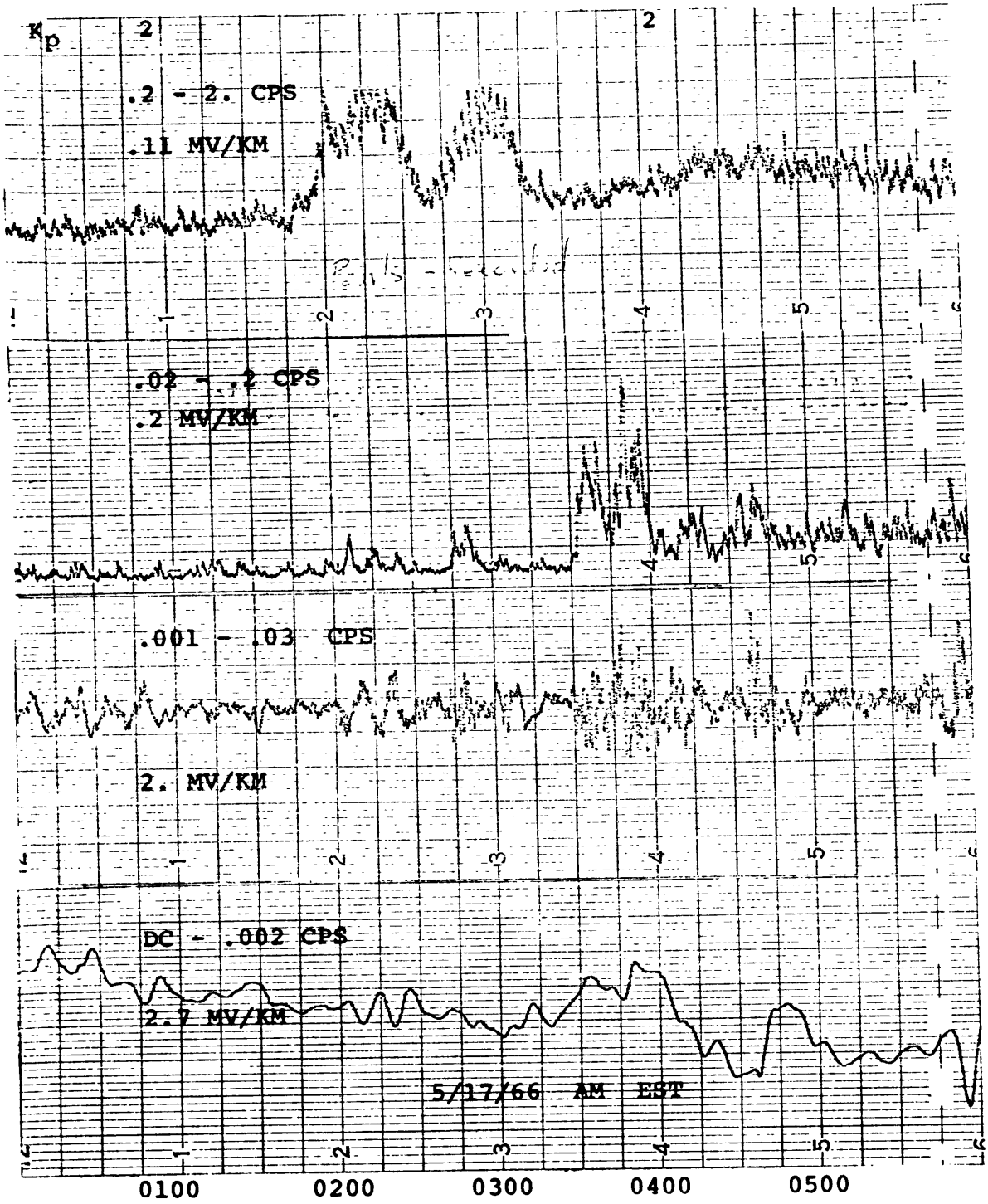

FIGURE 2.3.9
TELLURIC AMPLITUDE VS TIME RECORDS
5/20/66

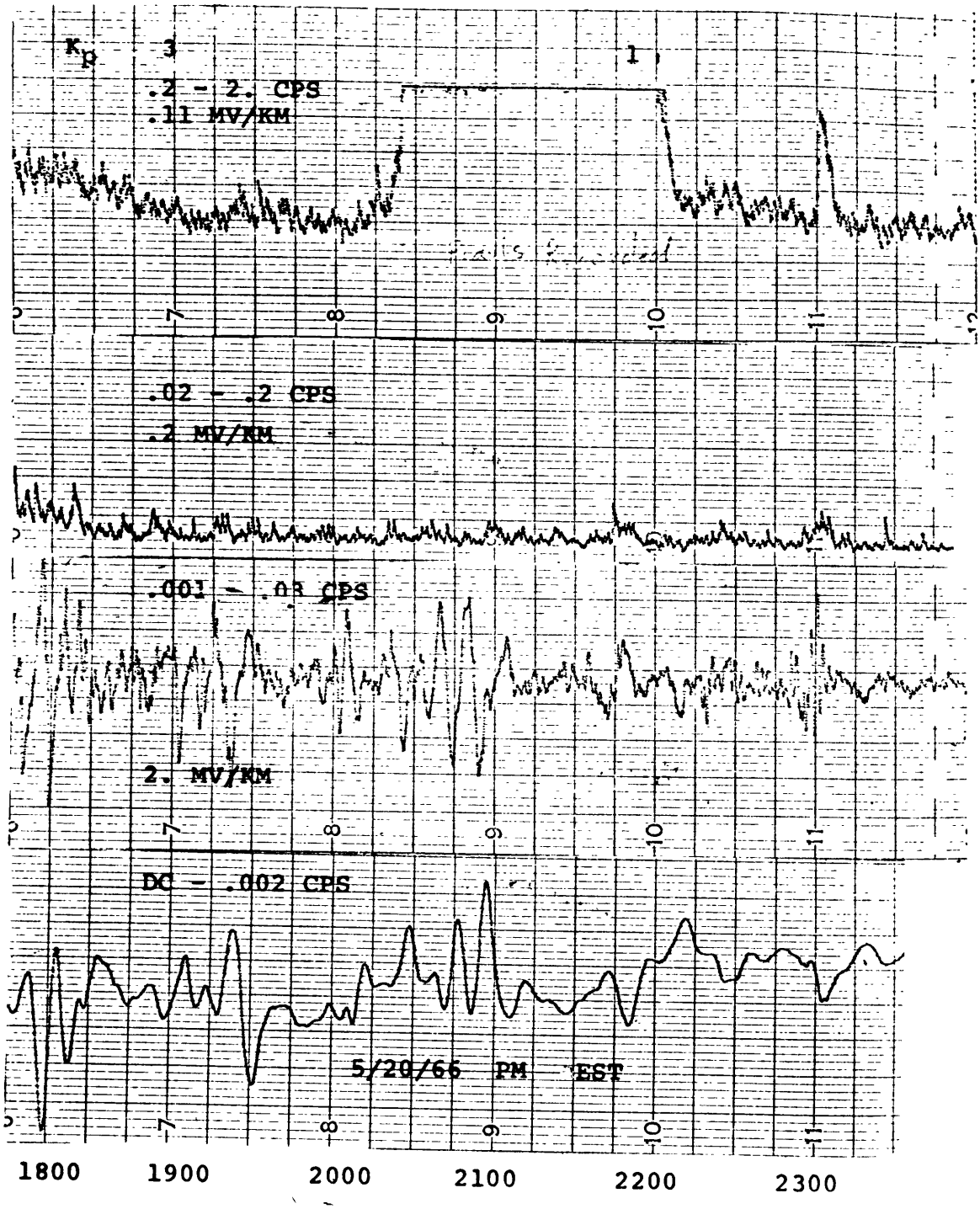

FIGURE 2.3.10

TELLURIC AMPLITUDE VS TIME RECORDS

4/13/66

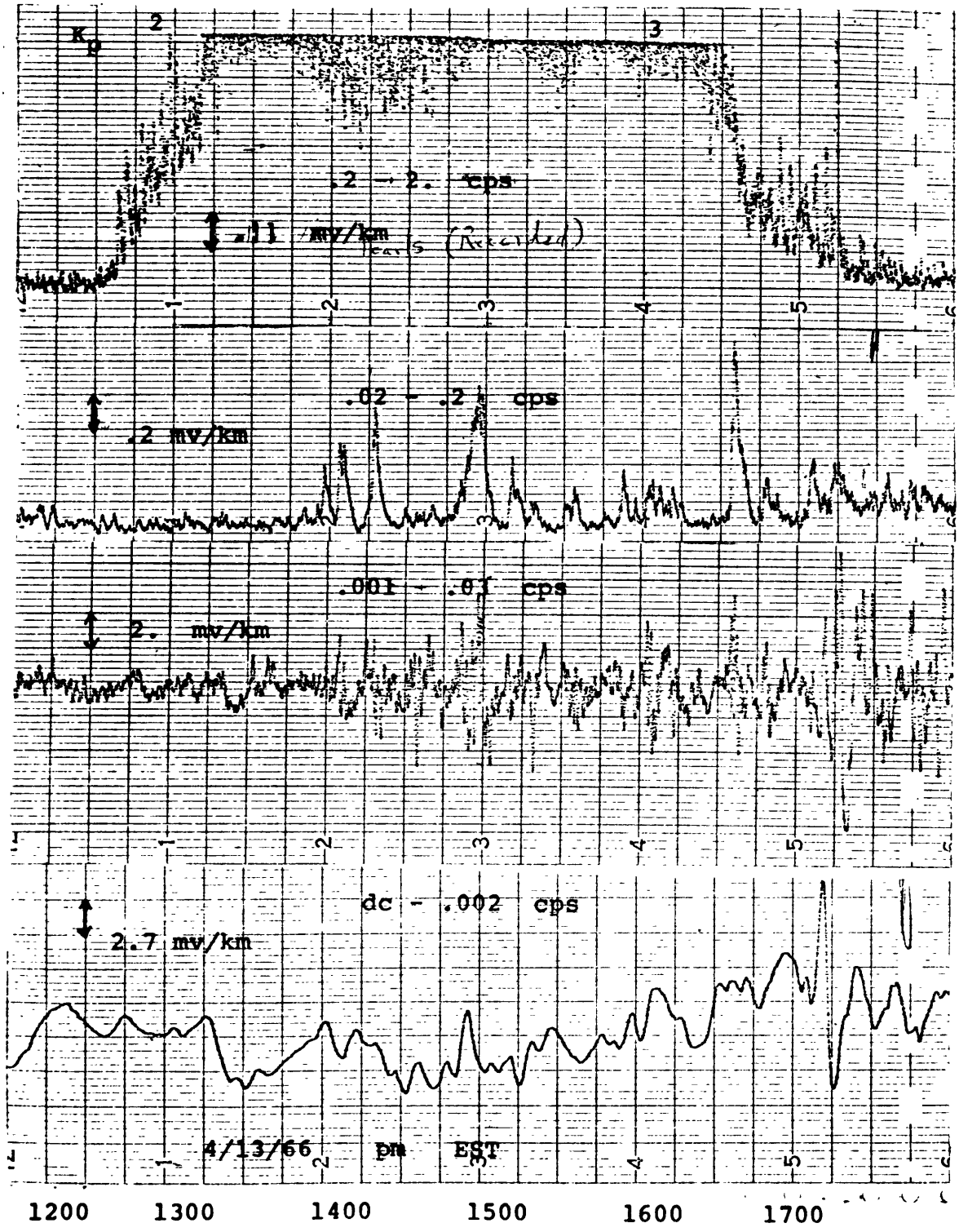

FIGURE 2.3.11

TELLURIC AMPLITUDE VS TIME RECORDS

9/9/66

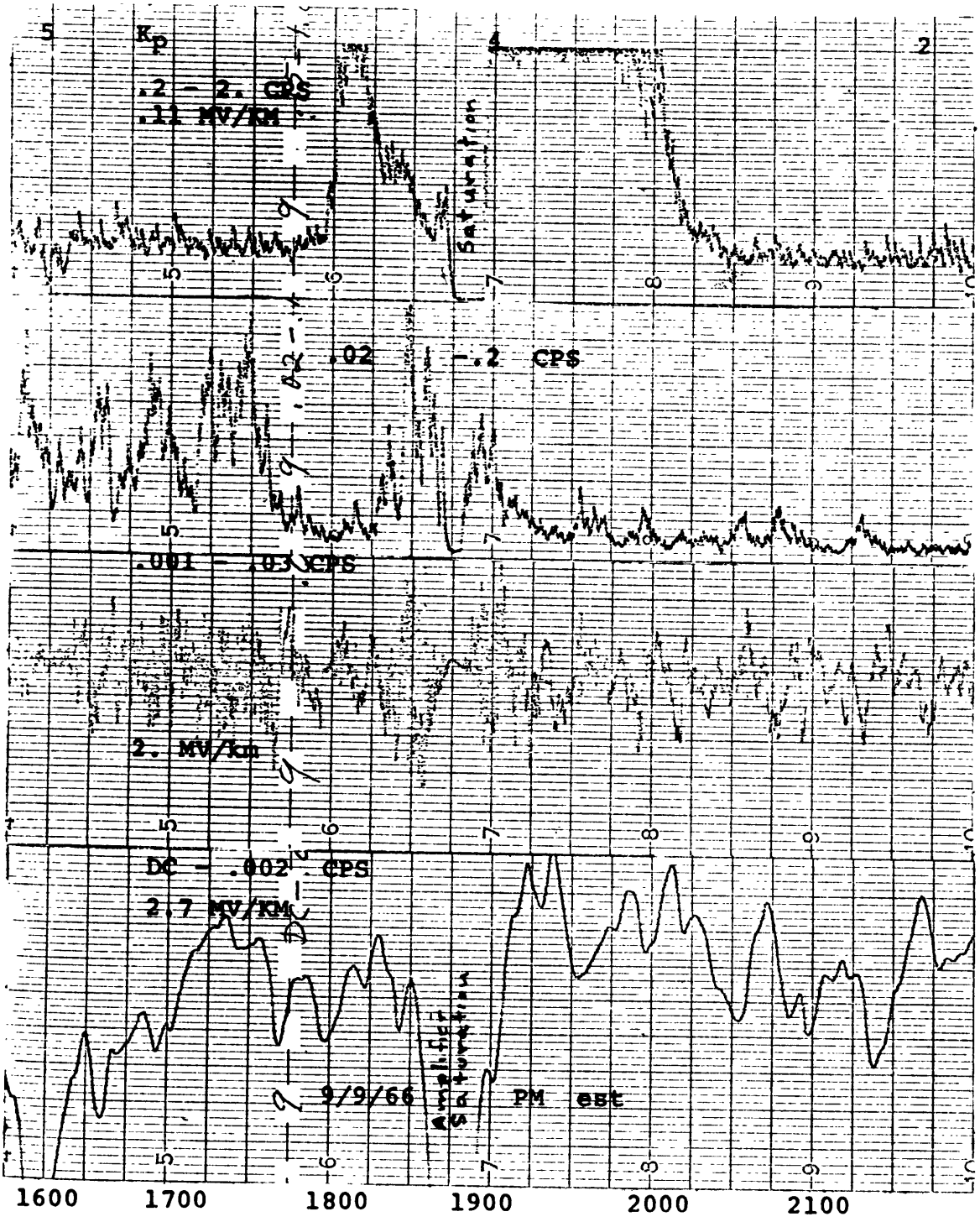

FIGURE 2.3.12
TELLURIC AMPLITUDE VS TIME RECORDS
7/10/67

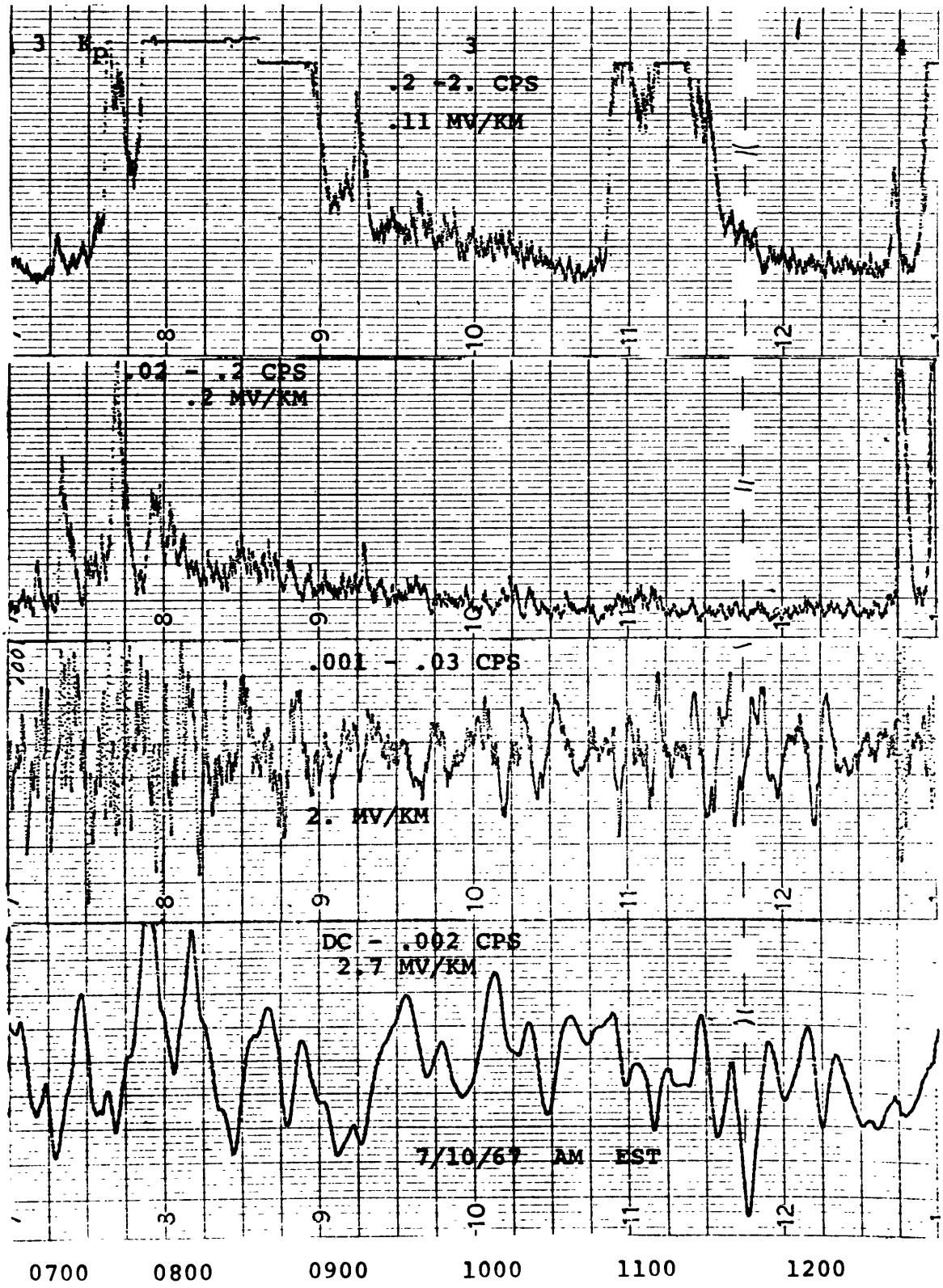

2.4 Sonograms and the Fine Structure in the Spectra of Hydromagnetic Emissions.

The sonogram of a well dispersed hydromagnetic emission has been presented in figure 1.1.1a. The rising wave trains in this event are readily apparent and the frequency fine structure manifests itself by the beadlike appearance (closed power contours) along the locus of the rising wave trains. This distribution of the energy at discrete frequencies within the individual wave trains is seen in figures 2.4.1 and 2.4.2.

In addition to the above sonogram display, the digital sonogram program also computes the spectra over longer time intervals by summing the sonogram output for 10 sampling intervals. Since the usual sample interval for the sonograms presented here are 8, 10 or 20 seconds these spectra cover 80, 100 or 200 second periods; a time span which is of the order of the length of one wave train.

The appearance of the frequency fine structure in these spectra are seen in figures 2.4.3 through 2.4.5. Figure 2.4.3 presents three 80 second averages sonogram spectra for the event of 10/4/66 (0500 EST). Note that some peaks are present in all three spectra and that some increase in energy with time (the peak at .86 cps) and others decrease (peaks at .915 and .945 cps). The frequencies of the peaks and the separation between the peaks are presented in Table 2.4.1

FIGURE 2.4.1

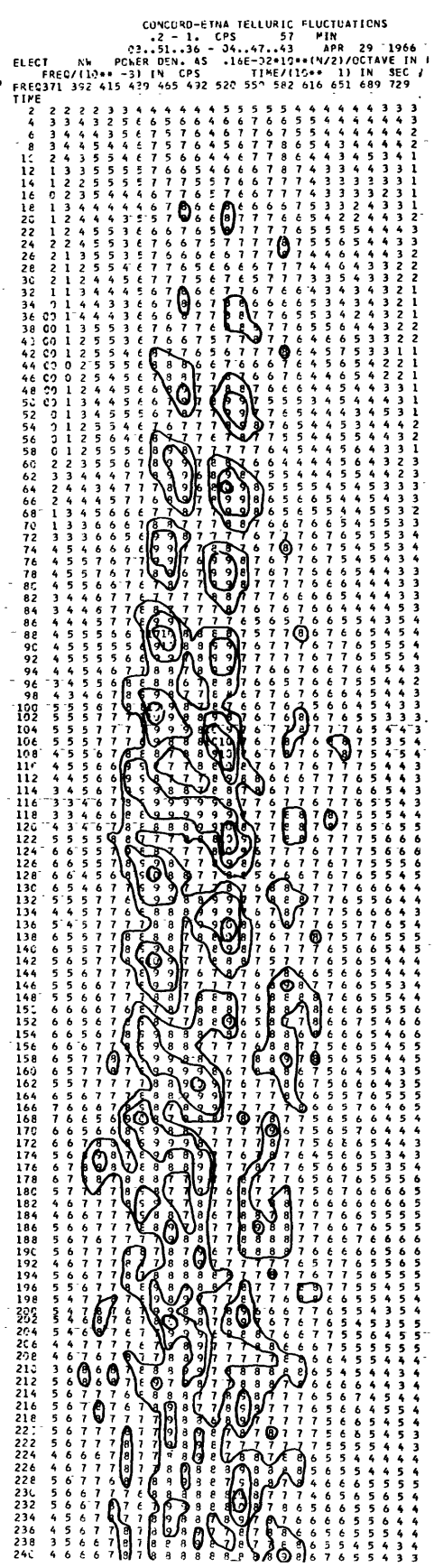

DIGITAL SONOGRAMS

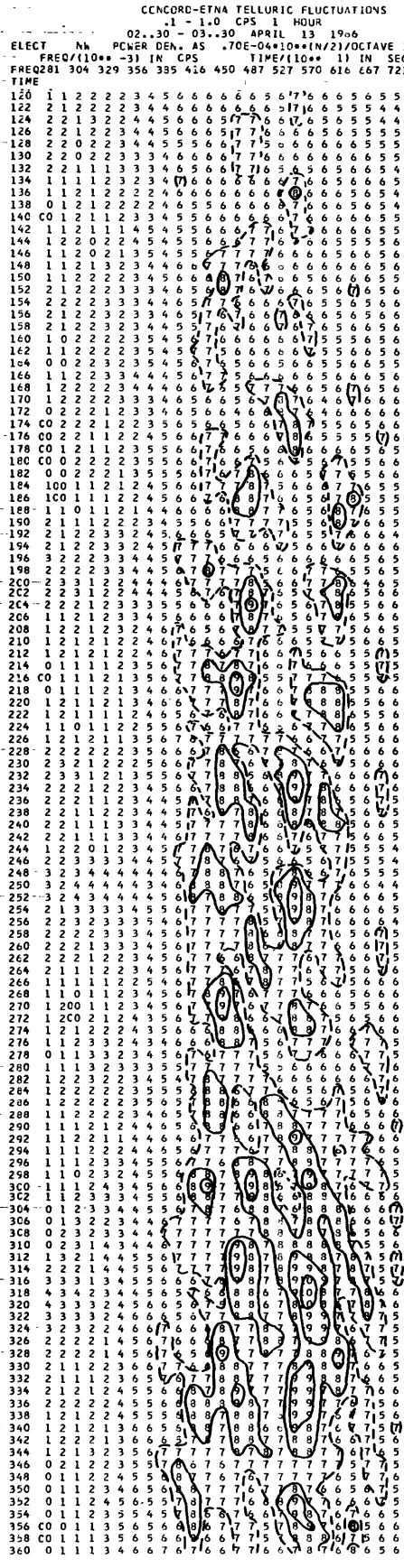

FIGURE 2.4.2

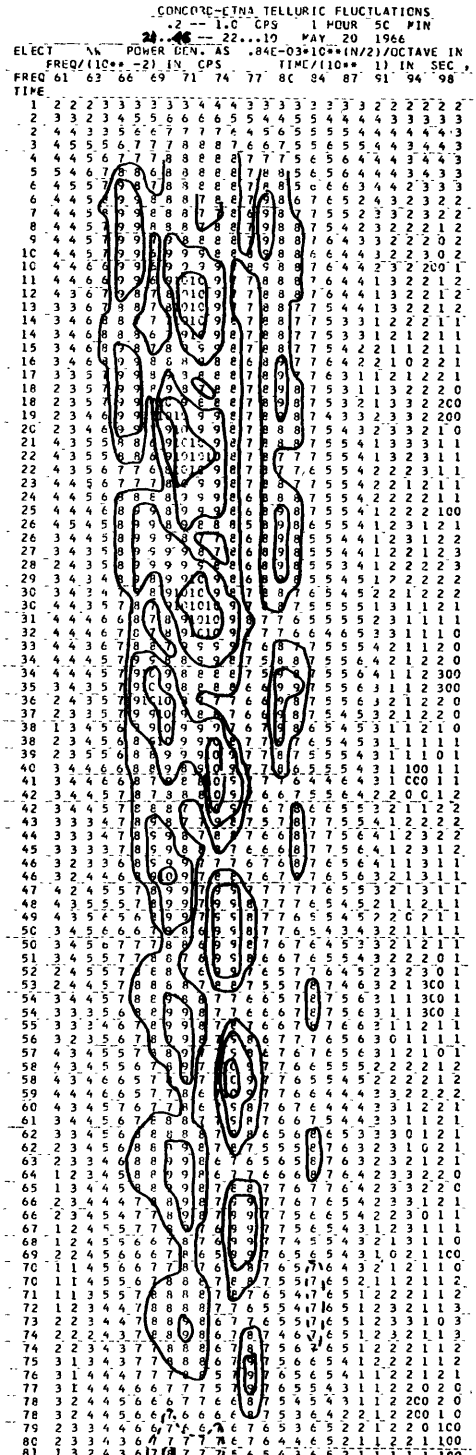

DIGITAL SONOGRAMS

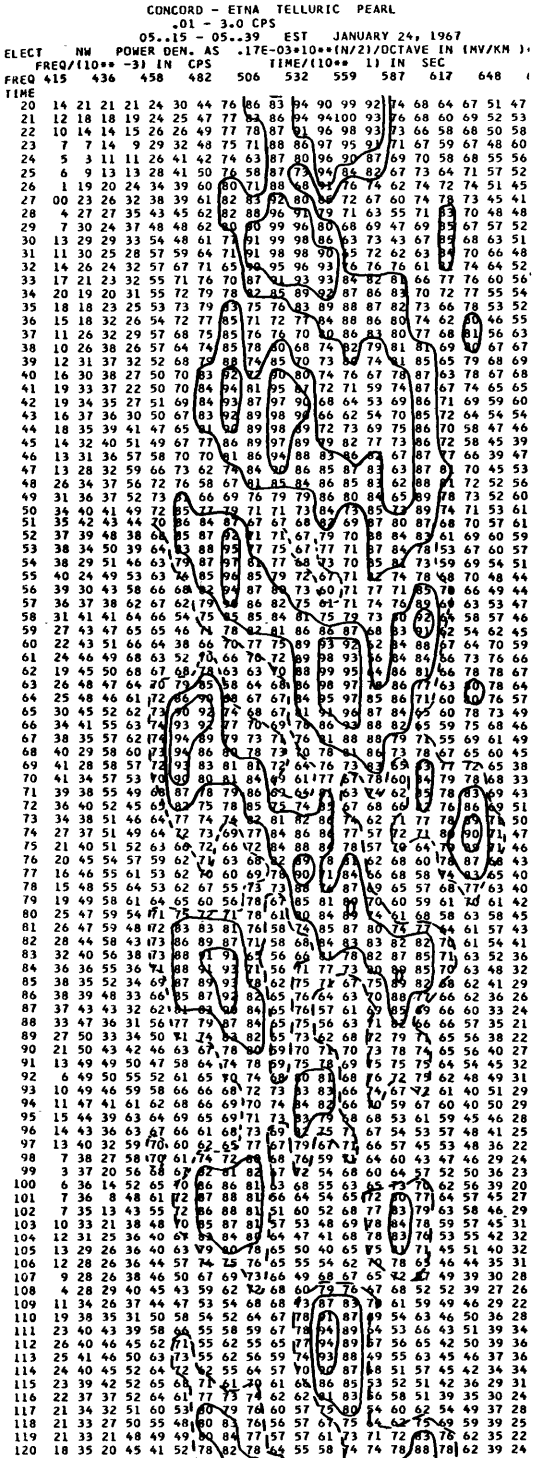

FIGURE 2.4.3

SPECTRA OF THE EMISSION OF 10/4/66

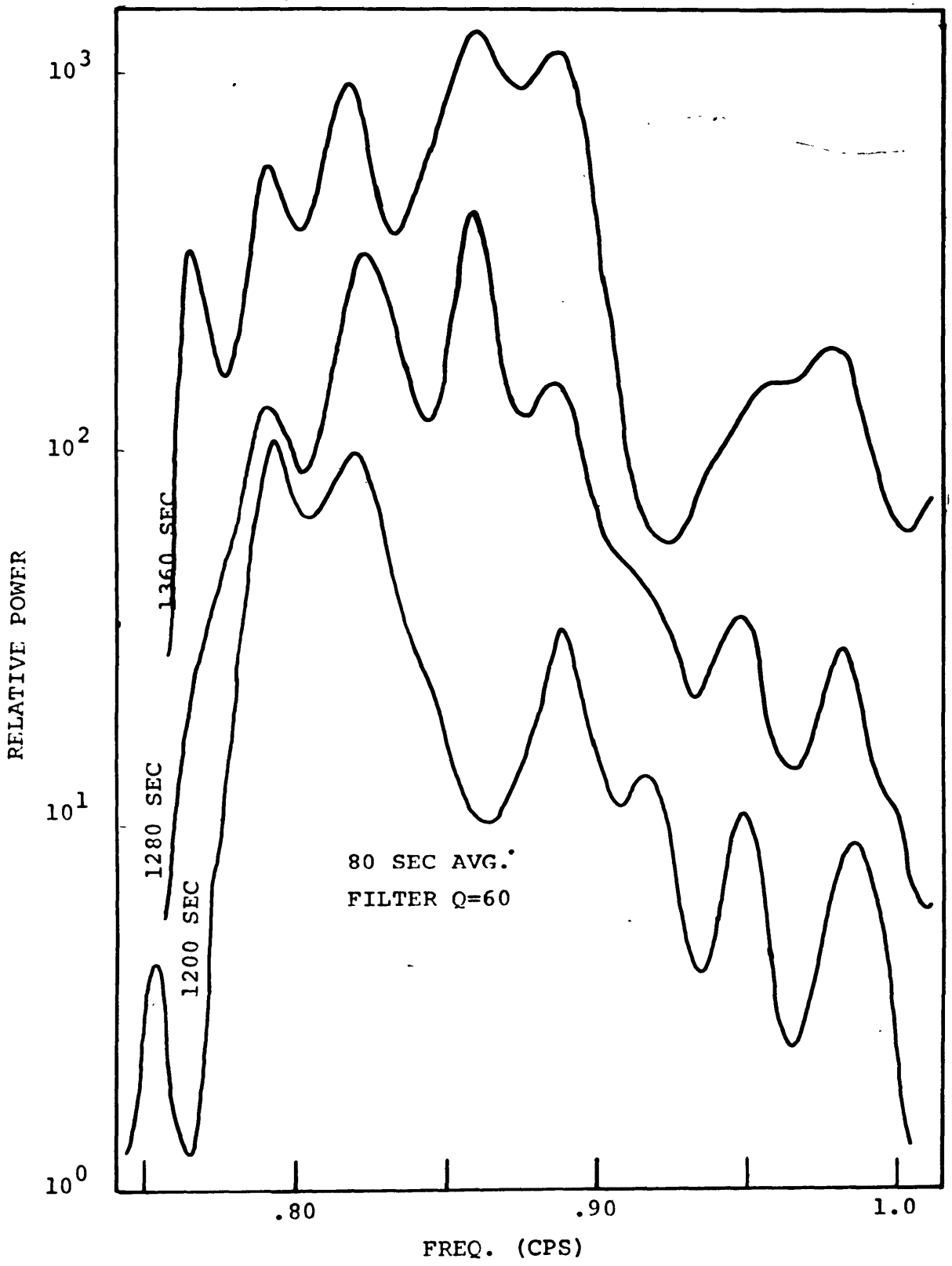

Table 2.4.1

Peak frequencies in the emission of 10/4/66 (0500/EST)

1200 sec		1320 sec		1400 sec	
f	Δf	f	Δf	f	Δf
.755				.765	
.792	.037	.790		.790	.025
.820	.028	.820	.030	.817	.027
		.857	.037	.857	.040
..888	.068	.888	.031	.888	.031
..917	.029	.915	.027		
.947	.030	.945	.030	.945	.057
.985	.038	.980	.035	.980	.035
1.015	.030	1.010	.030	1.005	.025
	.032		.033		.030

It is obvious in Table 2.4.1 that the dominant separation of the peaks is of the order of .03 cps. Taking into account that some of the larger separations are caused by the absence of a peak which is present in the adjoining spectra the average separations for the three spectra are .032, .033 and .030 cps. The dispersion measurements for this event indicate a nondispersive travel time (T_o) of 70 seconds (Table 2.5.1). In this

case the observed separation is given approximately by $2/T_o$ = .029 cps.

Measurements of the dispersion and the fine structure of a number of emissions showed that the average separation between the peaks was of the order of $2/T_o$. However, many events exhibit a fine structure which is not so regular as shown in figure 2.4.3. In these events separations of the order of $2/T_o$, $3/T_o$ and $4/T_o$ are seen. Some examples of this type of structure can be seen in the remaining figures.

It is important not to confuse the fine structure reported here with that caused by the repetative nature of a series of wave trains (T. Madden, 1964). In the latter case the periodicity at the group travel time (T (F)) will introduce a fine structure in the spectra with a separation of $\Delta f=1/T(F)$. This type of fine structure is apparent only in the spectrum of a series of wave trains, while the fine structure seen in the sonograms is visible within the individual wave trains.

Figure 2.4.4 shows two spectra for the first dispersed event of 4/13/66 (0130EST). The upper spectrum is for filter Q's of 25 and the lower for Q's of 50. As can be seen the lower Q spectra do not give an adequate picture of the number or the sharpness of the peaks. It would be helpful in this respect to analyze all the data with filters of high Q. However, certain problems can develop when this is attempted. There are two sets of information we would like to determine from the sonograms. The first is to measure the dispersion on suc-

FIGURE 2.4.4

SPECTRA OF THE EMISSION OF 4/13/66

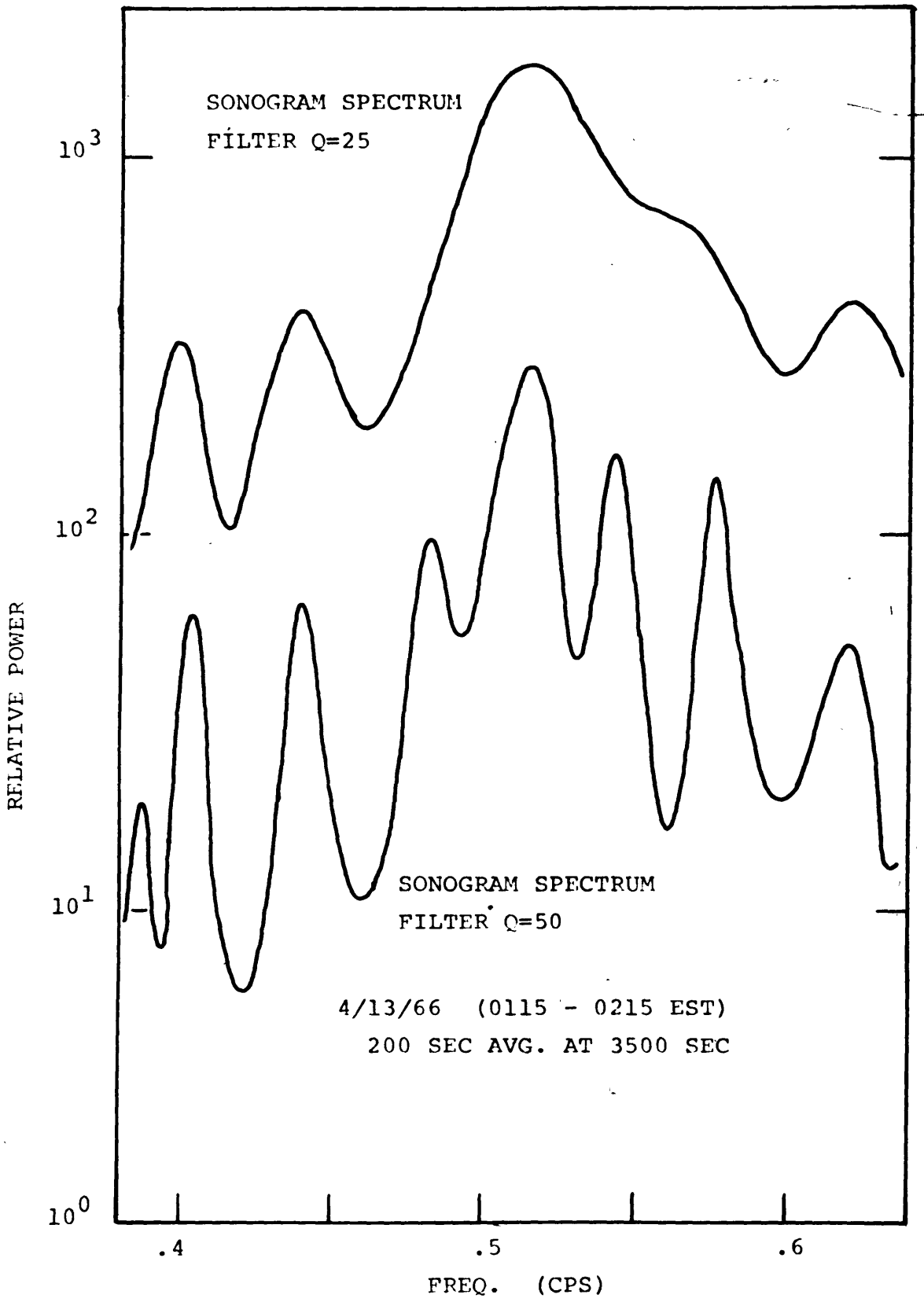

cessive wave trains (time resolution); and the second is to resolve the fine structure (frequency resolution). When the Q's are large the ringing of the filters (the decay constant is $\tau = Q/\pi f$) can smear together the signals from the individual wave trains and the time resolution will be lost. The Q's of the peaks in figure 2.4.4 are of the order of 25 to 50. The frequencies of the peaks are given in Table 2.4.2.

Table 2.4.2
Peaks of event of 4/13/66

f	Δ f
.402	.
.440	.038
.480	.040
.515	.035
.542	.027
.575	.032
.620	.045
.650	.030

The dispersion measurements for this event give T_o = 129 sec. The peaks in Table 2.4.2 have separations corresponding to $4/T_o$ (.031), $5/T_o$ (.039) and $6/T_o$ (.046). In this case although the fine structure is well developed it does not appear to correspond to as simple as a relation as the first example (10/4/66) where the separation between peaks was given by $2/T_o$.

FIGURE 2.4.5

SPECTRA OF THE EMISSION OF 4/29/66

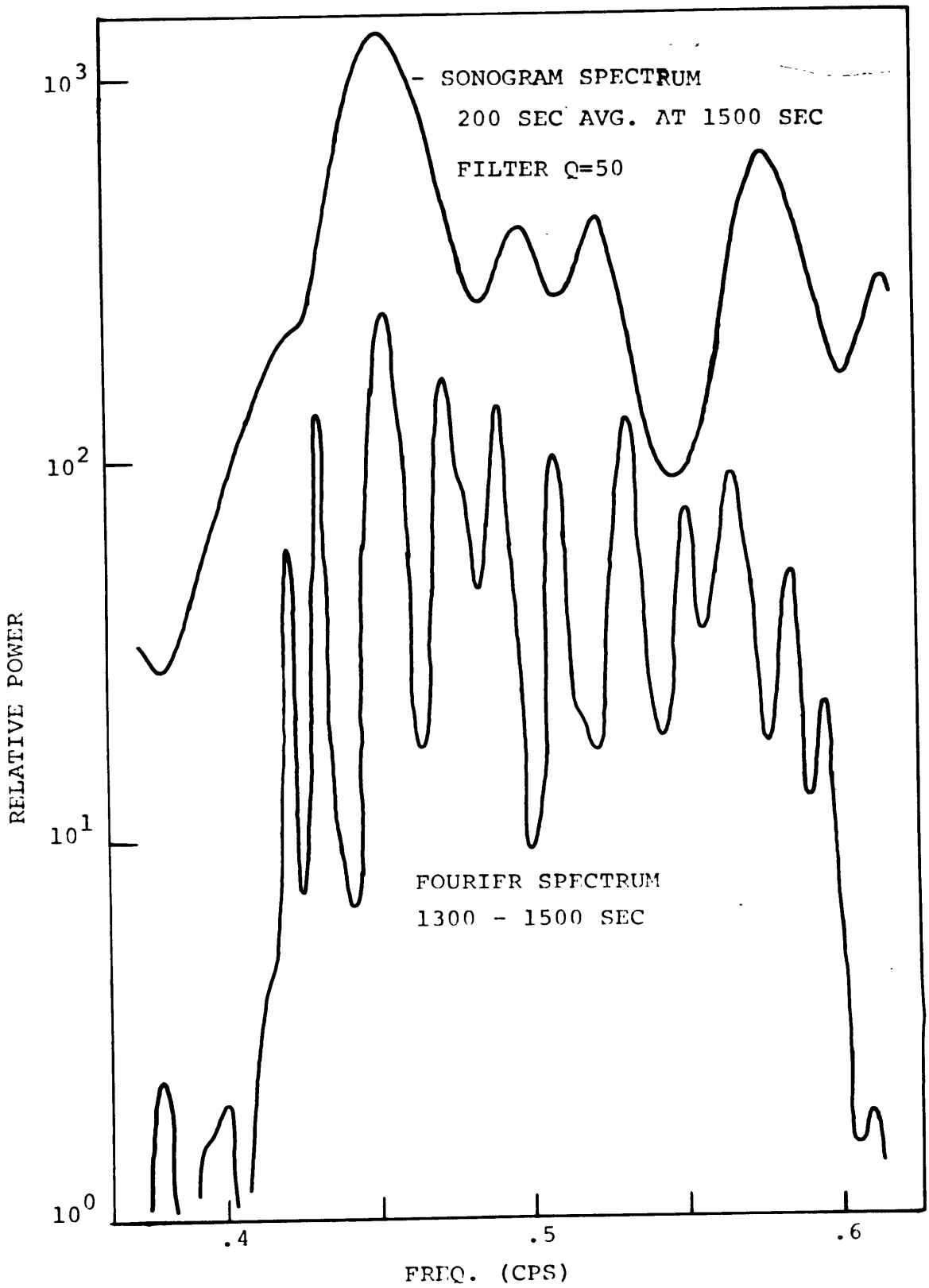

One way to obtain finer frequency resolution is to calculate the usual Fourier transform spectra for short data sections. When calculating the spectra by this technique it is important to keep the time sections shorter than one or two wave trains in order to avoid the other fine structure due to the repetative nature of the signals.

Figure 2.4.5 shows two spectra for the event of 4/29/66. The upper curve is a 200 sec averaged sonogram spectra at 0406 (1500 sec on the sonogram). The lower curve is a 200 second Fourier spectrum with much higher frequency resolution. Although the sonogram spectrum indicates some frequency structure we see that the lower resolution tends to merge many of the peaks. The smallest separations between the peaks is of the order of $2/T_o$, $3/T_o$ or $4/T_o$. The third feature of the fine structure is its Q, commonly being of the order of 30 to 50. In some cases the frequencies between the peaks may be down by as much as 20db. This fine structure is also present in the complicated events which show no recognizable series of wave trains and in the events which show no measurable dispersion.

A further discussion of the fine structure with respect to the resonant oscillations of the field lines will be taken up in the next chapter.

2.5 Densities in the Magnetosphere from Dispersion Measurements

The measured dispersion, calculated densities, L values and other pertinent data are given in Table 2.5.1. The listed emissions have been analyzed using the dispersion curves of section 1.6. The dispersion curves for the appropriate local time and L value were used and the magnetospheric boundary was assumed to be at 10 R_e.

The bandwidth of these events is typically of the order of .1 to .2 cps and the differences in group travel times (the dispersion for one round trip) between the low and high frequencies is around 10 to 20 sec. The slope of the individual wave trains indicates the cumulative dispersion experienced by the wave packet. Knowing the dispersion for one round trip allows one to determine the number of round trips the wave has made in the magnetosphere. Calculations of this type indicate that the first wave train of the dispersive series has made of the order of 5 to 20 round trips. This may be indicative of the number of passes a wave must make through the amplifying region before its amplitude is large enough to be observed relative to the other signals present at that time. In this respect it is interesting to consider the emission of 10/13/66 (Figure 1.1.1). This event, because of its slow increase in amplitude, did not trigger the recording system until 0506 although the initial increase above the background is noticeable 15 minutes earlier at 0451 (figure 2.3.3).

The cumulative dispersion for the first recorded wave train indicates that it had made 11 round trips. Since the travel time was 164 sec, the first wave train to rise above the background at 0451 had completed 5 round trips.

The ratio of the midfrequency to the equatorial gyrofrequency (the normalized frequency F) for the emissions in Table 2.5.1 falls in the range of .25 to .5, with the largest number of events falling in the range between .4 and .45.

The equatorial density vs. the L value for these events is shown in figure 2.5.1 along with two reference profiles which represent the results of whistler measurements for quiet and moderately disturbed periods (Angerami and Carpenter, 1966). The densities tend to be somewhat larger than those obtained from whistler data for Kp=2-4. They are however well below the expected values for very quiet conditions. This result indicates that hydromagnetic emissions propagate in the low density region outside of the plasmapause. The densities in figure 2.5.1 fall off at a rate between r-4 and r-5 which is in reasonable agreement with our density model (r-4).

Table 2.5.1

Dispersion measurements, equatorial densities and L values

Day	Time	f_l	f_h	T_l	T_h	f_+^e	T_o	L	n_e
	EST	cps		sec		cps	sec	R_e	cm^{-3}
4/24/66	0330	.439	.550	134	151	1.04	98	8.3	.84
5/17/66	0200	.632	.770	158	173	1.65	120	6.9	5.3
9/10/66	2030	.458	.725	130	136	3.52	118	5.3	39.
9/10/66	2200	.577	.822	133	152	1.83	105	6.7	4.8
9/12/66	0530	.500	.740	90	127	1.17	63	8.4	.29
10/4/66	0600	.800	.980	93	102	2.10	70	6.4	3.2
10/13/66	0500	.741	.949	164	193	1.76	116	7.1	3.9
1/20/67	0600	.980	1.20	140	154	2.65	104	6.0	12.
1/24/67	0515	.498	.596	163	175	1.37	121	7.8	1.9
6/13/67	0400	1.03	1.64	77	84	5.20	67	7.6	37.
6/22/67	0500	.411	.520	175	182	1.85	150	6.9	8.0
7/4/67	0345	.610	.900	103	117	2.20	86	6.2	5.4
7/4/67	0500	.828	1.07	113	123	2.75	90	5.9	10.4
6/9/60	1800	.640	.750	130	142	1.50	91	7.6	1.4

FIGURE 2.5.1
EQUATORIAL DENSITY
FROM DISPERSION MEASUREMENTS

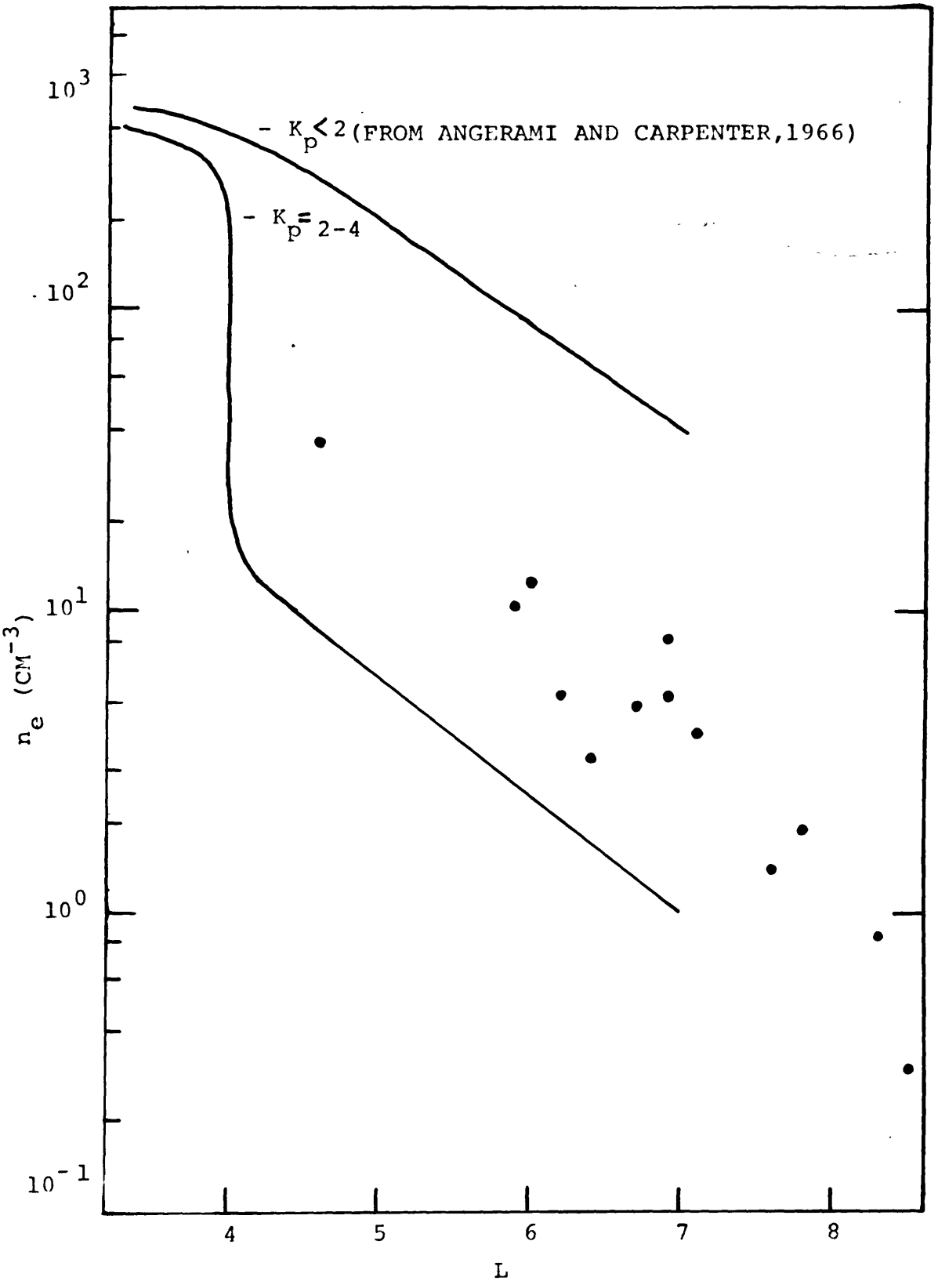

2.6 Discussion of Non-Dispersive Emissions

Of the thirty-four events recorded there are three examples in which well-defined rising wave trains exist but no dispersion is measurable. It has been suggested that these emissions with constant slope represent a case where a new wave is generated periodically near the equator and the slope is representative of the dispersion along the path from the equator to the surface. If all the frequencies are generated simultaneously at the equator the typical dispersion for frequencies near one-half the equatorial gyrofrequency is less than 10 seconds (Table 2.5.1). However, these events have a time delay between the low and high frequencies of the order of 100 seconds (figure 2.4.2).

There are several ways of accounting for this large time delay within a single wave train. One could assume that the wave frequencies are very close to the equatorial gyrofrequency ($F = .95$) but this is undesirable as the wave-particle interaction tends to damp waves of these frequencies (Liemohn, 1967). Another possible explanation is that the plasma instability could amplify different frequencies at different times and locations along the field line. If this is true then there is no a priori reason why any type of slope, rising or falling, should not be observed.

A simpler explanation would be to assume that the wave frequencies are well below the equatorial gyrofrequency so that the amount of dispersion over 5 or 6 round trips is smaller than can be measured. If this is the case, then the cumulative dispersion ($\lesssim$ 100 sec) as

shown by the slopes of the individual wave trains must be the result of many round trips.

We can test the above hypothesis by utilizing the empirical relation of section 2.4 which showed that for dispersive emissions the separations between the peaks in the spectra are of the order of $2/T_o$, $3/T_o$ and $4/T_o$.

In the following discussion we will assume that the frequencies are approximately .1 the equatorial gyrofrequency and using the results of section 1.6 determine the remaining parameters for these emissions. A comparison of the separation predicted by the calculated $1/T_o$ with the observed separations will show that the above assumption is reasonable.

The parameters for the non-dispersive emissions are given in Table 2.6.1 For the two emissions on 5/20/66 the normalized frequency was assumed to be .1 and for 5/29/66 it was assumed to be .15.

Table 2.6.1

Interpretation of the emissions of 5/20/66 (2124), 5/20/66 (2146) and 5/29/66 (0304) assuming the frequencies are much less than the equatorial ion gyrofrequency.

f_l	f_h	T(obs)	F	T_o	$1/T_o$	L	n_e	ΔT
5/20/66	(2124)							
.647	.821	97	.1	91.5	.011	4.2	134	2
5/20/66	(2146)							
.645	.820	88	.1	83	.012	4.2	110	1.6
5/29/66	(0304)							
.71	.94	103	.15	93	.0108	4.5	86	4

This interpretation leads to small L values and densities which are reasonable for these distances (figure 2.5.1). The time delay (ΔT) between the low and high frequencies for one round trip is small and in the first two cases 5/20/66) the dispersion over six wave trains would be so small as to be unmeasurable. In the last case, (5/29/66) the time delay over six wave trains (24 sec) would be just at the limit of the time resolution.

Two spectra for the emission of 5/20/66 (2.24) are given in figure 2.6.1 and a summary of the peaks for the three events is presented in Table 2.6.2.

Table 2.6.2

Peaks in the spectra of the emissions of 5/20/66 (2124), 5/20/66 (2146) and 5/29/66 (0304).

5/20/66 (2124)		5/20/66 (2146)		5/29/66 (0304)	
1002-1104 sec		815-917 sec		100-202 sec	
f	Δf	f	Δ f	f	Δ f
.650		.657		.745	
.685	.035	.677	.020	.781	.036
.708	.023	.703	.026	.820	.039
.740	.032	.725	.022	.840	.020
.775	.035	.745	.020	.883	.043
.805	.030	.780	.035	.908	.025
.835	.030	.840	.060	.928	.020
		.870	.030		

In these spectra we see peaks separated by the order of .02, .03, and .04 cps. Assuming that these represent separations by 2, 3 and 4 times $1/T_o$ the average separations corresponding to $1/T_o$ are, .011 cps (5/20/66, 2124), .0108 cps (5/20/66, 2146) and .0108 cps (5/29/66, 0304). In the first and last cases the agreement with the calculated separations in Table 2.6.1 are good. In the second case the calculated separation (.012 cps) is larger than the observed (.0108 cps) but it is probably within the limit of the errors in the calculations and the measurement of the observed separations.

The calculated time delay for one round trip when divided into the observed time delay (cumulative dispersion) should indicate the number of round trips made by the waves. The number of round trips for the emission of 5/20/66 (2124) is 76, for 5/20/66 (2146) it is 70 and for 5/29/66 (0304 it is 62.

We see then that the interpretation of non-dispersive emissions as events with frequencies well below the gyrofrequency is reasonable in terms of the L values, densities and observed separations between the peaks. Since the dispersion for one round trip is small and the observed time delay for one wave train is large the number of round trips made by the waves is large.

FIGURE 2.6.1

SPECTRA OF THE EMISSION OF 5/20/66

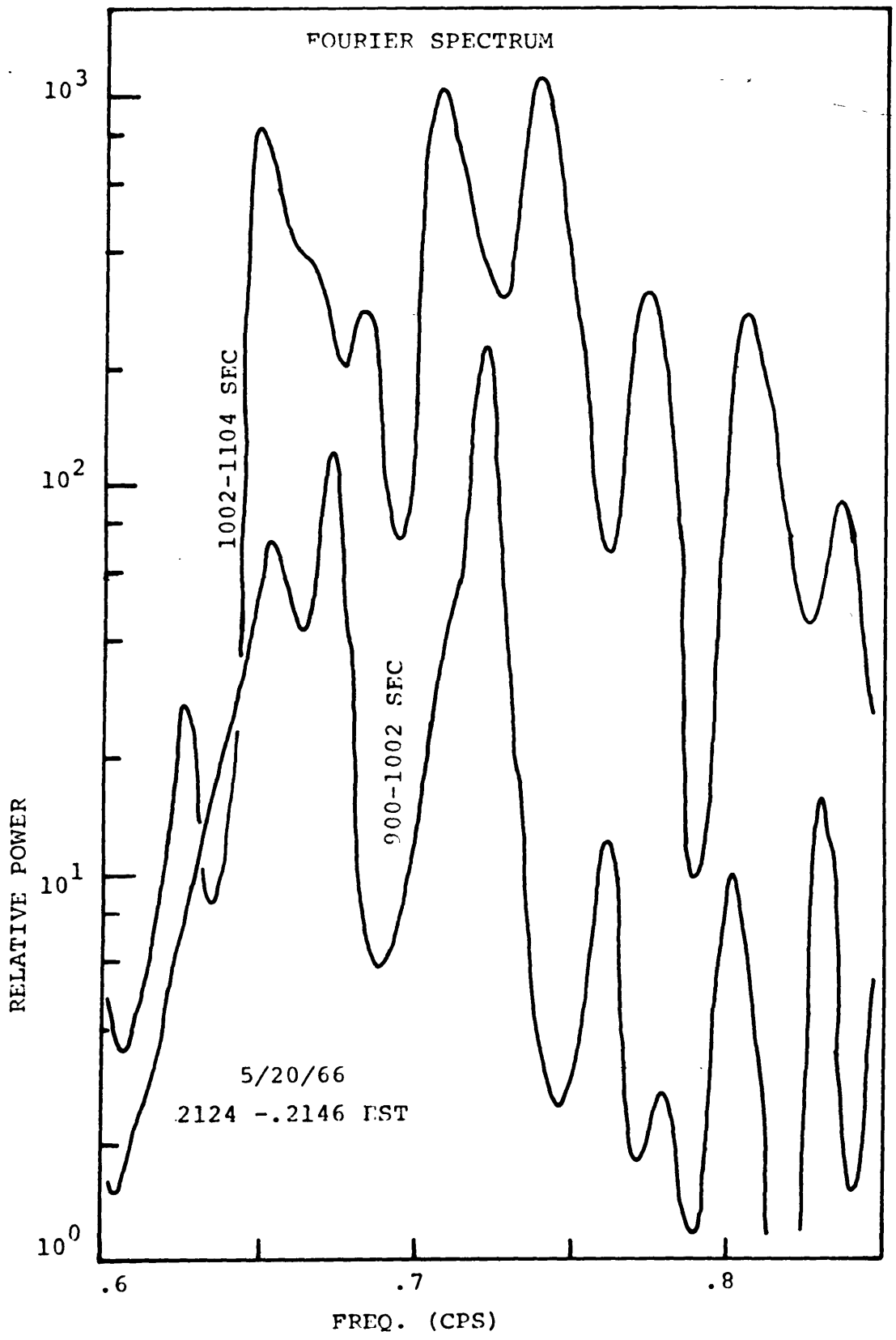

Chapter 3

RESONANT MODE STRUCTURE OF THE FIELD LINES

3.1 General

As was shown in section 2.4 the digital sonograms of hydromagnetic emissions exhibit a very pronounced frequency structure. The peaks in the spectra are approximately equally spaced and this spacing is related to the repetition period. The analysis of several dispersive events showed that the separation of the peaks was given approximately by the following equation.

$$\Delta f = (2, 3 \text{ or } 4) / T_o \qquad 3.1.1$$

where T_o is the travel time for a non-dispersive wave (F=0); recall that the phase and group velocities are equal at this limit.

One can consider the propagation of the anisotropic Alfven wave along the field lines as being analogous to the propagation of waves on a non-uniform string. When the "string" is terminated at two ends (the surface of the earth) and the proper boundary conditions applied we have a system with certain resonant modes of oscillation.

For a uniform string the travel time T_o is the period of the lowest mode of vibration. The frequencies of the higher modes are given by $fn=n/T_o$. We note with reference to 3.1.1 that the frequency separation between modes will

$1/T_o$. It is apparent then that the peaks observed in the spectra are a reflection of the resonant modes of vibration of the field lines.

In the case of a non-uniform string we can determine the frequencies of the resonant modes by use of the WKB method which requires that the phase integral over the length be equal to an integral number of half wavelengths (equation 3.1.2).

$$n\pi = \omega \int_0^L \frac{ds}{v(s,f)} \qquad 3.1.2$$

This technique is valid if the change in velocity over a wavelength is small; a condition which is not satisfied below an altitude of 15,000 km for frequencies of the order of 1cps. The phase velocity, like the group velocity, decreases with increasing frequency. In the magnetosphere along the field lines the velocity is a minimum at the equator and reaches a maximum at an altitude of 2000 km.

This low velocity region contributes most to the integral in 3.1.2 so that the frequencies of the resonant modes are determined mainly by the properties in the equatorial region. Also we can see from 3.1.2 that as the frequency increases (the velocity decreases) the modes will become closer together in frequency.

As a rough approximation the WKB method is suitable for providing a basic understanding of the characteristics of the resonant behavior. In order to treat adequately

the various field line and density models the propagation of the waves was formulated as a one dimensional, layered media problem.

3.2 Formulation of the One Dimensional Problem

In this section we will derive a matrix equation which determines the fields at any point in a constant velocity region, given the values of the fields at some other point. Repeated application of this equation for each layer of constant velocity coupled with the appropriate boundary conditions will permit a complete solution of the problem. Let us consider first the propagation of waves in a homogeneous plasme. The components of the wave are:

$$\vec{E} = (E_x \hat{x} + E_y \hat{y} + E_z \hat{z}) e^{j(\omega t - \alpha x)}$$

$$\vec{B} = (B_x \hat{x} + B_y \hat{y} + B_z \hat{z}) e^{j(\omega t - \alpha x)} \qquad 3.2.1$$

where the geometry is given in figure 3.2.1

Figure 3.2.1

Geometry for wave propagating at an angle to the field.

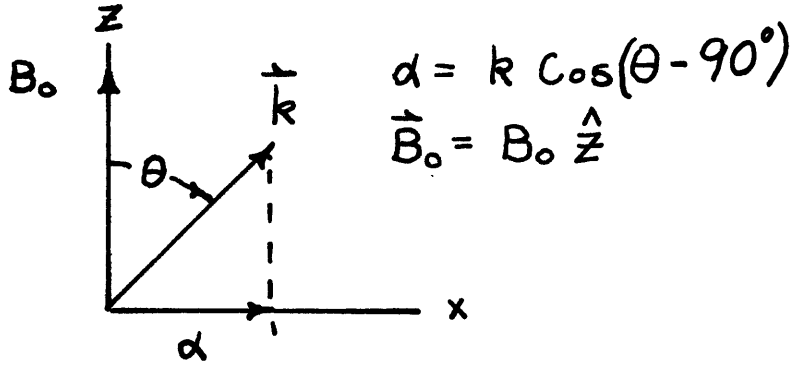

Maxwell's equations for a wave propagating in a plasma are given in 3.2.2.

$$\nabla \times \vec{E} = -j\omega B$$

$$\nabla \times \vec{B} = j\omega \epsilon_0 \mu \, \overline{\overline{K}} \cdot \vec{E} \qquad 3.2.2$$

where

$$\overline{\overline{K}} = \begin{bmatrix} KT & -KX & 0 \\ KX & KT & 0 \\ 0 & 0 & KP \end{bmatrix} \qquad 3.2.3$$

and from Appendix A

$$KT = \frac{c^2}{V_a^2} \frac{(1 - F_+ F_-)}{(1 - F_+^2)(1 - F_-^2)}$$

$$KX = j \frac{c^2}{V_a^2} \frac{(F_+ - F_-)}{(1 - F_+^2)(1 - F_-^2)} \qquad 3.2.4$$

$$KP = -\frac{c^2}{V_a^2} \frac{1}{F_+ F_-}$$

$F_\pm = \omega / \Omega_\pm$ = ratio of wave frequency to gyrofrequency.

In component form equations 3.2.2 become:

$$\frac{d E_y}{dz} = j\omega B_x \qquad 3.2.5$$

$$\frac{d E_x}{dz} = -j\alpha E_z - j\omega B_y \qquad 3.2.6$$

$$j\alpha E_y = j\omega B_z \qquad 3.2.7$$

$$-\frac{d B_y}{dz} = j\omega\mu\epsilon_0 (KT E_x - KX E_y) \qquad 3.2.8$$

$$\frac{d B_x}{dz} = j\omega\mu\epsilon_0 (KX E_x + KT E_y) - j\alpha B_z \qquad 3.2.9$$

$$-j\alpha B_y = j\omega\mu\epsilon_0 KP E_z \qquad 3.2.10$$

Making the substitutions of 3.2.10 into 3.2.6 and 3.2.7 into 3.2.9 we have in matrix form

$$\frac{d}{dz}\begin{bmatrix} E_x \\ E_y \\ B_x \\ B_y \end{bmatrix} = j\omega \begin{bmatrix} 0 & 0 & 0 & -\left(1-\frac{\alpha^2}{\omega^2\mu\epsilon KP}\right) \\ 0 & 0 & 1 & 0 \\ \mu\epsilon KX & \mu\epsilon KT\left(1-\frac{\alpha^2}{\omega^2\mu\epsilon KT}\right) & 0 & 0 \\ -\mu\epsilon KT & \mu\epsilon KX & 0 & 0 \end{bmatrix} \begin{bmatrix} E_x \\ E_y \\ B_x \\ B_y \end{bmatrix} \qquad 3.2.11$$

For phase propagation parallel to the field ($\alpha = 0$) the above set of equations can be simplified into a 2 x 2 matrix form by the proper combination of the field vectors. For a left rotating coordinate system we make the combinations $E_L = E_x - jE_y$ and $B_L = j(B_x - jB_y)$. With this substitution 3.2.11 becomes.

$$\frac{d}{dz}\begin{bmatrix} E_L \\ B_L \end{bmatrix} = \begin{bmatrix} 0 & -j\omega \\ -j\omega/V_L^2 & 0 \end{bmatrix} \cdot \begin{bmatrix} E_L \\ B_L \end{bmatrix} \qquad 3.2.12$$

where $V_L^2 = V_A^2(1-F_+) = C^2/KL = 2C^2/(KT - jKX)$

This form of our original set of equations is satisfactory so long as the two terms containing α^2 in 3.2.11 are much less than 1. This condition is easily satisfied in the 1,4 term of the matrix in 3.2.11 as KP is quite large (note the F- in the denominator in equation 3.2.4). In the case of the 3,2 term this condition is not so easily met as KT is of the order of 10^{-3}KP. In this case one is justified in dropping the α^2 factor only when $\theta < 40^\circ$.

Unless there is a certain amount of refraction by density gradients transverse to the magnetospheric field, θ will exceed this angle at latitudes along the field line greater than 20° (Appendix B.) This angular distance ($\lambda = 20^\circ$) accounts for almost 50 percent of the total arc length of the field line and at these latitudes the

wave frequency will be well below the gyrofrequency. This last result allows us to investigate some of the propagation characteristics in a simple fashion as the set of equations in 3.2.11 uncouple. As $F_+ \to 0$, ($KX \ll KT$ 3.2.4) equation 3.2.11 can be separated into two sets of equations, one for Bx, Ey (extra-ordinary) and another for By, Ex (ordinary). The limit $KX \to 0$ is equivalent to the Quasi-Plane (Quasi-Transverse) and the MHD approximations. As the name Quasi-Plane implies the ordinary (guided or anisotropic) wave and the extra-ordinary (unguided or isotropic), wave have plane polarizations.

In the limit where the terms in α^2 are small the two linerarly polarized waves have the same propagation characteristics. These waves can be added at one point with the proper phase lag to produce a left polarized wave and after propagating through an inhomogeneous region they will still add together to give the same polarization since each has the same velocity and reflection coefficients.

For α not equal to zero the two waves will have different propagation characteristics; the first set above being more dependent on α. A detailed examination of the effects of non-zero α on the propagation of these waves is worthy of further study.

The equation 3.2.12 is of the form

$$\frac{dX}{dz} = A \cdot X \qquad 3.2.13$$

If the matrix A is constant (v constant) between Z_1 and Z_2 we can easily integrate 3.2.9.

$$X_1 = X_2 e^{A(z_1 - z_2)} \qquad 3.2.14$$

The exponential in 3.2.14 can be expanded in a power series as follows:

$$e^{A(z_1-z_2)} = I + A(z_1-z_2) + \frac{A^2(z_1-z_2)^2}{2!} + \frac{A^3(z_1-z_2)^3}{3!} + \cdots \qquad 3.2.15$$

The characteristic equation for the matrix $A(Z_1 - Z_2)$ is

$$\lambda^2 = -\omega^2(z_1-z_2)^2 / N^2 \qquad 3.2.16$$

and the Cayley-Hamilton theorem states that the matrix satisfies its own characteristic equation.

$$A^2(z_1-z_2)^2 = \lambda^2 I \qquad 3.2.17$$

Regrouping the terms in 3.2.15 and making use of 3.2.17 we find that

$$e^{A(z_1-z_2)} = I\left(1 + \lambda^2/2! + \lambda^4/4! + \cdots\right) + \frac{A(z_1-z_2)}{\lambda}\left(\lambda + \lambda^3/3! + \lambda^5/5! + \cdots\right) \qquad 3.2.18$$

$$e^{A(z_1-z_2)} = I\,\mathrm{Cos}(j\lambda) + \frac{A(z_1-z_2)}{j\lambda}\,\mathrm{Sin}(j\lambda) \qquad 3.2.19$$

and upon substitution of 3.2.16 in 3.2.17 we obtain the final result.

$$e^{A(z_1-z_2)} = \bigsqcap_{1\,2} = \begin{bmatrix} \mathrm{Cos}\,\gamma_{12} & jN_1\,\mathrm{Sin}\,\gamma_{12} \\ \frac{j}{N_1}\mathrm{Sin}\,\gamma_{12} & \mathrm{Cos}\,\gamma_{12} \end{bmatrix} \qquad 3.2.20$$

where $\gamma_{12} = \frac{\omega}{N_1}(z_2 - z_1)$

The solution of 3.2.12 for a layer of constant velocity is then

$$\begin{bmatrix} E_m \\ B_m \end{bmatrix} \quad \bigsqcap_{m\ m+1} \quad \begin{bmatrix} E_{m+1} \\ B_{m+1} \end{bmatrix} \qquad 3.2.21$$

The matrix in 3.2.21 relates the fields at Zm to the fields at Zm+1 through a region ($Z_m \leq Z \leq Z_{m+1}$) in which the velocity is constant. In the model to be used in this section the arc distance along the field line is the linear distance Z and the layers of constant velocity are taken perpendicular to the field lines. In this treatment we have neglected the effects due to the curvature of the field lines. The model is shown in figure 3.2.2.

Figure 3.2.2

One Dimensional Model

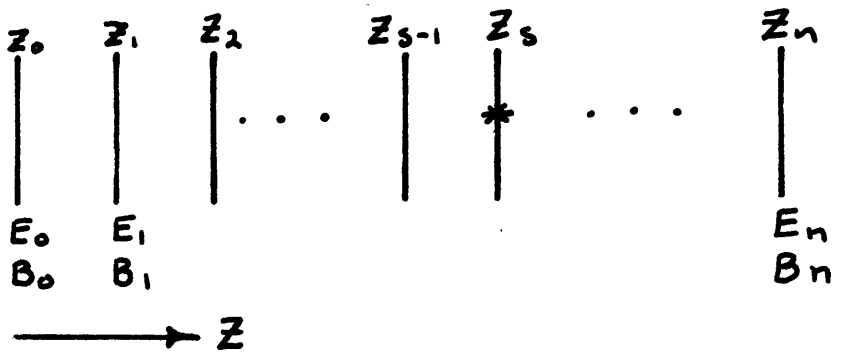

Application of 3.2.21 at each of the boundaries results in the following equation relating the fields at each end of the system.

$$\begin{bmatrix} E_0 \\ B_0 \end{bmatrix} = \Omega_0 \Omega_1 \Omega_2 \cdots \Omega_{S-1} \Omega_S \left\{ [S] + \Omega_S \Omega_{S+1} \cdots \Omega_{n-1} \Omega_n \begin{bmatrix} E_n \\ B_n \end{bmatrix} \right\} \qquad 3.2.22$$

$$\begin{bmatrix} E_0 \\ B_0 \end{bmatrix} = M [S] + N \begin{bmatrix} E_n \\ B_n \end{bmatrix} \qquad 3.2.23$$

where S is the source vector (Se, Sb).

Two models were set up and solved using 3.2.23. The first, which will be called the open model, has a layered region from Z_o to Z_s and a uniform halfspace for Z greater than Z_s. This model will be used to represent the field line from the equator (Z_s) to the surface (Z_o). In this model the boundary conditions are that at $Z = Z_o$ the electric field vanish and that at $Z = Z_s$ there be an outgoing wave only.

$$Z = 0 \; ; \; E_o = 0$$

$$Z = Z_s \; ; \; B_s = E_s / N_s \qquad 3.2.24$$

The boundary conditions (3.2.24) and equation 3.2.23 lead to two equations in two unknowns (E_s and B_o). With the source in the magnetic field the solution of 3.2.23 and 3.2.24 is:

$$E_s = \frac{-M_{12} S_b}{(M_{11} + M_{12}/N_s)}$$

$$B_o = \left[M_{22} + M_{12} \frac{(M_{21} + M_{22}/N_s)}{(M_{11} + M_{12}/N_s)} \right] S_b \qquad 3.2.25$$

The second or closed model represents the complete field line. The points at Z_o and Z_n correspond to the inter-

section of the field line with the surface of the earth and the source position (Z_s) corresponds to the equatorial crossing point of the field line.

The boundary conditions for this model are that the electric fields vanish at the ends ($E_o = 0$, $E_n = 0$). The boundary conditions and equation 3.2.23 yield two equations in two unknowns (B_o, B_n) which are solved for sources in either the electric or magnetic fields.

source in the electric field $S = (S_e, 0)$

$$B_n = -\frac{M_{11}}{N_{12}} S_e$$

$$B_o = \left(\frac{M_{21} N_{12} - M_{11} N_{22}}{N_{12}}\right) S_e \qquad 3.2.26$$

source in the magnetic field

$$B_n = -\frac{M_{12}}{N_{12}} S_b$$

$$B_o = \left(\frac{N_{12} M_{22} - M_{12} N_{22}}{N_{12}}\right) S_b \qquad 3.2.27$$

Since the matrices M and N are complex, the fields will in general be complex, i.e. $B = |B| e^{j\phi}$.

The values of the fields at any intermediate point can be determined from the end velues if the partial matrix products in 3.2.22 are saved.

$$\begin{bmatrix} E_m \\ B_m \end{bmatrix} = \prod_{m}^{m+1} \cdots \prod_{s-1}^{s} \left\{ [S] + \prod_{s}^{s+1} \cdots \prod_{n-1}^{n} \begin{bmatrix} 0 \\ B_n \end{bmatrix} \right\} \quad 3.2.28$$

The operations in equation 3.2.22 through 3.2.28 were programmed for machine computation and the results will be presented in section 3.4.

We can consider the model we have set up as a one-dimensional box in which we have placed a source. The solution we have obtained allows us to determine the response of the box as the source changes frequency. In the open model the source and the reflected energy are allowed to radiate into a half space while in the closed box the energy is trapped between two perfect conductors. We have yet to specify the velocity structure within the layered box and this problem will be taken up in the next section.

3.3 Models for the One Dimensional Box

The Alfven velocity along the field line is a function of the magnetic field strength and the density. Equation 1.4.3 provides the magnitude of the field as a function of the magnetic latitude. The linear distance along the field line as a function of magnetic latitude is found by integrating equation 1.4.1.

$$Z = S(\lambda) - S(\lambda_o) \qquad 3.3.1$$

where

$$S(\lambda) = \frac{R_e L}{2}\left[\sin\lambda\sqrt{1+3\sin^2\lambda} + \frac{1}{\sqrt{3}}\ln\left\{\sqrt{3}\sin\lambda + \sqrt{1+3\sin^2\lambda}\right\}\right] \qquad 3.3.2$$

The layered model representing the field line was considered symetric about its midpoint, corresponding to the equator and each half was in addition separated into two regions. The section from the center to a distance of 1000 km from the end was considered as representing the magnetosphere. The density varies through most of this region as r^{-4} except from 4000 to 1000 km where it was joined smoothly to the density in the ionospheric part of the model. The velocity in the magnetospheric

part of the model is given by 3.3.3.

$$\mathcal{V} = V_a \left(1 - \omega / \Omega_+\right)^{1/2} \qquad 3.3.3$$

where $V_a = B / [4\pi n m_+]^{1/2}$

$\Omega_+ = |e| B / m_+$

The velocity in this part of the model is real and dispersive.

In the remainder of the model the region from 1000 to 100 km represents the ionosphere and an air layer from 100 to 0 km completes this section. The basic ionospheric model is representative of night time, solar minimum conditions, with one variation of this model permitting higher collision frequencies which are representative of the average conditions between solar maximum and minimum. The velocity in this section of the model was calculated from 3.3.4.

$$\mathcal{V} = V_a \left[\frac{\left\{1 - \frac{\omega}{\Omega_+}\left(1 - j\frac{\nu_+}{\omega}\right)\right\}\left(1 - j\frac{\nu_-}{\omega}\right)}{1 - j\left(\frac{\nu_+}{\omega} + \frac{m_-}{m_+}\frac{\nu_-}{\omega}\right)} \right]^{1/2} \qquad 3.3.4$$

where ν_+ = ion collision frequency

ν_- = electron collision frequency

The collision terms in 3.3.4.result in a complex, dispersive velocity. The losses of energy in the system are allowed in the two regions representing the ionosphere at the ends of the box.

The parameters used in the various models are presented in Appendix D along with representative velocity profiles.

3.4 Results from the One Dimensional Models

We will discuss first the results of the open models the ionosphere alone and for the combination of the ionospheric and magnetospheric models. The latter will show the filtering effects on the spectrum for waves generated at the equator and propagated to the surface.

Next the closed model results will be presented. These will show that terminating the field lines introduces a spectrum of resonant modes of high Q. The waves which exist for long times in the magnetosphere will acquire a spectrum of this type. The resonant modes from low to high frequencies will be investigated even though the frequencies of hydromagnetic emission correspond to very high order modes (20 to 50). The low order mode information will be needed in order to relate the results of the model calculations to the observed fine structure.

The models used in the calculations are given in Appendix D. Three ionospheric models have been used. The first model (I-1) has 13 layers and is representative of night-solar minimum conditions. The second ionospheric model has the same density profile as the I-1 but higher collision frequencies representative of the average between solar minimum and solar maximum. The last ionospheric model (I-3) has a density profile appropriate for early morning (0600). The densities in the magnetospheric models are proportional to r^{-4} except at the lowest altitudes (1000 to 400 km). These models are specified by their L value and the equatorial density (n_e).

FIGURE 3.4.1

OPEN MODELS

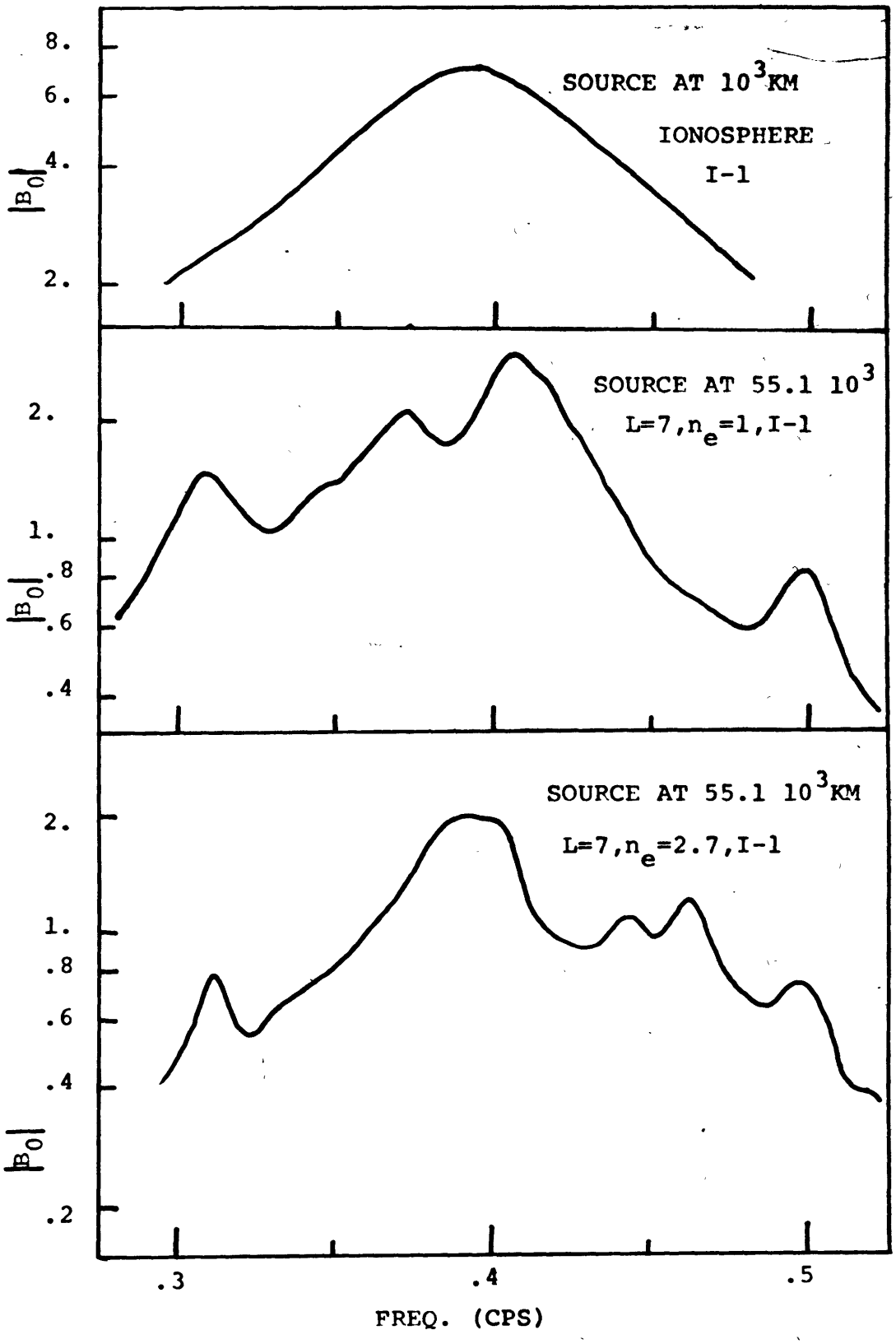

The top curve in figure 3.4.1 shows the response of the ionospheric model I-1 to a source at 1000 km and a half space above. Here we see a broad peak at .39 cps with a Q of 6. At this frequency there is a resonance in the low velocity part of the ionosphere such that there is a standing oscillation of one quarter wavelength between the surface and a height of about 1000 km. There will be a series of resonances of this type at approximately odd multiples of this frequency (1.17, 1.56 etc.) representing standing oscillations of odd multiples of a quarter wave.

This resonance is important for several reasons since it not only provides the transparent windows through which energy can propagate into the ionosphere, but it also controlls the cutoff frequency of waves propagating in the ionospheric waveguide. It is the ducting of the wave energy in this waveguide which permits one to observe hydromagnetic emissions entering the ionosphere at latitudes greater than that of the observation point.

The second and third curves in figure 3.4.1 illustrate the amplitude response at the surface for the open models when a source is located at the equatorial crossing point of the field lines. In these spectra we see a broad bandpass region centered on the frequency of the ionospheric resonance and several subsidiary peaks which are the result of the filtering action of the magnetosphere. The Q's of these peaks are of the order of 10 to 15. Calculations performed with the same magnetospheric

FIGURE 3.4.2

OPEN MODELS I-3, L=7, n_e=1

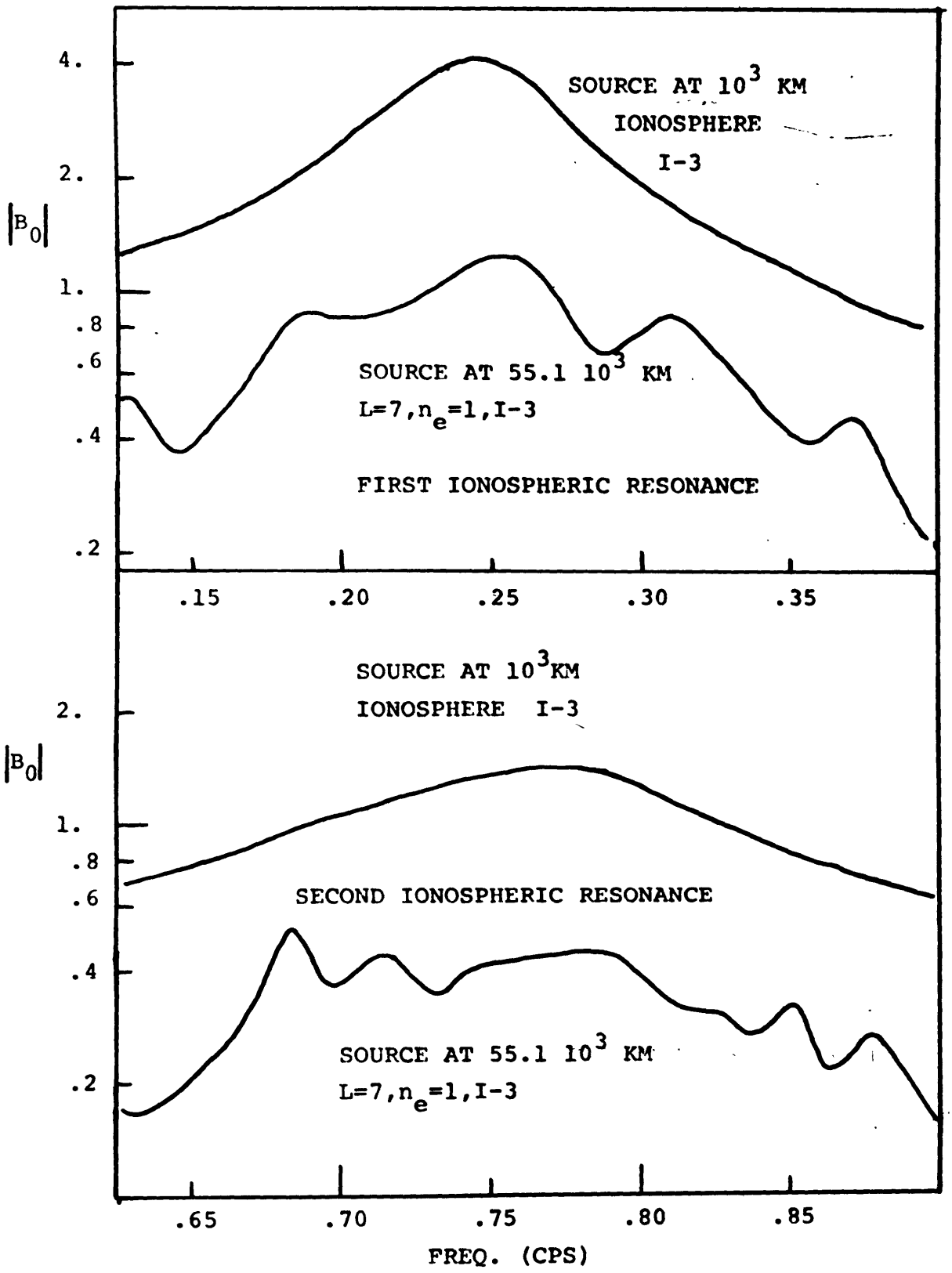

model and an increased collison frequency (model I-2) show a slight lowering of the amplitudes and the Q's.

Figure 3.4.2 shows the amplitude spectra for the one quarter and three quarter wavelength resonances (curves 1 and 3) of the early morning ionospheric model (I-3). Since the velocities in this model are lower than the preceeding example, the resonances are at lower frequencies. The first resonance is at .25 cps and has a Q of 3.8 and the second has a frequency a little greater than three times the first (.775 cps) and has a Q of 3.5.

The second and fourth curves (figure 3.4.2) are the amplitude spectra for the early morning ionosphere and the L = 7, n_e = 1 magnetosphere model with the source at the equator. As in the previous model these spectra have a broad bandpass at the ionospheric resonance and a number of superimposed peaks. In the region near the first ionospheric resonance these peaks have Q's in the range 3 to 7 and at the higher resonance, 16 to 25. Note that the higher Q peaks tend to be those on the flanks of the central bandpass.

As a final example of the open models, the amplitude spectra for a high density magnetosphere (L = 7 n_e = 2.7) and the early morning ionosphere are presented in figure 3.4.3. The upper and lower curves are for frequencies near the first and second ionospheric resonances respectively. The Q's of the peaks in this case are a bit greater than in the L = 7, n_e =1 model being of the order of 4 to 12 for the first resonance group and 20 to 40

FIGURE 3.4.3
OPEN MODELS I-3,L=7,n_e=2.7

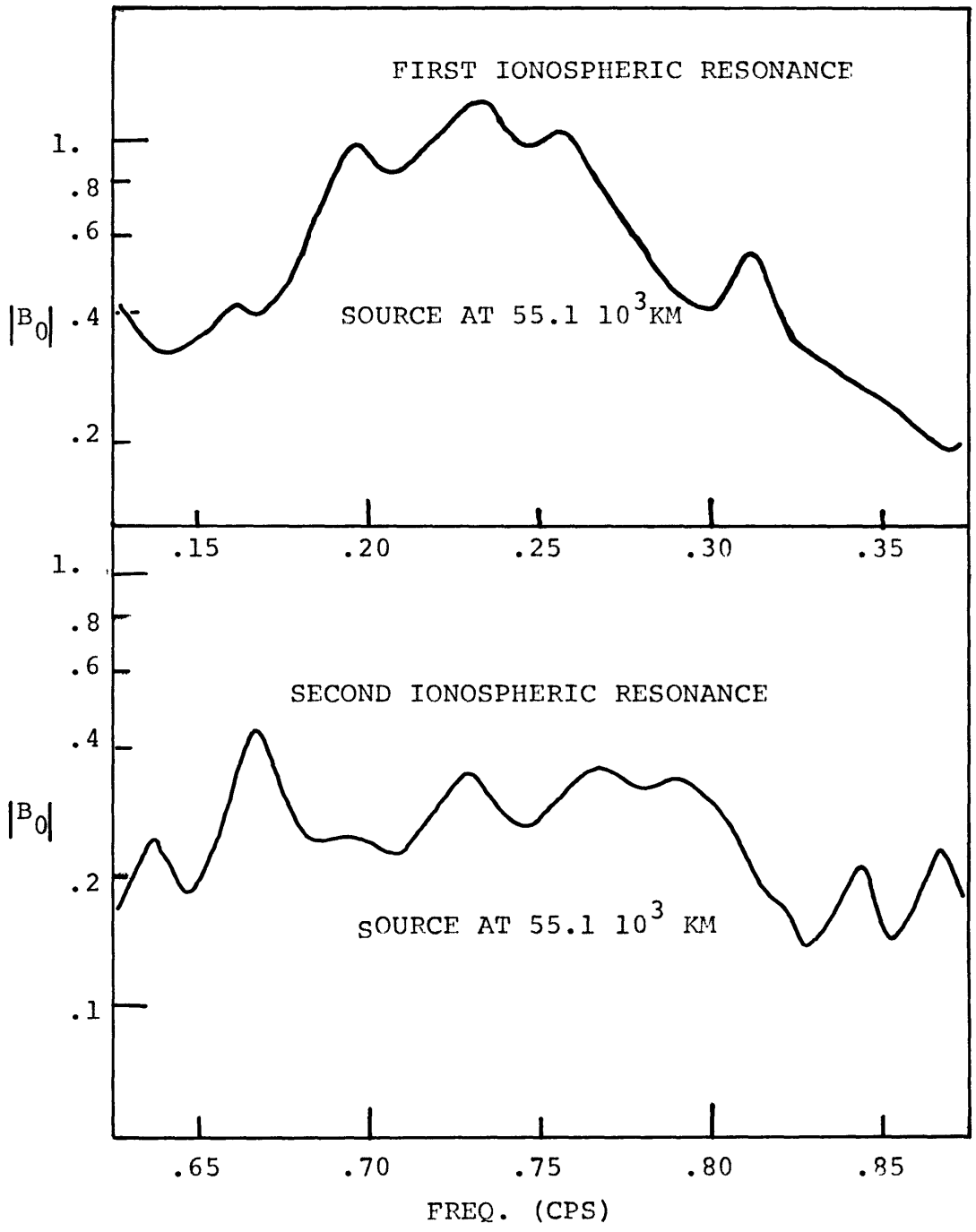

for the second. Note also that the peaks are spaced closer together in this model due to the lower velocities in the magnetospheric part of the model. Although these spectra bear a superficial resemblance to the observed spectra of some hydromagnetic emissions we have seen in section 2.4, the peaks are not spaced nearly so regularly nor do they have Q's as large as those which are often observed.

We will now consider the results of the closed model calculations. These models represent the complete field line from the surface of the earth in the northern hemisphere to the surface in the southern hemisphere. The models are symmetric about the equatorial crossing point at which point a source of unit amplitude and zero phase is located. Since the model is symmetric with respect to the source, we find that a source in the electric field excites only the even modes (an even number of quarter wavelengths) and a source in B excites only the odd modes.

These models are very different from the open models in that the waves are confined between two perfectly conducting surfaces and are, therefore, capable of building up strong resonances as can be seen in figure 3.4.4.

This figure shows the response of the system in the neighborhood of the seven lowest modes for the magnetospheric model L = 7, $n_e = 1/cm^3$ and the night time ionospheric model I-1. The velocity structure for this model is shown in figure 3.4.5.

The Q's of these peaks are quite high, typically greater than a few hundred. The frequencies of these peaks and the resonant frequencies one would calculate from the travel time integral for this velocity model are presented in Table 3.4.1.

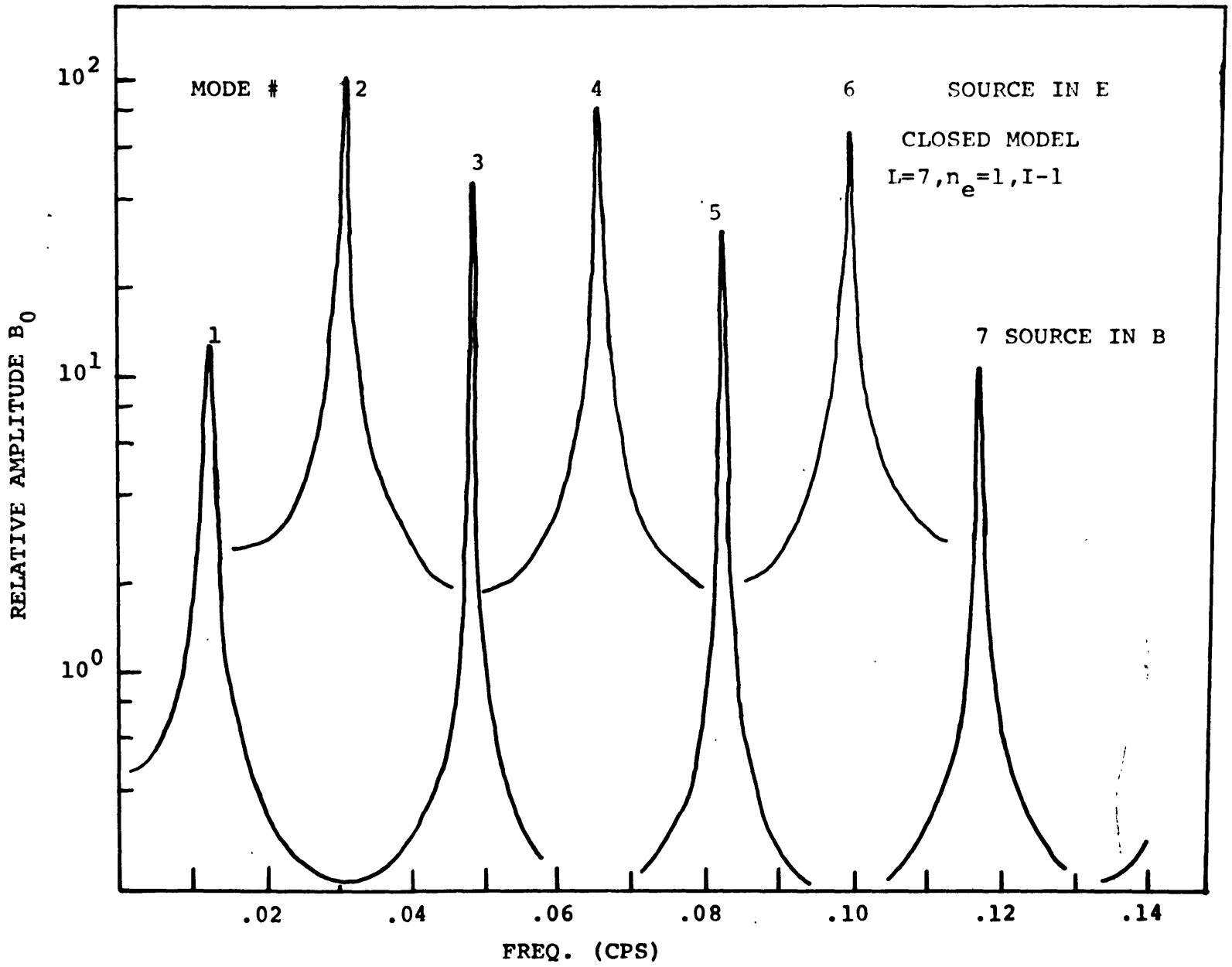

FIGURE 3.4.4
AMPLITUDE VS FREQUENCY, LOW MODES
I-1, L=7, n_e=1

FIGURE 3.4.5
VELOCITY MODEL
L=7, n_e=1, I-1

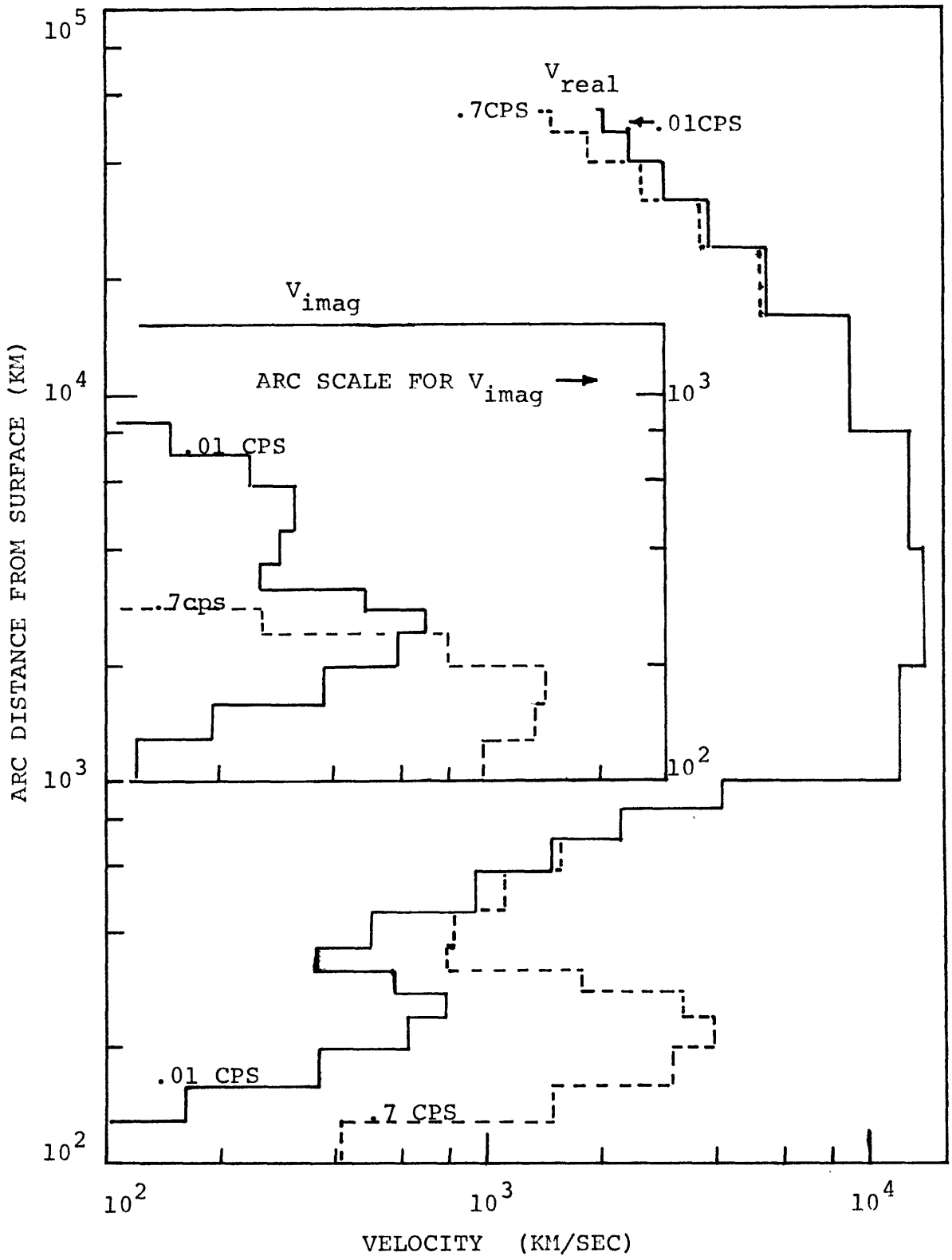

Table 3.4.1

Resonant frequencies from one dimensional model and from phase travel time (WKB).

$L = 7$, $n_e = 1$, I-1

Mode	Model	Phase travel time
1	.0118 cps	.0155 cps
2	.0308 cps	.0309 cps
3	.0480 cps	.0464 cps
4	.0653 cps	.0619 cps
5	.0821 cps	.0774 cps
6	.0990 cps	.0928 cps
7	.1165 cps	.1083 cps

The frequency of the first mode computed from the inverse of the phase travel time ($T_o = 64.6$ sec) is too high by 30 percent; the frequency of the second mode is about correct and the frequencies of the next few modes are about 7% too low.

Figure 2.4.6 shows the low order mode structure as a function of arc distance from the surface to the equator. The odd modes (source in B) are antisymmetric about the equator and even modes (source in E) are symmetric. The increase in wave length (zero crossing) due to the increase in velocity towards the surface can be seen in the case of the seventh mode. At still higher frequencies the mode structure (zero crossings) tends to be concentrated

FIGURE 3.4.6
LOW ORDER MODE STRUCTURE

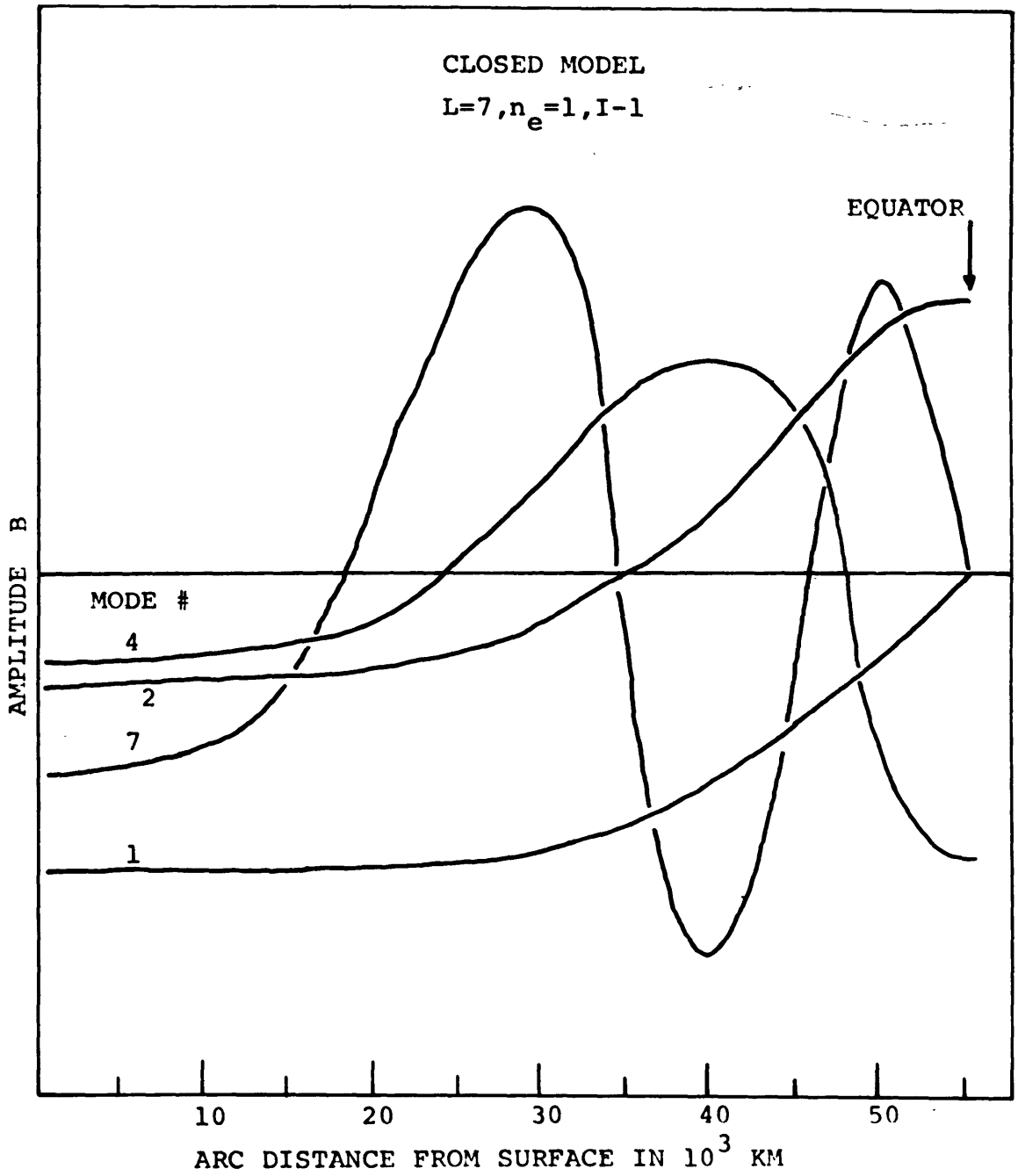

in the low velocity (short wavelength) region near the equator.

The other low velocity region in the ionosphere below 1000 km (figure 3.4.5) has a fundamental resonance ($\lambda/4$) near .4 cps as we have seen previously. The effects of this resonance in the closed model are illustrated in figure 3.4.7. The top curve in this figure shows the amplitude of B at the equator for a source in E, the bottom curves show the amplitude of B at the surface for sources in E and B. These curves show the effects of this resonance in the complete model consisting of the magnetosphere and the ionosphere; recall that the only disipative part of the model is the ionosphere. As the modes approach the frequency of the ionospheric resonance the amplitudes and Q's of the peaks decrease. The Q's of the peaks between .40 and .42 cps are about 50 and the Q's off to the sides of this region are of the order of 100. At still higher frequencies the Q's can be as large as 500 to 1000. Note that the response at the equator (top curve) is similar to that seen at the surface except that the minima between the peaks are deeper in the former case.

The mode structure near the end of the model, for several peaks in the vicinity of the ionospheric resonance, are given in figure 3.4.8. As the frequency increases the mode (zero crossing) moves down until at .406 cps we have a quarter wave between a distance of 750 km and the surface.

We find then that the collisional effects (dissipation)

FIGURE 3.4.7

AMPLITUDE VS FREQUENCY

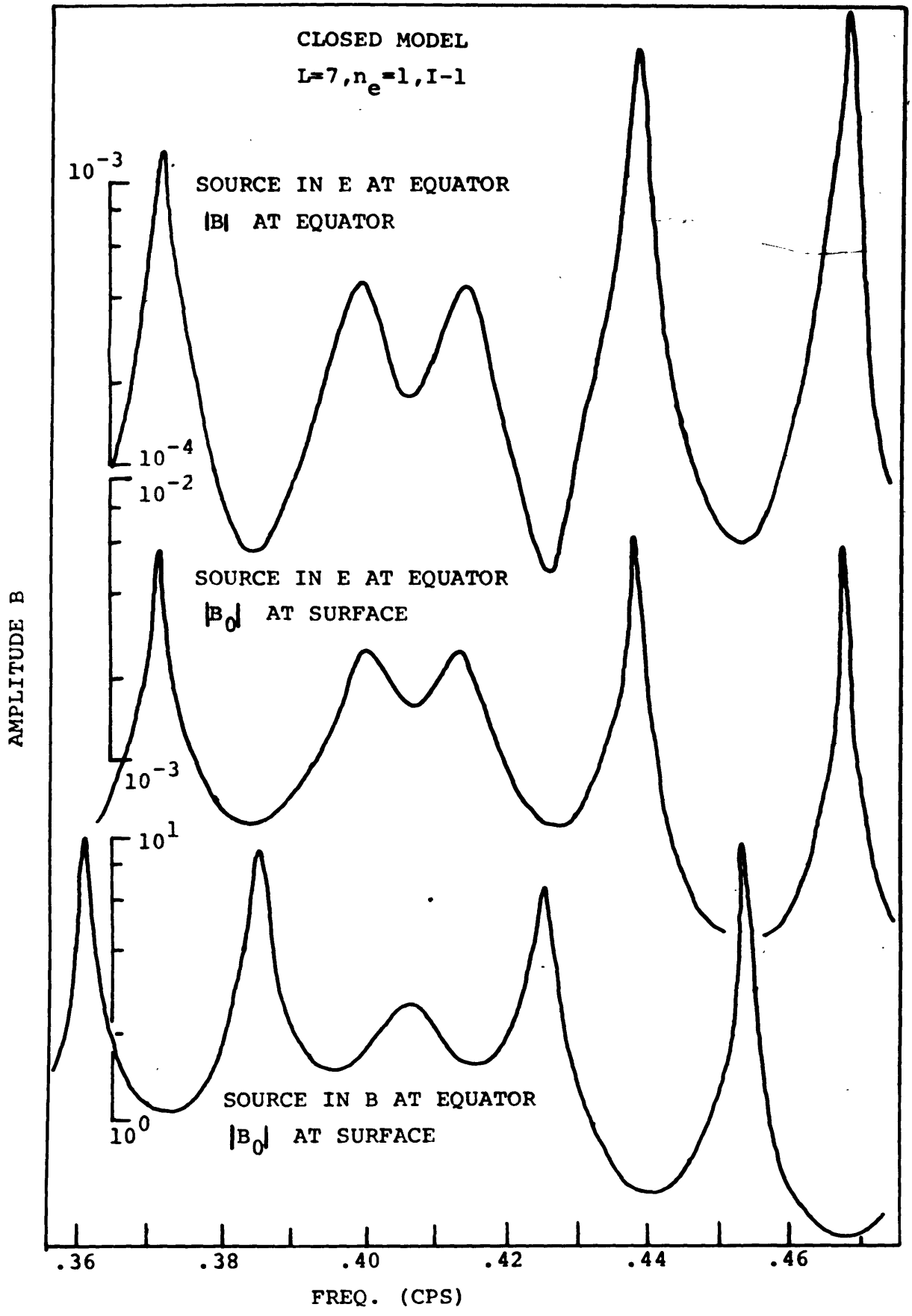

FIGURE 3.4.8
AMPLITUDE VS HEIGHT

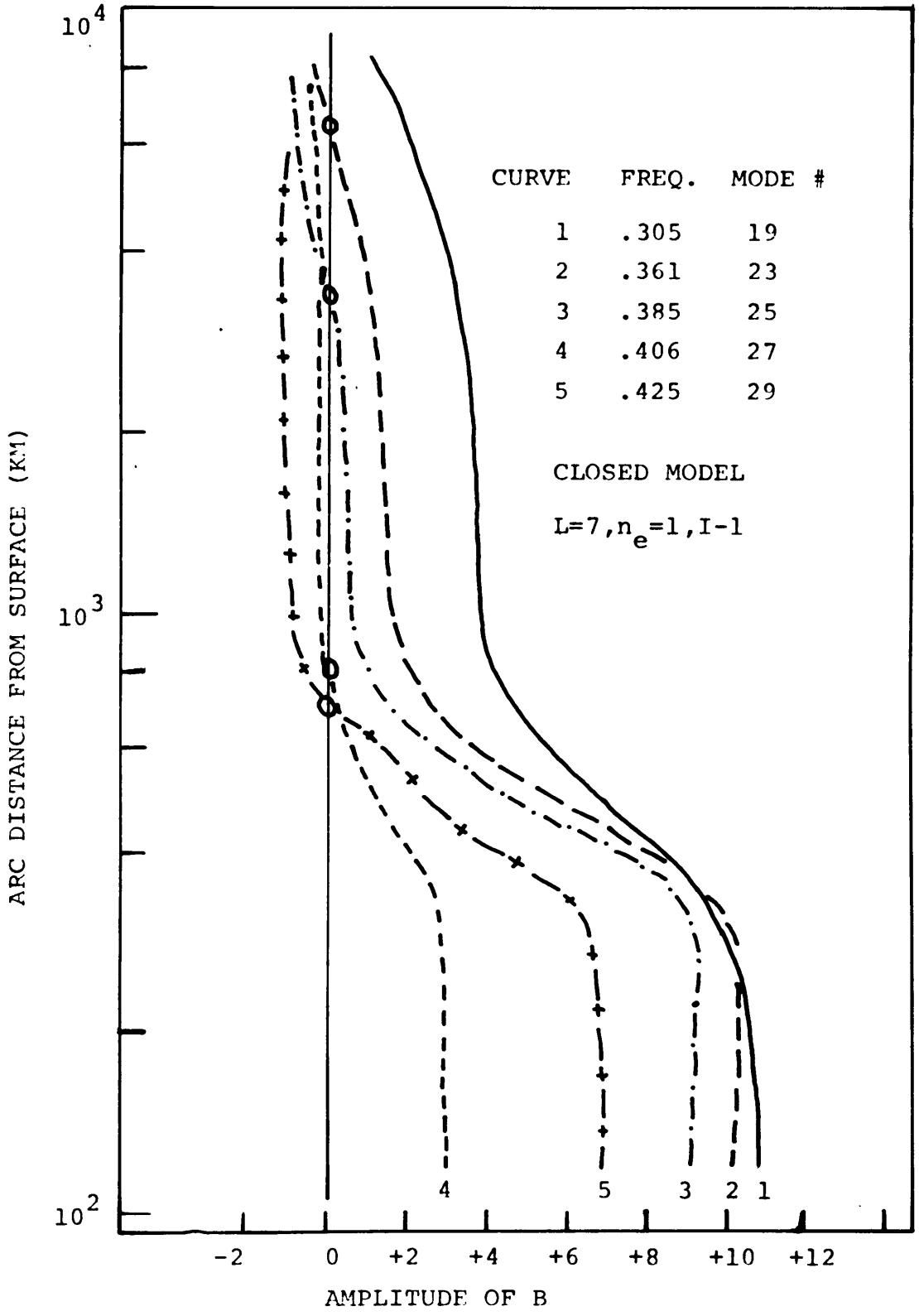

become most important in the region of the ionospheric resonance, leading to a reduction of the amplitudes and the Q's of the peaks. The appearance of these spectra are different from those for the open models which show a broad transparent region in the neighborhood of the ionospheric resonance. These two types of models are quite different in that the open model loses most of the energy generated by the source into the half space while in the closed model the energy in trapped in the system except for that which is dissipated in the ionosphere.

In light of the above discussion, it is interesting to note that in the closed model the ratio of field at the surface to that at the equator increases for those peaks in the region of the ionospheric resonance even through the magnitudes of the fields at the equator and the surface has decreases (see also figure 3.4.7). The ratio of the field at the surface to that at the equator for peaks far removed from the ionospheric resonance is about .3 and for peaks in the resonance region about 3. so that there is about a 10 to 1 increase in this ratio which is about the same order as the increase in amplitudes for the open model. In this sense the closed model also exhibits a transparent window in the region of the ionospheric resonance.

Increasing the collision frequency (Ionospheric Model I-2) lowers the amplitudes and Q's of the peaks near the ionospheric resonance as can be seen by comparing the two top curves in figure 3.4.9. In addition, the frequencies of the peaks in the region from .35 to .43 cps

FIGURE 3.4.9

AMPLITUDE VS FREQUENCY , LOW AND HIGH COLLISION FREQUENCY

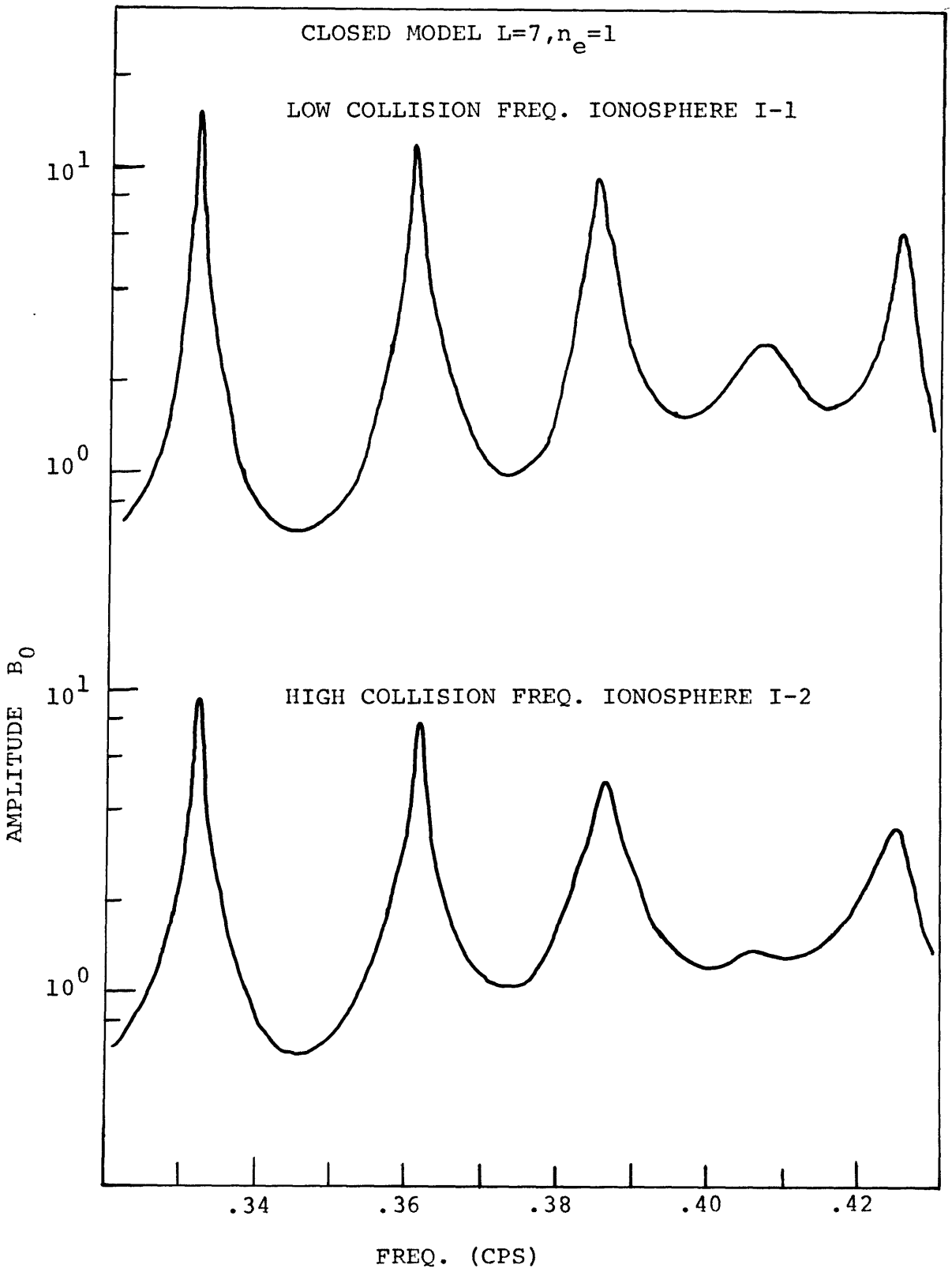

are slightly shifted; outside of this region the Q's are slightly lowered but the peak frequencies are not appreciably altered.

One difficulty with the closed model presented here is that it does not allow for certain losses of energy out of the system that undoubtedly occur and so the Q's from this model are probably unrealistically high. One of the losses will result from the less than perfect guiding of the waves and another is the result of the coupling of wave energy into the isotropic Alfven wave. It is this wave energy in the isotropic mode that is trapped in the low velocity wave guide centered at 400 km.

Prince, Bostick and Smith (1964) have stated that in their model studies of transmission through the ionosphere that most of the wave mode coupling was generated below 200 km. In this region both the electron and ion collision frequencies increase rapidly. This results in an increase in the KX dielectric tensor component which we have seen couples the various field components (equation 3.2.11). The effects of the loss of energy into the waveguide will then be similar to increasing the collision frequencies as it is the collisional coupling that allows the generation of the isotropic wave.

The data from the closed model studies presented so far show several interesting features. First, that the frequencies of the resonant modes are determined mainly by the properties of the magnetosphere with the ionosphere playing a minor role except in the region of its resonance where the frequencies and the Q's may be

noticeably altered. It is important not to underplay the significance of the ionospheric resonance with respect to the observation of hydromagnetic emissions at low latitudes. Since the velocities of the two Alfven modes are not greatly different for propagation along the field, the isotropic mode will also have ionospheric resonances for vertically propagating waves at nearly the same frequencies as the anisotropic wave. Manchester (1966) has shown that the steepest mode angle for propagation down the waveguide is around 89^{o}, so that the vertical resonance frequency is essentially the same as the cutoff frequency. He has also shown that the mode angle decreases rapidly as the frequency increases above the cutoff. A relatively small band of frequencies will then find a large range of mode angles at which energy can propagate in the waveguide. This should make for efficient coupling of energy into the waveguide for frequencies just above the cutoff.

The plot of mode number vs. frequency for the L=7, $n_e=1/cm^3$, I-1 model are presented for a wide range of mode numbers in figure 3.4.10. The curve through the points is relatively smooth except in the region of the ionospheric resonance. Note also the increase in the slope as the frequency increases; this is a reflection of the dispersive velocity in the region near the equator. In this case the equatorial gyrofrequency is 1.39 cps so that the normalized frequency F is about .5 for the highest frequencies shown (.7 cps).

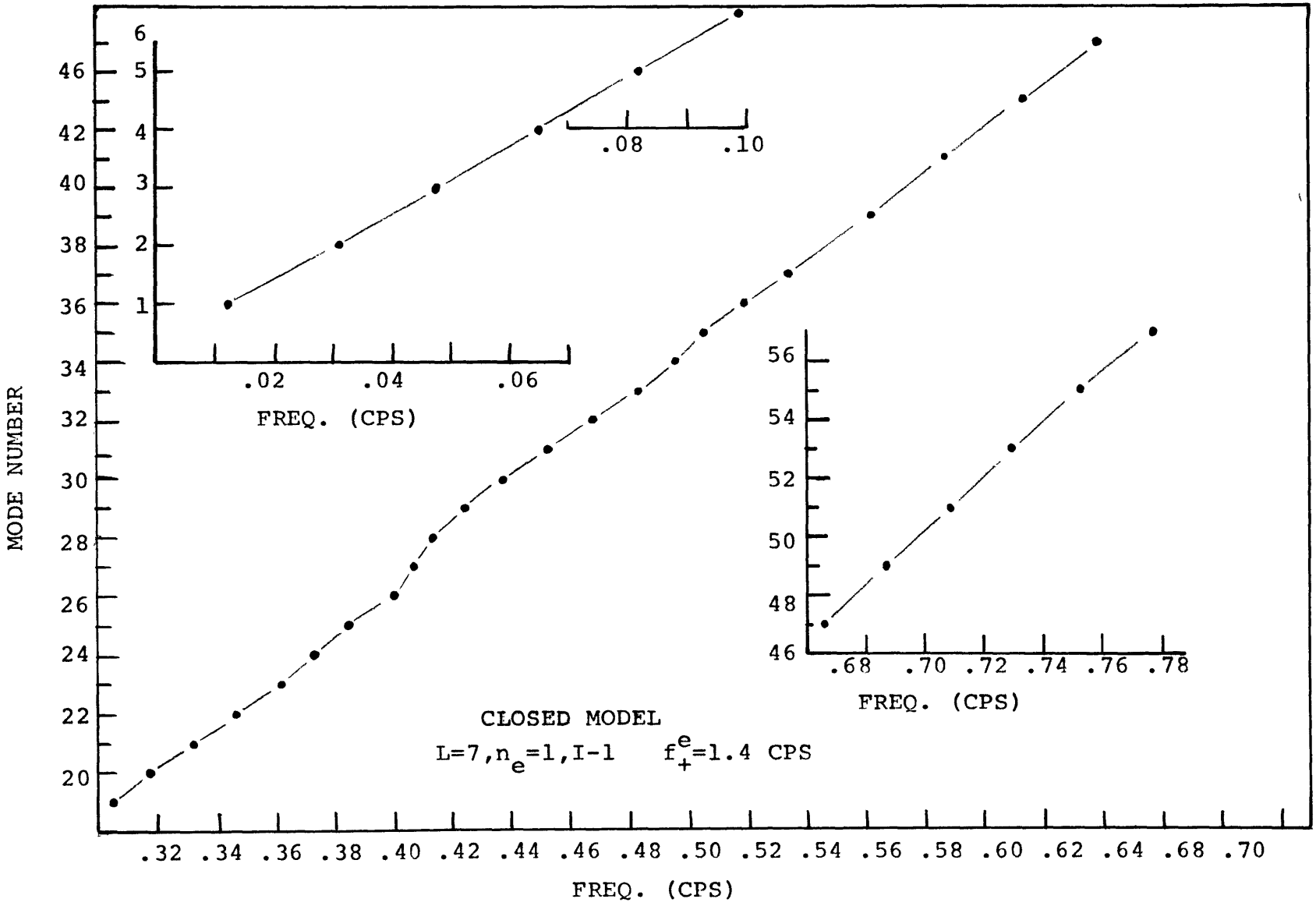

FIGURE 3.4.10

MODE NUMBER VS FREQUENCY

I-1, L=7, n_e=1

FIGURE 3.4.11

MODE NUMBER VS FREQUENCY

I-1, L=7, n_e=2.7

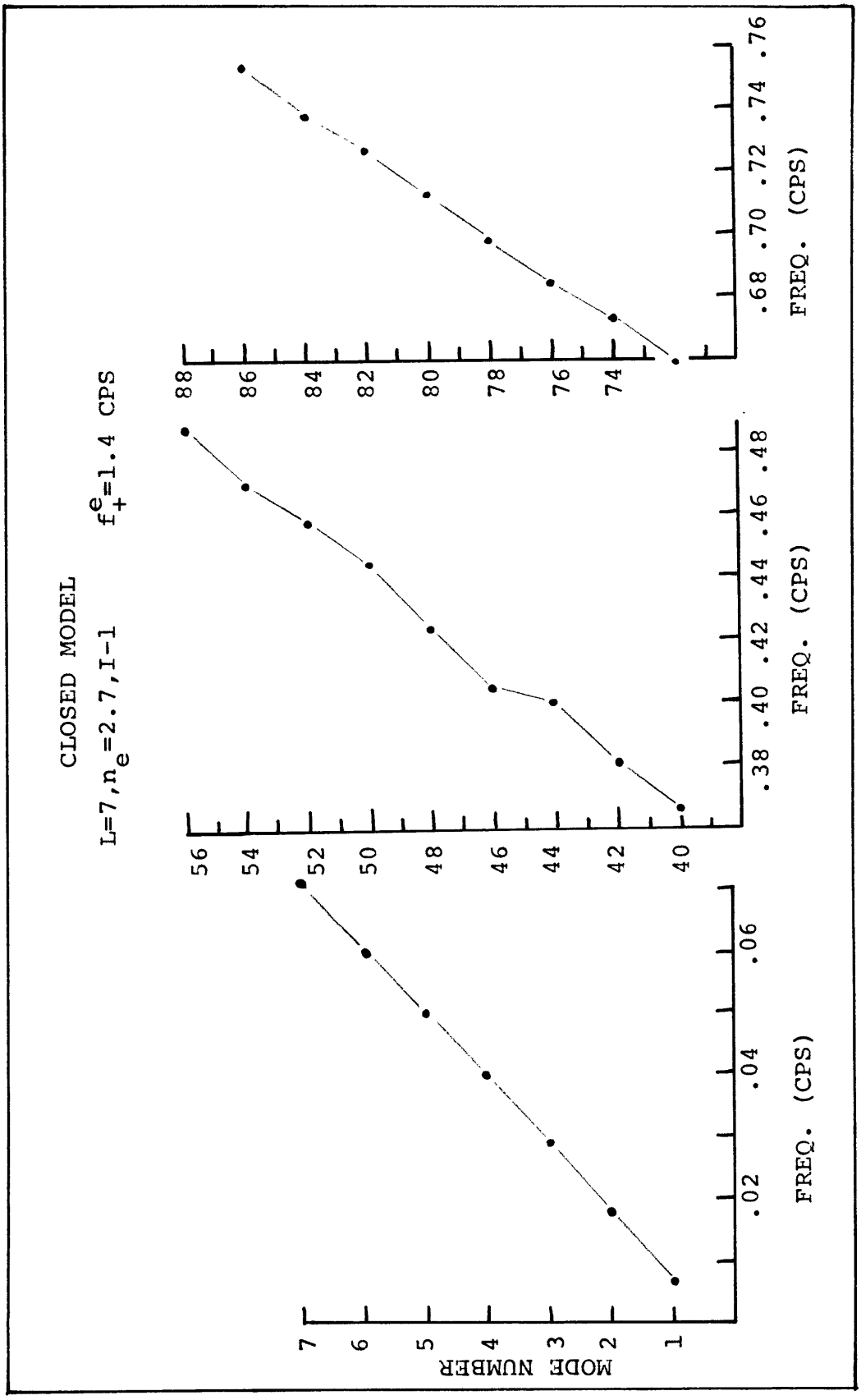

In figure 3.4.11 are presented a set of mode number vs. frequency curves for a model with a high density magnetosphere, $n_e = 2.7/cm^3$, L = 7 and the night-solar minimum ionosphere (I-1). The velocity in this model is lower than in the previous case and the mode frequencies are lower and spaced closer together. The frequencies of the low order modes for this model can be predicted quite accurately by multiplying the resonant frequencies for the $n_e = 1/cm^3$ model by the ratio of the phase travel times in the models as can be seen in Table 3.4.2.

Table 3.4.2

Frequencies of the first four modes for the L = 7, $n_e = 2.7/cm^3$ model compared with those predicted from the $n_e = 1/cm^3$ model.

Mode no.	$n_e = 2.7$	Predicted from $n_e = 1.0$ calculations
1	.007	.0074
2	.018	.0189
3	.029	.0302
4	.040	.0411

Although this technique is not valid for determining the peaks of the higher modes where dispersion is important it can be used to roughly scale the separation of the peaks at these high frequencies. In the $n_e = 1/cm^3$

model the average separation of every other peak is about .023 cps at .7 cps; multiplying this number by the ratio of the travel times (.63) we get a predicted separation of .0139 which compares favorably with the average calculated separation of these frequencies of .014 cps.

As an illustration of the effects of the L parameter on the resonant frequencies the calculations were carried out for a model with L = 8, $n_e = 1/cm^3$ and the solar minimum ionosphere. The results are given in figure 2.4.12. This model and the one for L = 7, $n_e = 2.7/cm^3$ had nearly identical phase travel times (T_o); 101.1 and 102.4 sec respectively. We see from figures 3.4.12 and 3.4.11 that the frequencies of the first seven modes are the same; however we note that at the higher frequencies where the dispersion is important that the slopes for L = 8 are steeper since the ion gyrofrequency is lower along this line (.93 compared to 1.39 cps).

FIGURE 3.4.12
MODE NUMBER VS FREQUENCY
I-1, L=8, n_e=1

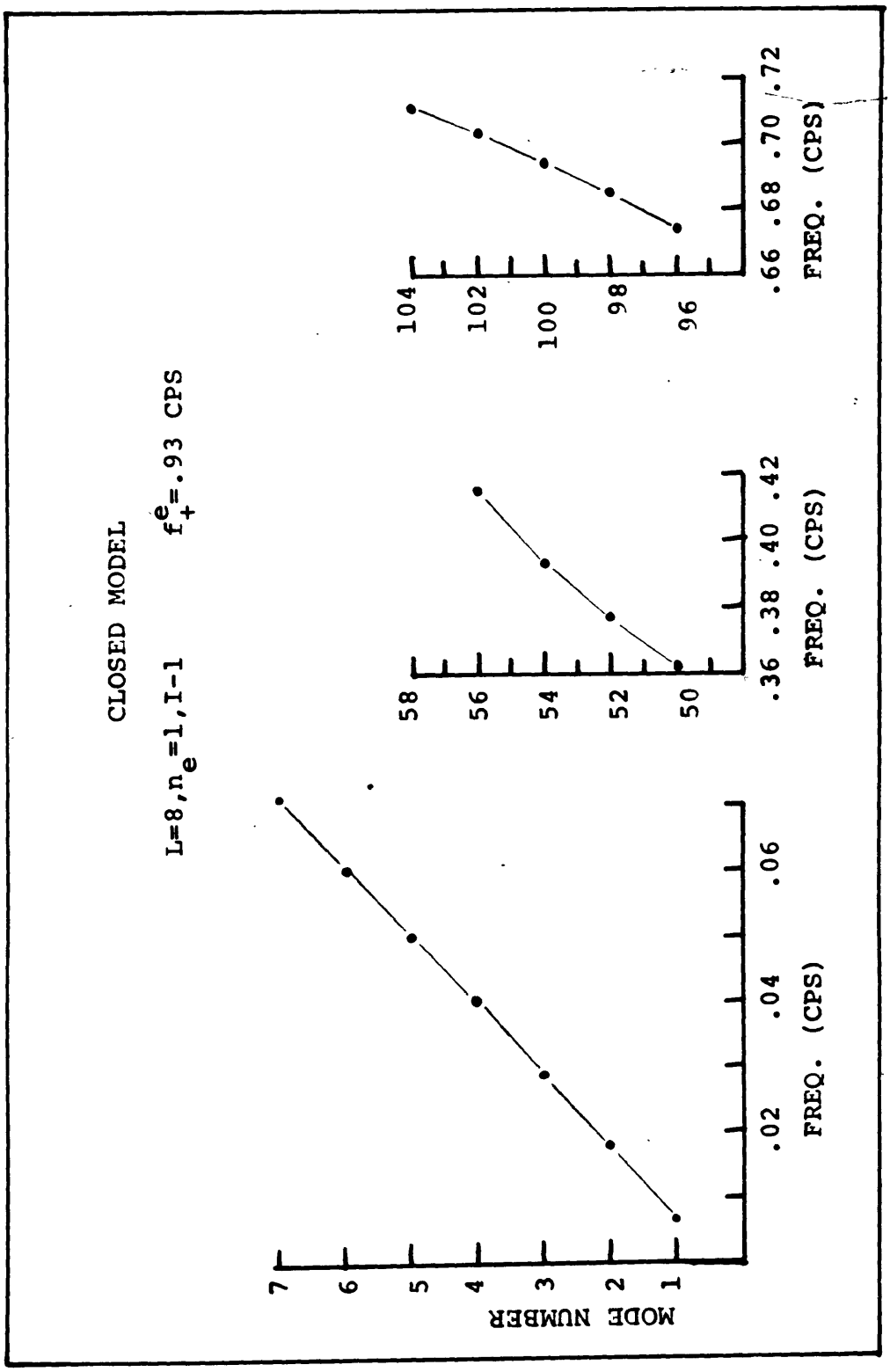

3.5 Discussion of Results and the Fine Structure

We have seen in the preceeding section that a source in the closed model sets up a series of resonant modes. The random fluctuations due to the solar wind and other sources should excite many of these modes. The background of waves should then have a spectrum characteristic of these resonances. When the conditions are favorable, i.e. there exists a proper distribution of energetic particles with a pitch angle anisotropy, the particles can transfer large amounts of energy into the waves. The plasma instability will then amplify the spectrum of background waves in some band of frequencies below the gyrofrequency.

The spectrum will then be given by the product of the amplification and background spectra. The source amplification spectrum as given by Leimohn (1967) has in general a sharp high frequency cutoff at .5 to .8 the equatorial ion gyrofrequency, a maximum just below the cutoff and a slow rate of falloff on the low frequency side (figure 3.5.1).

The waves are amplified in the region near the equator and then propagate to the surface. The wave spectrum as seen at the surface will then be further modified by the propagation through the magnetosphere and the ionosphere. This modification of the spectrum is given by the open model calculations. The spectrum as seen at the surface is given by multiplying the product of the resonant mode and the source amplification spectra by the open model spectrum. The final spectrum

FIGURE 3.5.1

EMISSION SPECTRUM AT VARIOUS STAGES

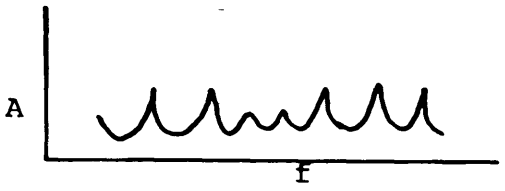

1 BACKGROUND
MODES DETERMINED BY
FIELD LINE AND DENSITY

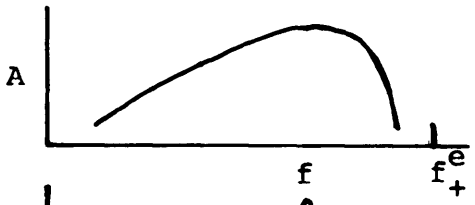

2 SOURCE
SHAPE DETERMINED BY
PARTICLE DISTRIBUTION
FUNCTION

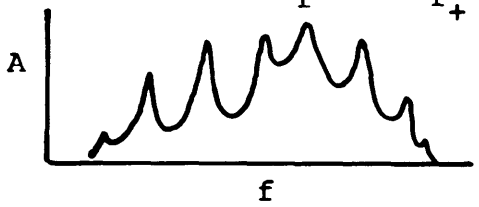

3 AFTER AMPLIFICATION
AT EQUATOR
1x2

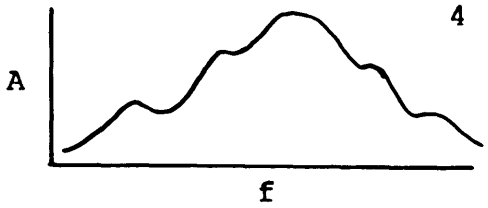

4 TRANSMISSION SPECTRUM FOR
MAGNETOSPHERE AND IONOSPHERE
TRANSPARENT REGION DETERMINED
BY IONOSPHERIC RESONANCES

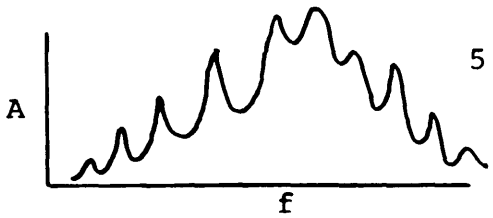

5 AT SURFACE
1x2x4

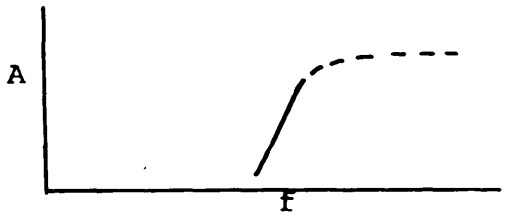

6 WAVEGUIDE

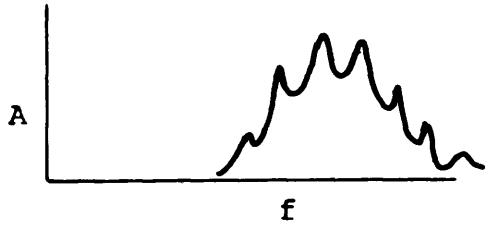

7 AT LOW LATITUDES
5x6

as observed at lower latitudes will be modified by the waveguide response which will introduce a low frequency cutoff near the frequency of the ionospheric resonance. The spectrum is shown schematically at various stages in figure 3.5.1.

The calculations in section 3.4 have shown that the low order mode frequencies for variations in the density and the L value can be determined quite accurately by multiplying the frequencies by the ratios of the travel times (Table 2.4.2). Although the resonant frequencies of the higher order modes cannot be determined in this fashion, we can determine the separation between the modes by this same scaling.

In order to apply some of the previous results to the observed fine structure of hydromagnetic emissions the change in the separation of the mode frequencies has been determined from the model calculations. These results are presented in figure 3.5.2 the constant k gives the separation between the modes as a function of the normalized frequency (F) through the formula $\Delta f = k \Delta f_o$. Where Δf_o is the separation between the low order modes.

From this curve the region of validity of the empirical relation for the observed separation ($\Delta f = 1/T_o$) can be shown. Take for example the results of the closed $L = 7, n_e = 1$ model (Table 3.4.1). The separation between the low order modes is .017 cps and $T_o = 64.6$. The empirical relation would give a separation of $\Delta f = 1/T_o = .0155$. From figure 3.5.2 we see that at F = .2 the separation between every other modes is, $\Delta f = .91 \times$

FIGURE 3.5.2

CHANGE OF MODE SEPARATION (Δf) WITH FREQUENCY

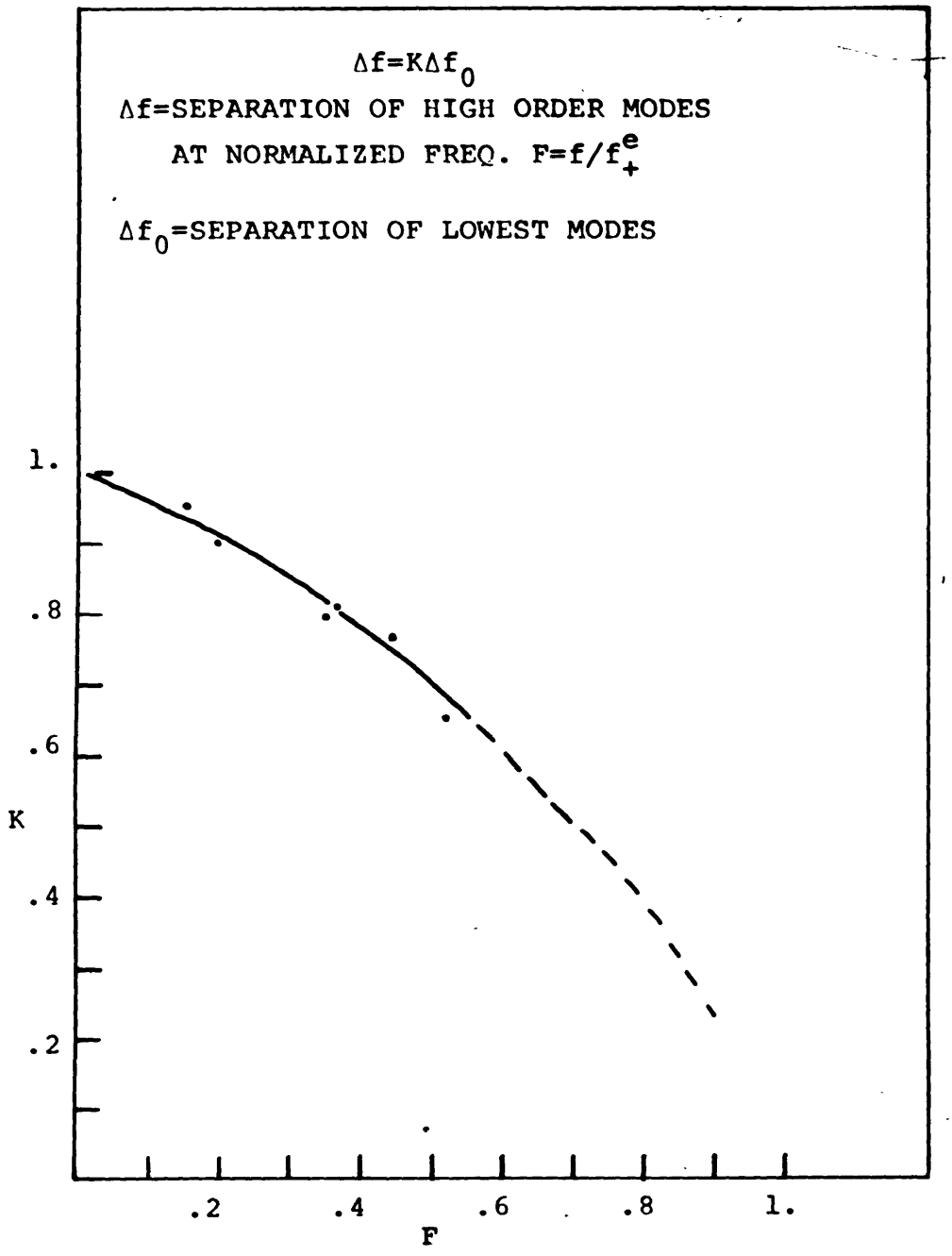

(.017) = .0155. At the higher frequencies normally present in hydromagnetic emissions (F ≅ .4) the observed separation whould be smaller than that given by the empirical relation.

We turn our attention now to some examples of the observed fine structure and the interpretation of this fine structure in terms of the results of the closed model studies.

The dispersion measurements for the event of 7/4/67 provides the following data (Table 2.5.1); L = 5.9 and T_o = 90 sec. Making use of the results for the closed model for L =7 and T_o =64.6 sec we can calculate the frequencies of the low order modes by multiplying the model frequencies by the ratio of the travel times (64.6/90. = .72). The low modes are given in Table 3.5.1.

Table 3.5.1

Low order modes for 7/4/67 calculated from the closed model for L = 7, n_e = 1., T_o 64.6

Mode	Frequency	Δf
1	.0085	
2	.0222	.0137
3	.0345	.0123
4	.0468	.0123

The separation between the modes at the frequencies of this event (F = .35) will down by about 20% (figure 3.5.2). The separation between neighboring modes is then .00985;

FIGURE 3.5.3

SPECTRA OF THE EMISSION OF 7/4/67

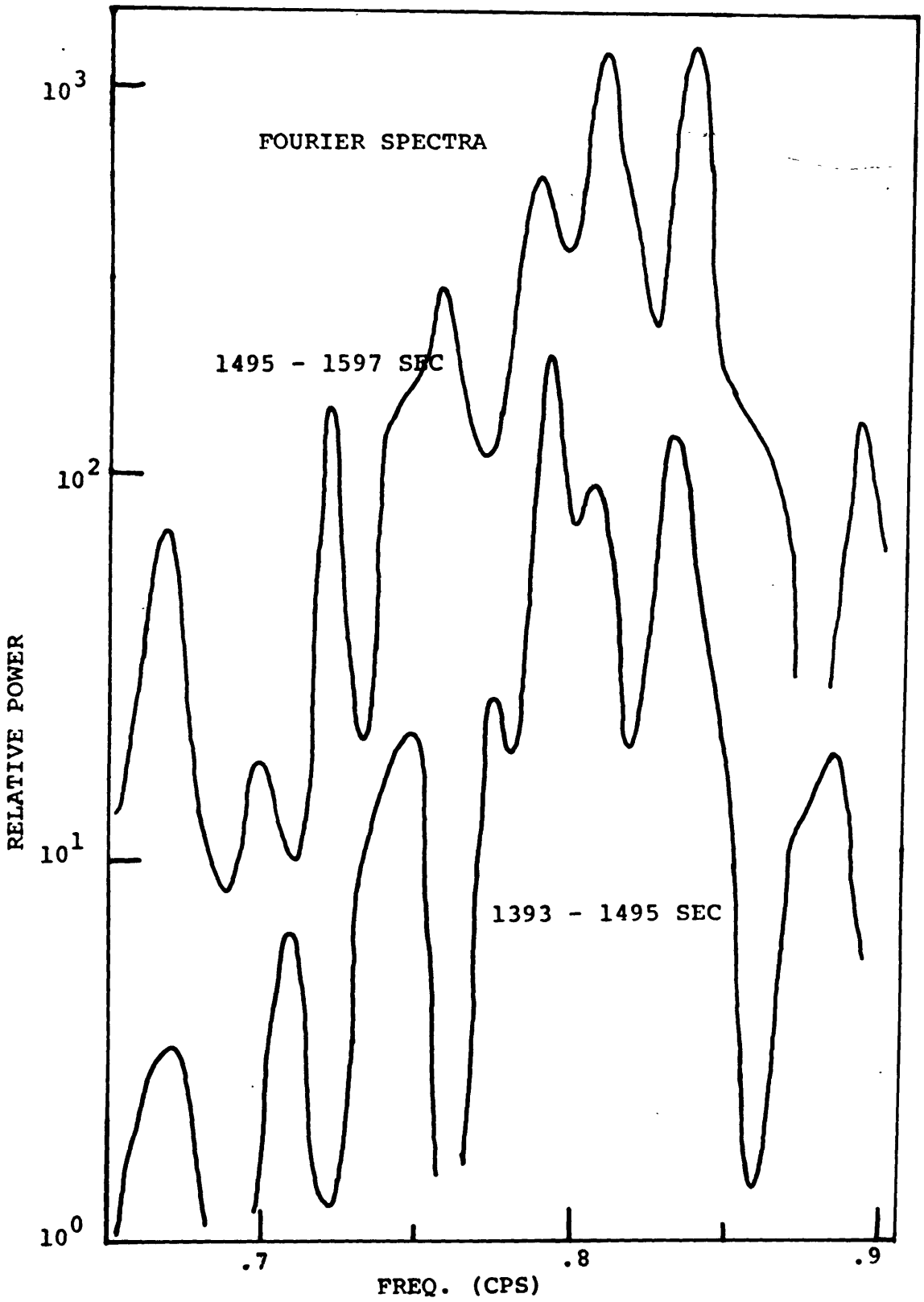

between every other mode it is .0197 and between every third mode it is .0295.

Figure 3.5.3 shows the Fourier spectra for 102 second data samples from the event of 7/4/67. The locations of the peaks in these spectra are given in Table 3.5.2.

Table 3.5.2

Peaks in the Spectra of the Emission of 7/4/67.

1495 - 1597 sec.		1393 - 1495 sec.	
f	Δf	f	Δf
.747	.025	.722	
.772		.760	.038
.791	.019	.790	.030
.811	.020	.810	.020
.830	.019	.840	.030
.889	.059	.896	.056
.918	.029	.922	.026
.947	.029	.950	.028
.986	.039	.965	.016
1.015	.029	.996	.030
1.045	.030	1.015	.019
1.074	.029		

Table 3.5.2 shows that there are peaks which have separations of 2 modes (.019), of 3 modes (.029) and of 4 modes (.039).

The emission of 4/29/66 had L = 8.3 and T_o = 98 sec as determined from the dispersion analysis (Table 2.5.1). The separation of the low order modes calculated from the L = 8, T_o = 101 sec closed model would be .0113 cps. The normalized midfrequency for this event is .45 so that the separation of the modes should be .75 (.0113) = .0085 cps (figure 3.5.2). A Fourier spectrum of this emission was shown in figure 2.4.5 and the peaks from this and a similar spectrum are summarized in Table 3.5.3

Table 3.5.3

Peaks in the spectra of the the emission of 4/29/66

1300 - 1500 sec		2600 - 2800 sec	
f	Δf	f	Δf
.420	.010	.420	
.430	.010	.435	.015
.455	.025	.449	.014
.472	.017	.459	.010
.490	.018	.474	.015
.510	.020	.493	.019
.532	.022	.513	.020
.550	.018	.527	.014
.566	.016	.542	.015
.585	.019	.576	.034
.595	.010	.586	.010

Here we see separations of the order of one mode (.0085), two modes (.017), three modes (.025) and four modes (.034). The average separation between modes as

FIGURE 3.5.4

SPECTRUM OF THE EMISSION OF 6/9/60

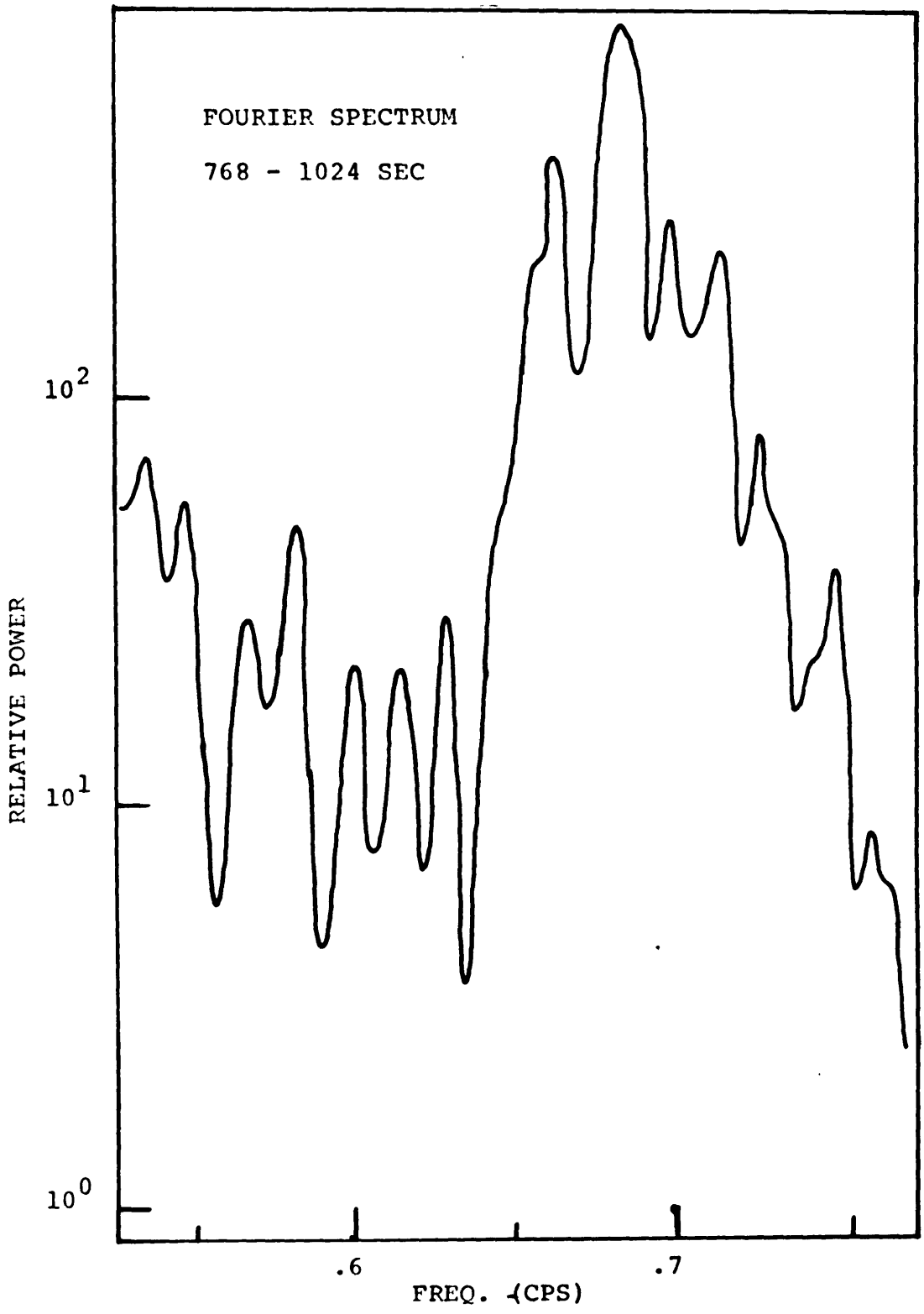

determined from Table 3.5.3 are .0087 (1300-1500 sec) and .0083 (2600-2800 sec). These are in good agreement with the predicted mode separation of .0085 cps.

Dispersion measurements for the emission of 6/9/60 yield the following parameters, L = 7.6 and T_o = 91 sec. The low order mode separation as determined from theL = 7, T_o = 64.6 closed model is .0123 cps. The mode separation at the higher frequencies of this emission is .7 (.0123) = .0085. A Fourier spectrum for this emission is presented in figure 3.5.4 and a summary of the peaks is presented in Table 3.5.4.

Table 3.5.4

Peaks in the spectra of the emissions of 6/9/60 and 6/13/67

6/9/60 768 - 1024 sec		6/13/67 0 - 102	
f	Δf	f	Δf
.580		1.128	
.600	.020	1.145	.017
.615	.015	1.63	.018
.630	.015	1.179	.016
.662	.032	1.201	.022
.685	.023	1.216	.015
.700	.015	1.240	.024
.715	.015	1.265	.025
.725	.010	1.314	.049
.750	.025	1.343	.029
		1.372	.029
		1.400	.028

The peaks appear to be separated by 1,2,3 and 4 modes. On this basis the average separation between modes is .0081 cps compared to the predicted separation of .0085 cps.

Table 3.5.4 also contains a list of the peaks in the emission of 6/13/67. The dispersion measurements for this event give L=4.6 and T_o=67. The closed model results for the L=7, T_o=64.6 would predict for this case a low order mode separation of .0164 cps. The normalized frequencies for this emission are of the order of .2 so that the expected separation between modes is .0148 cps. The peaks in Table 3.5.4 are of the order of one, two and three times this value. The average separation between modes from Table 3.5.4 is .0152 cps which compares favorably with that predicted from the model results (.0148).

Chapter 4

SUMMARY AND SUGGESTIONS FOR FUTURE WORK

The results of the first chapter show that the dispersion is most strongly affected by the distortion of the dipole field lines. At a fixed local time the dispersion increases as the equatorial crossing point (L value) approaches the magnetopause boundary and it increases for a given L value as the local time progresses from midnight to noon. For local times within a few hours of midnight and for field lines crossing the equator at less than half the distance to the magnetopause, the distortion of the field lines is small and the dipole calculations for dispersion should be adequate. Using dispersion curves based on a dipole field rather than the distorted dipole will result in L values which are too small and densities which are too large.

The observational data presented in Chapter 2 is in agreement with the results of other workers in the field. That is the emissions occur predominately during periods of moderate geomagnetic activity and that the interpretation of the dispersion measurements indicate that the waves propagate in the rarified plasma exterior to the plasmapause. With respect to the observations of the activity in the various Pc bands, several interesting examples of a simultaneous decrease in the Pc2-3 activity

coupling into the waveguide and its transmission properties exerts a controll over what will be observed at the lower latitudes where many of the observation sites are located.

APPENDIX A

ALFVEN WAVE PROPAGATION

Several books (Allis, et. al. 1962; Stix, 1962) discuss in general the propagation of waves in a plasma. The purpose of this appendix is to present briefly the propagation characteristics of Alfven waves in a plasma such as the magnetosphere. Following in part the notation of Allis (1962) the expression for the index of refraction is given by equation A-1.

$$
\begin{aligned}
n_{\pm} &= (B \pm D)/2A \\
A &= KT \sin^2\theta + KP \cos^2\theta \\
B &= KR\ KL \sin^2\theta + KP\ KT\ (1+\cos^2\theta) \\
C &= KR\ KL\ KP \\
D &= B^2 - 4AC
\end{aligned}
\qquad \text{(A-1)}
$$

The angle θ is the angle between the propagation vector and the magnetic field. (See figure A-1). Since the displacement currents associated with Alfven waves in the magnetosphere are negligible, the components of the dielectric tensor ($\overline{\overline{K}}$) can be written as:

$$
\begin{aligned}
KL &= C^2/V_a^2\,(1-F_+)(1+F_-) & KX &= .5\,j(KL-KR) \\
KR &= C^2/V_a^2\,(1+F_+)(1-F_-) & F_{\pm} &= \omega/\Omega_{\pm} = \omega/|e|B/m_{\pm} \\
KT &= .5\,(KL+KR) & C^2/V_a^2 &= C^2 4\pi n m_+/B^2 \\
KP &= C^2/V_a^2\,F_+\,F_-
\end{aligned}
\qquad \text{(A-2)}
$$

Combining equations A-1 and A-2 the phase velocity is

$$v_{\pm} = \frac{\omega}{k_{\pm}} = \sqrt{2}\, V_a \left[\frac{(1-F_+^2)(1-F_-^2)\cos^2\theta - F_+F_-(1-F_+F_-)\sin^2\theta}{1+\cos^2\theta - 2F_+F_- \pm \left\{4(F_+-F_-)^2\cos^2\theta + \sin^4\theta\right\}^{\frac{1}{2}}} \right]^{\frac{1}{2}} \qquad \text{(A-3)}$$

In the above equation the plus and minus signs refer to the left-ordinary and the right-extra ordinary waves respectively (Allis, 1962). The left-ordinary (+) wave has left-circular polarization for propagation parallel to the magnetic field. This wave is often called the anisotropic or slow Alfven wave. The right-extraordinary wave (-) has right-circular polarization for propagation parallel to B_o and is also referred as the isotropic or fast Alfven wave. Hereafter the notation L and R will be used interchangeably with + and - . Equation A-3 is correct for all angles of propagation provided the displacement currents can be neglected. This equation can be simplified somewhat by making use of the quasicircular

Figure A-1

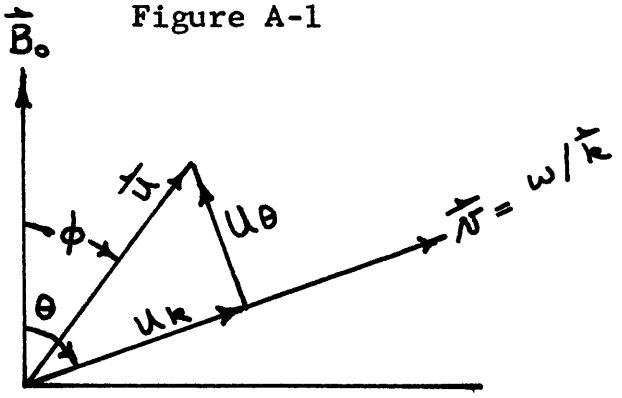

(quasilongitudinal) and the quasiplane (quasitransverse) approximations; however for frequencies of the order of the gyrofrequency (F+ → 1) there is a range of angles ($40^{\circ} < \theta < 65^{\circ}$) in which neither approximation is very good. For the simple case of propagation parallel to the field the phase and group velocities for the left-ordinary wave are ($F_- << 1$)

$$v_L = \omega / k_L = V_a (1 - F_+)^{1/2} \tag{A-4}$$

$$u_L = \frac{\partial \omega}{\partial k} = \frac{V_a (1 - F_+)^{3/2}}{(1 - .5 F_+)} \tag{A-5}$$

For propagation at any arbitrary angle the group velocity is found by evaluating equation A-6 (Stix, 1962). (See Figure A-1)

$$u = \hat{k} \frac{\partial \omega}{\partial k} + \hat{\theta} \frac{1}{|k|} \frac{\partial \omega}{\partial \theta} = \hat{k} u_k + \hat{\theta} u_\theta \tag{A-6}$$

The components of the group velocity along the direction of the phase velocity (u_k) and perpendicular to k (u_θ) are given in equations A-7 and A-8.

$$u_k^I = V_a v_\pm / (1 + a + b_\pm) \tag{A-7}$$

where

$$a = [\cos^2\theta\{F_+^2(1-F_-^2)+F_-^2(1-F_+^2)\}+\sin^2\theta\, F_+F_-(1-2F_+F_-)]/C$$

$$b_\pm = 2[-F_+F_- \pm (F_+-F_-)^2\cos^2\theta/S]/d_\pm$$

$$C = (1-F_+^2)(1-F_-^2)\cos^2\theta - F_+F_-(1-F_+F_-)\sin^2\theta$$

$$d_\pm = 1+\cos^2\theta - 2F_+F_- \pm S$$

$$S = [4(F_+^2-F_-^2)\cos^2\theta + \sin^4\theta]^{1/2}$$

$$U_\theta^\pm = -U_k^\pm \sin\theta\cos\theta\,[e+f_\pm] \qquad \text{(A-8)}$$

where

$$e = -[(1-F_+^2)(1-F_-^2)+F_+F_-(1-F_+F_-)]/C$$

$$f_\pm = [-1 \pm (-2(F_+-F_-)^2+\sin^2\theta)/S]/d_\pm$$

Equations A-3, A-7 and A-8 have been evaluated for the left-ordinary wave and the results are shown in figures A-2 and A-3. Figure A-2 illustrates the dependence of the phase velocity on the angle of propagation to the field (θ) and on the ratio of the frequency to the gyrofrequency of the ions (F+). We see first that at any frequency as the angle to the field increases the phase velocity decreases until at $\theta = 90^\circ$ the wave ceases to propagate and as the frequency approaches the gyrofrequency of the ions the phase velocity decreases. Figure A-3 shows the trajectory of the tip

of the group velocity vector as the angle θ varies from 0^{o} to 80^{o}. We see that as the frequency increases ($F+\rightarrow 1$) the magnitude of the group velocity decreases and that for frequencies less than $.7\Omega+$ the group velocity vector is confined to within 10^{o} of the magnetic field direction.

FIGURE A-2

PHASE VELOCITY SURFACE v_L POLAR DIAGRAM

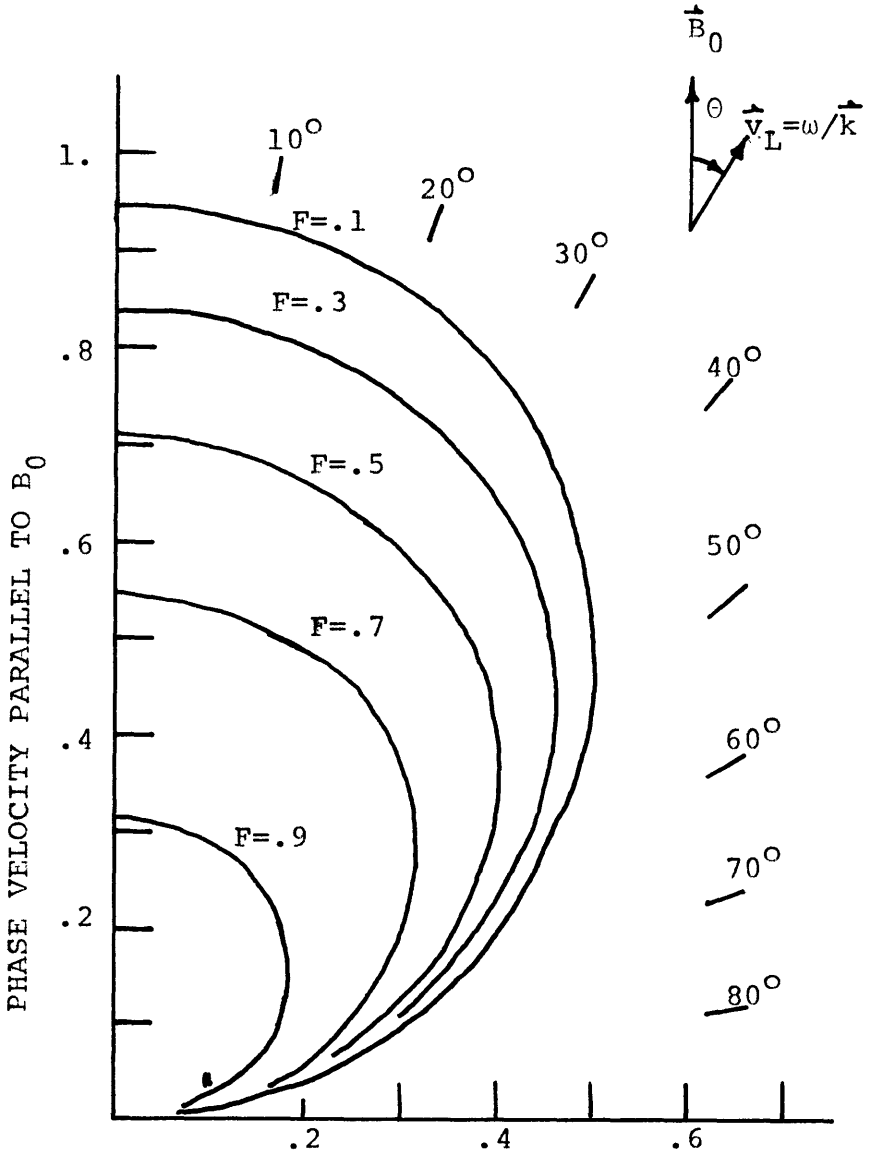

FIGURE A-3

POLAR DIAGRAM OF GROUP VELOCITY u_L

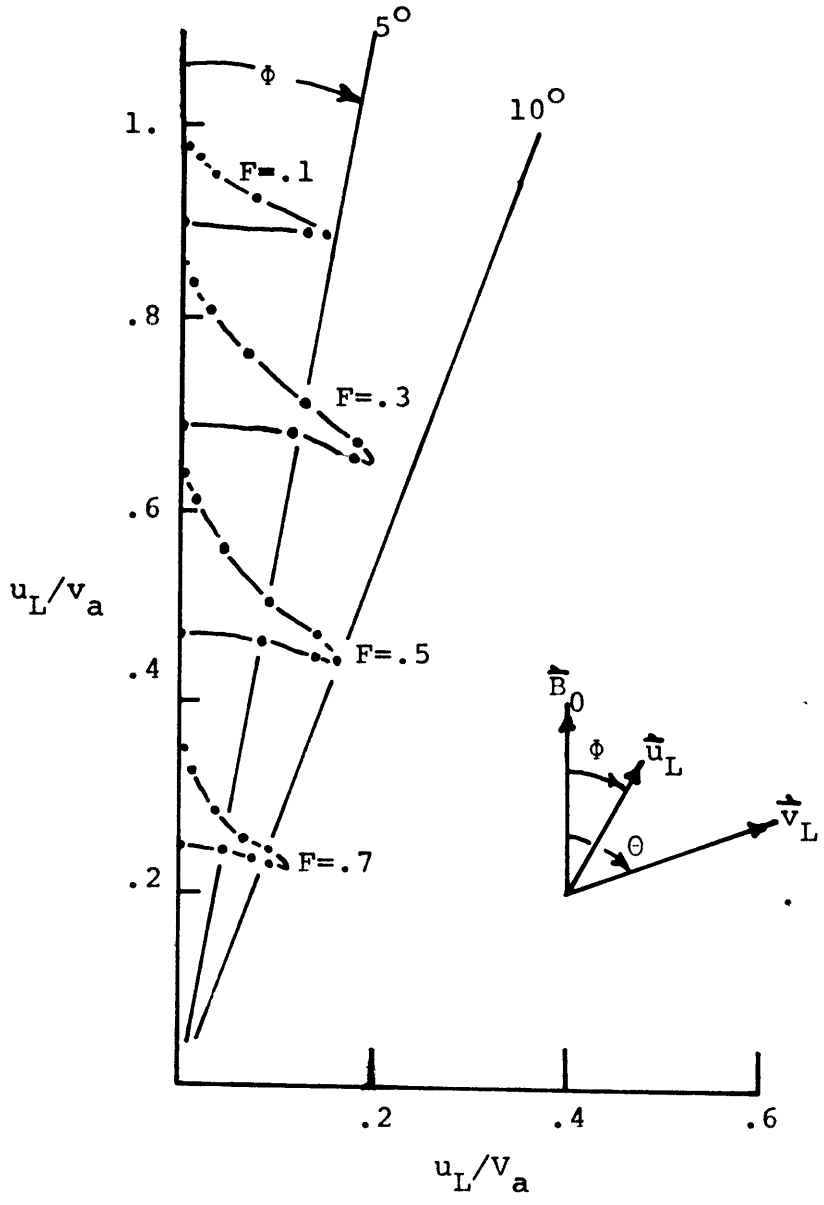

GROUP VELOCITY AS A FUNCTION OF F, POINTS INDICATE MAGNITUDE AND GROUP ANGLE (Φ) OF GROUP VELOCITY FOR 10° INCREMENTS IN THE DIRECTION OF THE PHASE VELOCITY (Θ)

APPENDIX B

RAY PATHS IN A DIPOLE FIELD

In this section the expression for the ray paths of the anisotropic Alfven wave will be derived under the assumption that the propagation characteristics are constant between surfaces of magnetic latitude defined by λ and $\lambda+\Delta\lambda$. Application of Snell's law at these boundaries leads to the expression for the rate of change of the propagation vector k with magnetic latitude. (Thorne and Kennel, 1967).

$$\frac{dk}{d\lambda} = -k\ Cot(\theta-\phi)\left[\frac{d\theta}{d\lambda} - \frac{d\phi}{d\lambda} - 1\right] \qquad \text{B.1}$$

where (see figure B.1)

θ = angle between k and B
δ = angle between k and u_g (Group Velocity)
ϕ = inclination of the magnetic field

Figure B.1

For a dipole field $Tan\,\phi = 2\,Tan\,\lambda$ B.2

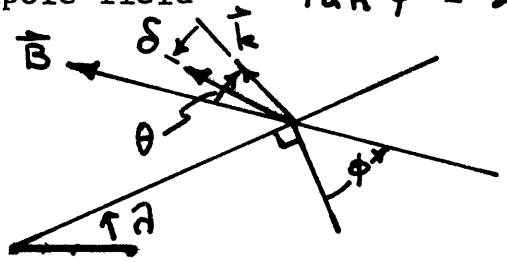

Geometry for Propagation in Dipole Field

The dispersion relation for the Quasi-longitudinal approximation is

$$k = \frac{\omega}{V_a \cos\theta}\left[\frac{1 + F_+ \cos\theta}{1 - F_+^2}\right]^{1/2} \qquad \text{B.3}$$

where Va and F+ are functions of λ as discussed in Chapter 1. For this same approximation (Q-L) the relation for the angle (δ) between the propagation vector and the group velocity is given by equation B.4.

$$\tan\delta = \tan\theta\left[\frac{1 - .5 F_+ \cos\theta}{1 + F_+ \cos\theta}\right] \qquad \text{B.4}$$

The equation for the ray path is (Thorne and Kennel, 1967)

$$\frac{1}{r}\frac{dr}{d\lambda} = \tan(\theta - \delta - \phi) \qquad \text{B.5}$$

For low frequencies (F+ → 0) we find from B.4 that $\delta = \theta$. This result and equations B.5 and B.2 yield the following equation for the ray.

$$\frac{1}{r}\frac{dr}{d\lambda} = -2\tan\lambda \qquad \text{B.6}$$

Integrating this equation we have

$$r = R_e L \cos^2\lambda \qquad \text{B.7}$$

which is the equation of a dipole field line. At low frequencies the ray paths are along the field lines.

When the frequencies are not low we can still obtain a qualitative picture by considering B.4. As a wave proapgates away from the equatorial region F+ will decrease due to the increase in the local gyrofrequency. After some distance F+ will decrease sufficiently so that tan δ = tan θ ; the waves will then be guided to the surface along the field line passing through this point. Equations B.1, B.2 and B.3 can be combined to determine the angle of the propagation vector (θ) as a function of magnetic latitude.

$$\frac{d\theta}{d\lambda} = \frac{1 + 2\cos^2\phi/\cos^2\lambda + Y(\lambda,\theta)\tan\lambda\tan(\theta-\phi)}{1 + \tan(\theta-\phi)[\tan\theta - .5 F_+ \sin\theta]} \qquad \text{B.8}$$

where

$$Y(\lambda,\theta) = 2(1+1.5a) + \frac{3F_+\cos^6\lambda(1+.5a)}{[4-3\cos^2\lambda]^{1/2}}\left[\frac{\cos\theta}{N} + \frac{2F_+\cos^6\lambda}{D}\right]$$

$$a = \cos^2\lambda/(4-3\cos^2\lambda) \qquad \text{B.9}$$

$$N = 1 + F_+\cos^6\lambda\cos\theta/[4-3\cos^2\theta]^{1/2}$$

$$D = 1 - F_+^2\cos^{12}\lambda/(4-3\cos^2\theta)$$

Equations B.5 and B.8 were numerically integrated and the results are presented in figures B.2 and B.3.

Figure B.2 shows the change in angle (θ) between the magnetic field and the propagation vector (k) as a function of angle (λ) along the ray path for the case where F=.5. We see that regardless of the initial angle (θ_o) the propagation vector tends to become perpendicular to the field lines at high latitudes as the ray approaches the surface. For F greater than .5 the approach to the asymptotic values $\pm 90^o$ is faster than in the above case and for F less than .5 it is slower.

These results indicate that it might be useful to study the propagation of the anisotropic wave when the angle between the field and the propagation vector is large. The anisotropic wave has a transverse left-circular polarization only when θ equals zero; for other angles the waves will be circularly polarized perpendicular to k and in addition will have a component of E parallel to k (Q-L approximation).

Most of the theoretical work on the cyclotron resonance instability has been confined to the case of propagation parallel to the field. If the instability is limited to approximately transverse, circularly-polarized waves (θ small) then figure B.2 indicates that the region of the instability for any one wave is quite limited.

The inner three ray paths, in figure B.3a illustrate the effects of increasing the frequency with zero initial angle. The ray path for F=0 is along the dipole field

line and as the frequency increases the rays travel at greater radial distances. The largest increase in radial distance is less than 5 percent and the increase in arc length along the rays is less than 5 percent. The ray for $\theta_o = 40^o$, F= .8 has the first part of its trajectory outside of the ray with $\theta_o = 0^o$ and the last part ($\lambda > 30^o$) interior to this ray. This results from the fact that when θ_o is large to begin with θ rapidly approaches 90^o (figure B.2).at which point the guiding is perfect (equation B.4) and with a maximum of δ for θ in the range of 30^o to 40^o we can consider the waves as propagating across the field until θ becomes large and/or F+ becomes small at which point the wave locks on to a particular field line and it guided to the surface.

Figure B.3b shows two ray paths for equal but opposite initial angles. The ray with $\theta_o = -30^o$ travels inside the dipole line passing through the same equatorial point and the ray with $\theta_o = +30^o$ travels outside of this field line. For $-30^o < \theta_o < 0^o$ part of the ray path is inside the field and part outside.

We see then that the ray paths are not substantially different from the field lines. The small deviations of the ray paths will affect the dispersion however and these effects are discussed in section 1.5.

FIGURE B-3

RAY PATHS AS A FUNCTION OF Θ_0 AND F

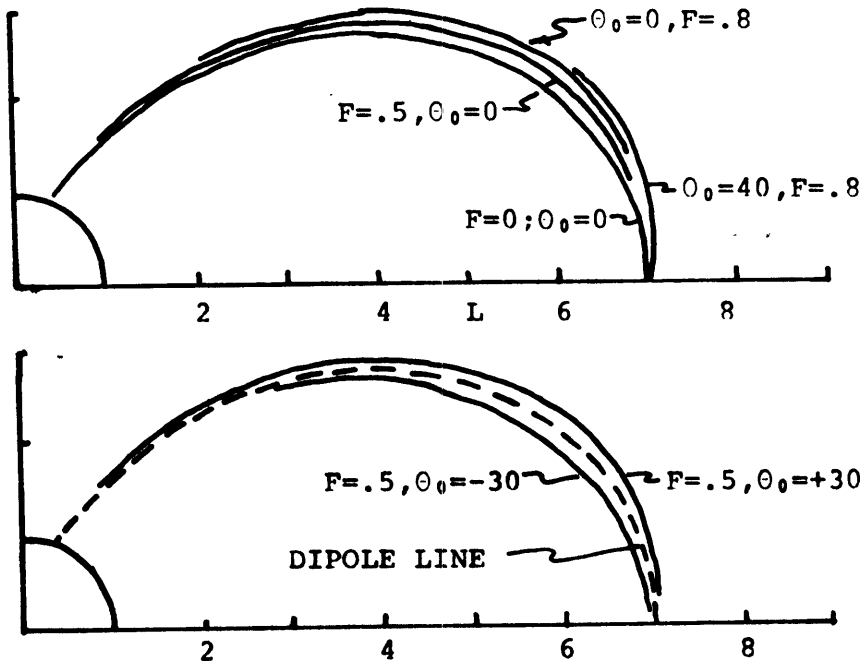

FIGURE B-2

ANGLE (Θ) BETWEEN PROPAGATION VECTOR AND B_0 AS A FUNCTION OF Θ_0 AND LATITUDE λ

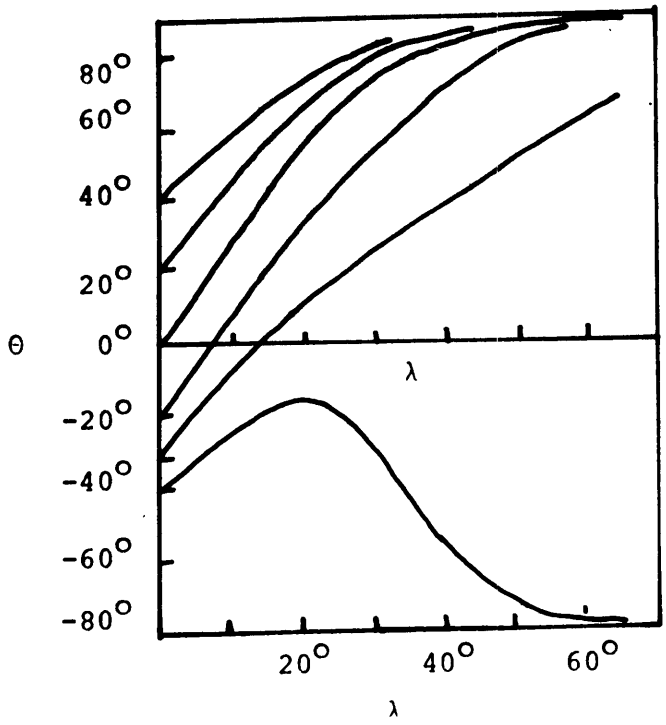

APPENDIX C

DISPERSION DATA

This appendix contains tables of calculated dispersion data. Tables C-1 through C-4 contain the results for a pure dipole field (Section 1.4). Rr is the distance (in R_e) at which the waves are assumed to be reflected. $R_r = 1$ corresponds to reflection from the surface and $R_r = 1.5$ corresponds to reflection at an altitude of 3,000 km. LAT is the latitude at which the given field line intersects the surface.

Tables C-4 through C-14 contain dispersion data for the distorted dipole model (Section 1.6). With a r^{-4} density model. R_b is the radial distance (in R_e) to the magnetopause at the subsolar point.

Table C-1

Dipole Model

$R_r = 1.0$

Density - $n = n_o \left(\frac{R_e}{r}\right)^3$

L	LAT	$f+^e$	$T_o/\sqrt{n_e}$
4	60.0	14.468	5.623
5	63.4	3.824	13.788
6	65.9	2.213	28.649
7	67.8	1.394	53.155
8	69.3	.934	90.776
9	70.5	.656	145.463

T/T_o

L \ F	.1	.2	.3	.4	.5	.6	.7		.8
4	1.07	1.15	1.25	1.38	1.56	1.82	2.24	3.04	5.37
5	1.07	1.15	1.25	1.38	1.56	1.82	2.23	3.03	5.35
6	1.07	1.15	1.25	1.38	1.56	1.81	2.23	3.03	5.34
7	1.07	1.15	1.25	1.38	1.56	1.81	2.23	3.02	5.33
8	1.07	1.15	1.25	1.38	1.56	1.81	2.23	3.02	5.33
9	1.07	1.15	1.25	1.38	1.56	1.81	2.23	3.02	5.33

Table C-2

Dipole Model

$R_r = 1.5$ Density - $n = n_o \left(\frac{R_e}{r}\right)^3$

L	LAT	$f+^e$	$T_o/\sqrt{n_e}$
4	60.0	7.469	5.498
5	63.4	3.824	13.607
6	65.9	2.213	28.468
7	67.8	1.394	52.902
8	69.3	.934	90.460
9	70.5	.656	145.035

T/T_o

	F	.1	.2	.3	.4	.5	.6	.7	.8	.9
L	4	1.07	1.15	1.26	1.39	1.57	1.81	2.26	3.09	5.47
	5	1.07	1.15	1.25	1.39	1.57	1.83	2.25	3.06	5.41
	6	1.07	1.15	1.25	1.38	1.56	1.82	2.24	3.04	5.37
	7	1.07	1.15	1.25	1.38	1.56	1.82	2.23	3.03	5.36
	8	1.07	1.15	1.25	1.38	1.56	1.82	2.23	3.03	5.35
	9	1.07	1.15	1.25	1.38	1.56	1.81	2.23	3.03	5.34

Table C-3

Dipole Model

$R_r = 1.5$

Density - $n = n_o \left(\frac{R_e}{r}\right)^4$

L	LAT	$f+^e$	$T_o/\sqrt{n_e}$
4	60.0	7.469	6.044
5	63.4	3.824	15.073
6	65.9	2.213	31.737
7	67.8	1.394	59.135
8	69.3	.934	101.354
9	70.5	.656	162.670

T/T_o

	F	.1	.2	.3	.4	.5	.6	.7	.8	.9
L	4	1.06	1.14	1.24	1.37	1.54	1.78	2.18	2.94	5.12
	5	1.06	1.14	1.24	1.36	1.53	1.77	2.15	2.90	5.03
	6	1.06	1.14	1.23	1.35	1.52	1.76	2.14	2.87	4.97
	7	1.06	1.14	1.23	1.35	1.52	1.75	2.13	2.86	4.95
	8	1.06	1.14	1.23	1.35	1.51	1.75	2.13	2.85	4.93
	9	1.06	1.14	1.23	1.35	1.51	1.75	2.12	2.84	4.92

Table C-4

Dipole Model

$R_r = 1.0$

L	LAT	$f+^e$	$T_o/\sqrt{n_e}$
4	60.0	7.169	6.269
5	63.4	3.824	15.431
6	65.9	2.213	32.132
7	67.8	1.394	59.727
8	69.3	.934	102.154
9	70.5	.656	163.802

T/T_o

	F	.1	.2	.3	.4	.5	.6	.7	.8	.9
L	4	1.06	1.14	1.23	1.35	1.52	1.76	2.14	2.87	4.97
	5	1.06	1.14	1.23	1.35	1.51	1.75	2.13	2.85	4.94
	6	1.06	1.14	1.23	1.35	1.51	1.75	2.12	2.84	4.92
	7	1.06	1.14	1.23	1.35	1.51	1.74	2.12	2.84	4.91
	8	1.06	1.14	1.23	1.35	1.51	1.74	2.12	2.83	4.90
	9	1.06	1.14	1.23	1.35	1.51	1.74	2.12	2.83	4.90

Table C-4

$R_b = 10$ 00:00 LMT

L	LAT	F^e_+	$T_o/\sqrt{n_e}$
4	60.5	7.235	6.179
5	64.0	4.047	15.116
6	67.0	2.404	31.195
7	69.0	1.552	57.161
8	70.5	1.060	96.049
9	72.0	.750	151.119

T/T_o

	F	.1	.2	.3	.4	.5	.6	.7	.8	.9
L	4	1.06	1.14	1.23	1.36	1.52	1.76	2.15	2.88	5.00
	5	1.06	1.14	1.23	1.36	1.52	1.76	2.14	2.87	4.97
	6	1.06	1.14	1.23	1.35	1.52	1.75	2.13	2.86	4.94
	7	1.06	1.14	1.23	1.35	1.51	1.75	2..2	2.83	4.88
	8	1.06	1.14	1.23	1.35	1.50	1.73	2.10	2.79	4.77
	9	1.06	1.13	1.22	1.34	1.49	1.71	2.06	2.72	4.59

Table C-5

R_b = 10 03:00

L	LAT	F_{ft}^{e}	$T_o/\sqrt{n_e}$
4	60.5	7.761	6.176
5	69.5	4.094	15.117
6	67.0	2.460	31.129
7	69.0	1.618	56.972
8	71.0	1.135	95.642

T/T_o

F	.1	.2	.3	.4	.5	.6	.7	.8	.9
4	1.06	1.14	1.24	1.36	1.53	1.77	2.15	2.89	5.02
5	1.06	1.14	1.23	1.36	1.52	1.76	2.15	2.89	5.01
6	1.06	1.14	1.23	1.36	1.52	1.76	2.15	2.89	5.02
7	1.06	1.14	1.23	1.36	1.53	1.77	2.15	2.89	5.03
8	1.06	1.14	1.23	1.36	1.52	1.76	2.15	2.89	5.00

Table C-6

$R_b = 10$ 06:00

L	LAT	F^e_+	$T_o/\sqrt{n_e}$
4	60.5	7.852	6.167
5	64.5	4.207	15.078
6	67.5	2.596	30.036
7	69.5	1.776	56.761
8	72.0	1.316	95.562

T/T_o

L	F	.1	.2	.3	.4	.5	.6	.7	.8	.9
4	1.06	1.14	1.24	1.36	1.53	1.77	2.16	2.91	5.06
5	1.06	1.14	1.24	1.36	1.53	1.78	2.17	2.93	5.11
6	1.06	1.14	1.24	1.37	1.54	1.79	2.20	2.98	5.24
7	1.07	1.15	1.25	1.38	1.56	1.82	2.24	3.06	5.45
8	1.07	1.15	1.26	1.39	1.58	1.86	2.30	3.18	5.77

Table C-7

R_b =10 09:00

L	LAT	f^e_+	$T_o/\sqrt{n_e}$
4	61.0	7.942	6.170
5	64.5	4.320	15.044
6	67.5	2.732	30.958
7	70.5	1.935	56.883
8	73.0	1.498	96.883

T/T_o

F	.1	.2	.3	.4	.5	.6	.7	.8	.9
4	1.06	1.14	1.24	1.36	1.53	1.78	2.17	2.92	5.10
5	1.06	1.14	1.24	1.37	1.54	1.79	2.19	2.97	5.23
6	1.07	1.15	1.25	1.38	1.56	1.82	2.25	3.08	5.50
7	1.07	1.15	1.26	1.40	1.60	1.88	2.35	3.27	6.03
8	1.07	1.17	1.28	1.44	1.66	1.98	2.53	3.65	7.22

Table C-8

R_b = 10 12:00

L	LAT	$F^e_{\mp}$	$T_o/\sqrt{n_e}$
4	61	7.980	6.167
5	64.5	4.367	15.031
6	68.0	2.788	30.971
7	70.5	2.001	56.979
8	73.5	1.573	97.931

T/T_o

L \ F	.1	.2	.3	.4	.5	.6	.7	.8	.9
4	1.06	1.14	1.24	1.36	1.53	1.78	2.17	2.93	5.12
5	1.06	1.14	1.24	1.37	1.54	1.80	2.20	2.99	5.27
6	1.07	1.15	1.25	1.31	1.57	1.84	2.27	3.12	5.61
7	1.07	1.16	1.27	1.41	1.61	1.91	2.40	3.38	6.34
8	1.08	1.17	1.30	1.46	1.70	2.05	2.67	3.97	8.38

Table C-9

$R_b = 8$ 00:00

L	LAT	f^e_+	$T_o/\sqrt{n_e}$
4	61.0	7.904	6.135
5	64.5	4.181	14.906
6	67.5	2.491	30.512
7	69.5	1.594	55.388
8	71.0	1.056	92.217

T/T_o

L \ F	.1	.2	.3	.4	.5	.6	.7	.8	.9
4	1.06	1.14	1.24	1.36	1.53	1.77	2.15	2.89	5.01
5	1.06	1.14	1.24	1.36	1.52	1.76	2.14	2.87	4.95
6	1.06	1.14	1.23	1.35	1.51	1.74	2.11	2.82	4.85
7	1.06	1.13	1.22	1.34	1.50	1.72	2.07	2.75	4.65
8	1.06	1.13	1.21	1.32	1.47	1.68	2.01	2.63	4.37

Table C-10

R_b = 8 03:00

L	LAT	$f^e_{\mp}$	$T_o/\sqrt{n_e}$
4	61.0	7.995	6.137
5	64.5	4.295	14.888
6	67.5	2.629	30.412
7	70.0	1.754	55.096
8	72.0	1.239	91.313

T/T_o

F	.1	.2	.3	.4	.5	.6	.7	.8	.9
4	1.06	1.14	1.24	1.36	1.53	1.77	2.16	2.90	5.05
5	1.06	1.14	1.24	1.36	1.53	1.77	2.16	2.90	5.05
6	1.06	1.14	1.24	1.36	1.53	1.77	2.16	2.90	5.03
7	1.06	1.14	1.23	1.36	1.52	1.76	2.14	2.87	4.96
8	1.06	1.14	1.23	1.35	1.51	1.74	2.11	2.81	4.79

Table C-11

R_b = 8 06:00

L	LAT	$f^e_{\mp}$	$T_o/\sqrt{n_e}$
4	61.0	8.217	6.120
5	65.0	4.512	14.838
6	68.5	2.961	30.340
7	71.5	2.141	55.366
8	74.5	1.681	93.851

T/T_o

L \ F	.1	.2	.3	.4	.5	.6	.7	.8	.9
4	1.06	1.14	1.24	1.37	1.54	1.78	2.18	2.95	5.15
5	1.07	1.14	1.24	1.37	1.55	1.80	2.21	3.01	5.31
6	1.07	1.15	1.25	1.39	1.57	1.84	2.27	3.12	5.61
7	1.07	1.16	1.27	1.41	1.61	1.90	2.37	3.31	6.12
8	1.07	1.17	1.29	1.44	1.66	1.98	2.53	3.63	7.03

Table C-12

$R_b = 8$ 09:00

L	LAT	f^e_+	$T_o/\sqrt{n_e}$
4	61.5	8.438	6.115
5	65.5	4.848	14.819
6	69.5	3.293	30.530
7	73.0	2.528	57.410

T/T_o

L \ F	.1	.2	.3	.4	.5	.6	.7	.8	.9
4	1.06	1.14	1.24	1.37	1.54	1.80	2.20	2.99	5.26
5	1.07	1.15	1.25	1.37	1.57	1.84	2.27	3.12	5.62
6	1.07	1.16	1.27	1.42	1.62	1.93	2.43	3.43	6.51
7	1.08	1.18	1.31	1.49	1.74	2.13	2.81	4.31	9.85

Table C-13

R_b = 8 12:00

L	LAT	f^e_+	$T_o/\sqrt{n_e}$
4	61.5	8.529	6.099
5	66.0	4.963	14.812
6	89.5	3.430	30.631
7	74.0	2.689	59.012

T/T_o

	F	.1	.2	.3	.4	.5	.6	.7	.8	.9
L	4	1.07	1.15	1.24	1.37	1.55	1.80	2.22	3.01	5.32
	5	1.07	1.15	1.26	1.39	1.58	1.85	2.30	3.18	5.78
	6	1.07	1.17	1.28	1.44	1.65	1.97	2.51	3.61	7.08
	7	1.09	1.20	1.34	1.54	1.83	2.31	3.20	5.45	19.50

Table C-14

$R_b = 8$ 12:00

L	LAT	$f_{\mp}^{e}$	$T_o/\sqrt{n_e}$
5.6	68.0	3.908	23.243
6.4	71.0	3.072	39.968

T_o/T_o

	F	.1	.2	.3	.4	.5	.6	.7	.8	.9
L	5.6	1.07	1.16	1.27	1.41	1.62	1.91	2.40	3.39	6.37
	6.4	1.08	1.17	1.30	1.46	1.70	2.06	2.67	3.98	8.40

APPENDIX D

MODEL PARAMETERS AND VELOCITY PROFILES

Tables D-1 through D-4 contain the model parameters for the open and closed models of Chapter 3.

Tables D-5 through D-8 contain representative velocity profiles for these models.

Table D-1

Ionospheric Model I-1

Night Solar Minimum - Low Collision Frequency
v- = electron collision frequency
v+ = proton collision frequency

alt. (km)	n (l/cm^3)	molecular weight	v-(l/sec)	v+(l/sec)
100	.15 E04	27.0	.45 E05	.25 E04
130	.21 Eo4	25.5	.20 E04	.70 E02
160	.25 E04	24.0	.35 E03	.13 E02
200	.30 E04	21.0	.10 E03	.27 E01
240	.50 E04	17.5	.55 E02	.90 E00
280	.10 E05	17.0	.80 E02	.35 E00
320	.10 E06	16.9	.16 E03	.15 E00
370	.13 E06	16.7	.19 E03	.50 E-1
450	.80 E05	16.4	.13 E03	.90 E-2
580	.35 E05	15.2	.60 E02	.50 E-3
700	.20 E05	13.5	.25 E02	.9 E-4
850	.10 E05	9.5	.80 E01	.0
1000	.60 E04	3.8	.25 E01	.0

Table D-2

Ionosphere Model I-2

Night Solar Minimum - High Collision Frequency

alt. (km)	n (l/cm^3)	Weight	v-(l/sec)	v+(l/sec)
100	.15 E04	27.0	.47 E05	.30 E04
130	.21 E04	25.5	.30 E04	.14 E04
160	.25 E04	24.0	.40 E03	.23 E02
200	.30 E04	21.0	.20 E03	.56 E01
240	.50 E04	17.5	.10 E03	.22 E01
280	.10 E05	17.0	.20 E03	.92 E00
320	.10 E06	16.9	.30 E03	.44 E00
370	.13 E06	16.7	.30 E03	.17 E00
450	.80 E05	16.4	.20 E03	.40 E-1
580	.35 E05	15.2	.15 E03	.10 E-1
700	.20 E05	13.5	.10 E03	.40 E-2
850	.10 E05	9.5	.70 E02	.0
1000	.60 E04	3.8	.50 E02	.0

Table D-3

Ionosphere Model I-3

0600 Solar Minimum - High Collision Frequency

alt (km)	n ($1/cm^3$)	weight	v-(1/sec)	v+(1/sec)
100	.20 E05	27.0	.46 E05	.30 E04
130	.25 E05	25.5	.30 E04	.14 E04
160	.40 E05	24.0	.40 E03	.24 E02
200	.70 E05	21.0	.20 E03	.56 E01
240	.95 E05	17.5	.10 E03	.22 E01
280	.23 E06	17.0	.20 E03	.92 E00
320	.32 E06	16.9	.30 E03	.44 E00
370	.32 E06	16.7	.30 E03	.17 E00
450	.20 E06	16.4	.20 E03	.40 E-1
580	.85 E05	15.2	.15 E03	.10 E-1
700	.42 E05	13.5	.10 E03	.40 E-2
850	.22 E05	9.5	.70 E02	.0
1000	.13 E05	3.8	.50 E02	.0

Table D-4

Magnetosphere Models

L = 7 arc distance (km)	Low Density (ne=1) $n(1/cm^3)$	High Density (ne=2.7) $n(1/cm^3)$
.10 E04	.60 E04	.60 E04
.20 E04	.17 E04	.17 E04
.40 E04	.42 E03	.70 E03
.80 E04	.90 E02	.25 E03
.16 E05	.20 E02	.46 E02
.24 E05	.60 E01	.16 E02
.32 E05	.27 E01	.80 E01
.40 E05	.15 E01	.45 E01
.48 E05	.11 E01	.30 E01
.55 E05	.10 E01	.27 E01

L = 8 arc distance (km)	$n(1/cm^3)$
.10 E04	.80 E04
.20 E04	.22 E04
.40 E04	.60 E03
.80 E04	.16 E03
.16 E05	.31 E02
.24 E05	.95 E01
.32 E05	.42 E01
.40 E05	.23 E01
.48 E05	.15 E01
.56 E05	.11 E01
.64 E05	.10 E01

Table D-5

I-1 Ionospheric Model Velocity (km/sec)

	.01 cps		.1 cps		.6 cps	
alt.	V_r	V_i	V_r	V_i	V_r	V_r
100	.49 E02	.12 E03	.16 E03	.38 E03	.39 E03	.91 E03
130	.64 E03	.19 E03	.53 E03	.59 E03	.14 E04	.13 E04
160	.37 E03	.37 E03	.12 E04	.11 E04	.30 E04	.15 E04
200	.62 E03	.59 E03	.22 E04	.14 E04	.39 E04	.90 E03
240	.79 E03	.70 E03	.25 E04	.10 E04	.33 E04	.31 E03
280	.59 E03	.49 E03	.16 E04	.43 E03	.18 E04	.85 E02
320	.36 E03	.26 E03	.77 E03	.12 E03	.79 E03	.21 E02
370	.51 E03	.29 E03	.82 E03	.72 E02	.82 E03	.12 E02
450	.95 E03	.31 E03	.11 E04	.47 E02	.11 E04	.78 E01
580	.15 E04	.25 E03	.16 E04	.28 E02	.16 E04	.46 E01
700	.23 E04	.15 E03	.23 E04	.15 E02	.23 E04	.25 E01
850	.42 E04	.79 E02	.42 E04	.79 E01	.42 E04	.13 E01

Table D-6

I-3 Ionospheric Model Velocity (km/sec)

	.01 cps		.1 cps		.6 cps	
alt.	V_r	V_i	V_r	V_i	V_r	V_i
100	.14 E02	.34 E02	.45 E02	.11 E03	.15 E03	.33 E03
130	.43 E02	.50 E02	.14 E03	.16 E03	.47 E03	.49 E03
160	.81 E02	.82 E02	.27 E03	.24 E03	.78 E03	.32 E03
200	.14 E03	.13 E03	.47 E03	.30 E03	.89 E03	.13 E03
240	.17 E03	.15 E03	.55 E03	.23 E03	.72 E03	.42 E02
280	.18 E03	.15 E03	.48 E03	.12 E03	.52 E03	.14 E02
320	.22 E03	.16 E03	.46 E03	.60 E02	.47 E03	.74 E01
370	.32 E03	.18 E03	.52 E03	.46 E02	.52 E03	.45 E01
450	.60 E03	.20 E03	.72 E03	.30 E02	.72 E03	.30 E01
580	.10 E04	.18 E03	.11 E04	.18 E02	.11 E04	.18 E01
700	.17 E04	.99 E02	.16 E04	.10 E02	.16 E04	.10 E01
850	.28 E04	.54 E02	.28 E04	.53 E01	.28 E04	.53 E00

Table D-7

L=7 Magnetospheric Model Velocity (km/sec)

	n_e =1		n_e = 2.7	
	.1 cps	1.0 cps	.1 cps	.6 cps
arc dist.				
.10 E04	.12 E05	.12 E05	.12 E05	.12 E05
.20 E04	.14 E05	.14 E05	.13 E05	.13 E05
.40 E04	.13 E05	.13 E05	.91 E04	.91 E04
.80 E04	.90 E04	.90 E04	.56 E04	.56 E04
.16 E05	.55 E04	.52 E04	.35 E04	.34 E04
.24 E05	.39 E04	.35 E04	.23 E04	.22 E04
.32 E05	.30 E04	.24 E04	.17 E04	.15 E04
.40 E05	.24 E04	.18 E04	.14 E04	.12 E04
.48 E05	.20 E04	.12 E04	.12 E04	.97 E03
.55 E05	.19 E04	.11 E04	.12 E04	.92 E03

Table D-8

L=8, n_e=1 Magnetospheric Model Velocity (km/sec)

arc dist.	.01 cps	.60 cps
.10 E04	.11 E05	.11 E05
.20 E04	.12 E05	.12 E05
.40 E04	.11 E05	.11 E05
.80 E04	.92 E04	.92 E04
.16 E05	.66 E04	.65 E04
.24 E05	.32 E04	.30 E04
.32 E05	.24 E04	.21 E04
.40 E05	.19 E04	.15 E04
.48 E05	.16 E04	.11 E04
.56 E05	.14 E04	.87 E04
.63 E05	.13 E04	.80 E04

REFERENCES

Allis, W.P., S.J. Buchsbaum and A. Bers, Waves in Anistropic Plasmas, MIT Press, 1962

Angerami, J.J., and D.L. Carpenter, Whistler studies of the plasmapause in the magnetosphere, 2. Electron density and total tube electron content near the knee in the magnetospheric ionization, J. Geophys. Res., 71, 711, 1966

Benioff, H., Observations of geomagnetic fluctuations in the period range 0.3 - 120 sec, J. Geophys. Res., 65, 1413, 1960

Carpenter, D.L., Whistler studies of the plasmapause in the magnetosphere, 1. Temporal variations in the position of the knee and some evidence of plasma motions near the knee, J. Geophys. Res., 71, 693, 1966

Cornwall, J.M., Cyclotron instabilities and electromagnetic emission in the ultra low frequency and very low frequency ranges, J. Geophys. Res., 70, 61, 1965

Duffus, N.Y., W.W. Nasmyth, J.A. Shand, and C. Wright, Subaudible geomagnetic fluctuations, Nature, 181, 1258, 1958

Gendrin, R., A theory of fine structured micropulsations, Ann. De Geophys. 19, (3), 1963

Harung, L., Oscillations and vibrations in magnetic records at high latitude stations, Terr. Mag. Atmos. Elect., 41, 329, 1936

Hruska, A., Cyclotron Instabilities in the magnetosphere, J. Geophys. Res., 71, 1377, 1966

Jacobs, J.A., and T. Watanabe, Micropulsation Whistlers, J. Atmos. Terrest. Phys., 26, 825, 1964

Jacobs, J.A., and T. Watanabe, Amplification of hydromagnetic waves in the magnetosphere by a cyclotron instability process with applications to the theory of hydromagnetic whistlers, J. Atmos. Terrest. Phys., 28, 235, 1966

Kenney, J.F., and H.B. Knaflich, A systematic study of structured micropulsations J. Geophys. Res., 72, 2858, 1967

Liemohn, H., Cyclotron-resonance amplification of VLF and VLF whistlers, J. Geophys. Res., 72, 39, 1967

Lokken, J.E., J.A. Shand and C.S. Wright, Some characteristics of electromagnetic background signals in the vicinity of one cycle per second, J. Geophys. Res., 68, 789, 1963

Madden, T.R., Spectral, cross-spectral and bispectral analysis of low frequency electromagnetic data, in Natural Electromagnetic Phenomena Below 30 KC/S, edited by D.F. Bleil, p.429, Plenum Press, 1964

Manchester, R.N., Propagation of Pc1 micropulsations from high to low latitudes J. Geophys. Res., 71, 3749, 1966

Mead, G.D., Deformation of the geomagnetic field by the solar wind. J. Geophys. Res., 69, 1181, 1964

Obayashi, T., Hydromagnetic Whistlers, T. Geophys. Res., 70, 1069, 1965

Pope, J.H., Dynamic spectral characteristics of micropulsation pearls, J. Geophys. R_es., 70, 3595, 1965

Prince, C.E., F.X. Bostick and H.W. Smith A study of the transmission of plane hydromagnetic waves through the upper atmosphere, Report No. 134 of the Electrical Engineering Laboratory, The University of Texas, 1964

Shanks, J.L., Recursion filters for digital processing, Geophysics, 32, 33, 1967

Sill, W.R., Pearls and hydromagnetic emissions, Oral paper submitted as partial fulfillment for the general examination in geophysics at MIT, 1965

Smith, R.L., and N. Brice, Propagation in multicomponent plasmas, J. Geophys. Res., 69, 5029, 1964

Stix, T.H., The Theory of Plasma Waves, McGraw-Hill, 1962

Sucksdorff, E., Occurrences of rapid micropulsations at Sodanklya during 1932-1935, Terr. Mag. Atmos. Elect., 41, 337, 1936

Taylor, H.A., H.C. Brinton, and R.C. Smith, Positive ion composition in the magnetosphere obtained from Ogo-A Satellite, J. Geophys.Res., 70, 5769, 1965

Tepley, L.R., Observations of hydromagnetic emissions, J. Geophys. Res., 66, 1651, 1961

Tepley, L.R., and R.C. Wentworth, Hydromagnetic emissions, X-ray bursts, and electron bunches, 1. Experimental results, J. Geophys. Res., 67, 3317, 1962

Tepley, L.R., Low latitude observations of fine-structured hydromagnetic emissions, J. Geophys. Res., 69, 2273, 1964

Tepley, L.R., and R.K. Landshoff, Waveguide theory for ionospheric propagation of hydromagnetic emissions, J. Geophys. Res., 71, 1499, 1966

Thorne, R.M., and C.F. Kennel, Quasi-trapped VLF propagation in the outer magnetosphere, J. Geophys. Res., 72, 857, 1967

Troitskaya, V.A., Earth current installations of the USSR, Ann. IGY, 4, 322, 1957

Troitskaya, V.A., Pulsations of earth's electromagnetic field (T 15 sec) and their connection with phenomena in high atmosphere, J. Geophys. Res., 66, 5, 1961

Watanabe, T., Determination of the electron distribution in the magnetosphere using hydromagnetic whistlers, J. Geophys. Res., 70, 5839, 1965

Wentworth, R.C., and L.R. Tepley, Hydromagnetic emissions, X-ray bursts, and electron bunches 2. Theoretical interpretation, J. Geophys. Res., 67, 3335, 1962

Wentworth, R.C., Recent investigations of hydromagnetic emissions, Part II theoretical interpretation, J. Geomag. Geoelect., 18, 257, 1966

Yanugihara, K., Geomagnetic micropulsations with periods from .03 to 10 seconds in the auroral zones with special reference to conjugate-point studies, J. Geophys. Res., 68, 3383, 1963

BIOGRAPHICAL NOTE

The author received his undergraduate education at Michigan State University and received a B.S. in Geology in 1960. He attended graduate school at M.I.T. during the periods 1960 to 1963 (S.M.) and 1964 to 1967 (Ph.D) and the University of California at San Diego during the period 1963 to 1964.

The author's professional experience includes part time employment by Jones and Laughlin Steel Co. - Michigan Ore Division, Geoscience Inc., Chevron Research Corp., and Avco Corp. - Space Sciences Division.